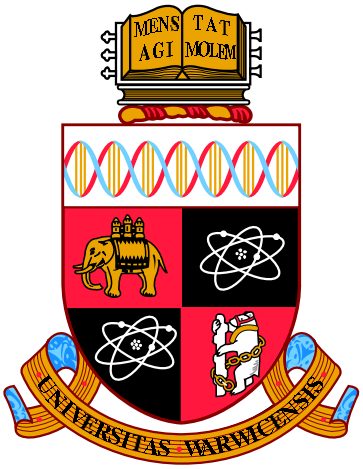

Neuronal Signal Modulation by Dendritic Geometry

by

Yihe Lu

Thesis

Submitted to the University of Warwick

for the degree of

Doctor of Philosophy

Centre for Complexity Science

August 2018

THE UNIVERSITY OF WARWICK

Contents

Cogito, ergo sum.

– René Descartes

Si Xu (*Thinking*). Xiaohe Lu, 2018.

Acknowledgments

First of all, I would like to express my most sincere gratitude to my supervisor, Dr. Yulia Timofeeva. I started my Ph.D. project with passionate curiosity in nature and science but mere preparation in the research direction. She has been since then the most supportive and encouraging person. Discussions with her have always been enjoyable and pedagogic. My Ph.D. work, as well as my Ph.D. life, has benefited considerably from her guidance and assistance.

Second, I want to thank Dr. Hugo van den Berg and Prof. Magnus Richardson, who brought me the initial insight and interest into the field of neuroscience during my postgraduate study, and all the staff at the Centre for Complexity Science for their ardent support in my doctoral training. I would also like to thank Dr. Nicolangelo Iannella for inspiring discussions over dendritic resonance and taper, and Dr. Tom Rother for constructive suggestions on Green's functions in general cases.

Last but not least, I am grateful to my families and friends. To borrow some words from Isaac Newton, I have been playing on the seashore, looking for pretty shells, and knowing nothing about the great ocean of truth. Nonetheless, I do know I can see stars at night, and they are my families and friends. Amongst them I dedicate the special thanks to my father, Xiaohe Lu. He has not only offered me supports in life, but also inspirations. The picture, **Si Xu**, on page **iv** is one of his recent art works.

Declarations

I declare this thesis is my original work, and I gratefully credit all the authors of the literature that form the foundation of my work. In terms of the copyright issue, the permissions to reuse the materials in Fig. 1.1, 1.2, 1.3 and 5.1 in this thesis are granted to me by the publishers. In addition, Fig. 2.4 is reused with minor modifications at the courtesy of Yulia Timofeeva (one of the authors of the original material) under a Creative Commons license.

Parts of this thesis have been written up into two papers:

- **Lu Yihe** and Yulia Timofeeva. Response functions for electrically coupled neuronal network: a method of local point matching and its applications. *Biological Cybernetics*, 110(2-3):117–133, 2016.

- **Lu Yihe** and Yulia Timofeeva. Cable theory in neurons with tapered and branched dendrites. *In preparation for submission.*

The first paper presents the original development of the method of local point matching, and thus contains the same content as in **Chapter 2**. Nonetheless, the chapter offers more rigorous deductions and more comprehensive explanations. The second paper derives the generalised sum-over-trips framework for reducible tapers, which duplicates some sections in **Chapter 3**. It will be submitted for publication in March, 2019.

This thesis is submitted to the University of Warwick for the degree of Doctor of Philosophy in Complexity Science. It has not been submitted to other institutions.

Abstract

Neurons are the basic units in nervous systems. They transmit signals along neurites and at synapses in electrical and chemical forms. Neuronal morphology, mainly dendritic geometry, is famous for anatomical diversity, and names of many neuronal types reflect their morphologies directly. Dendritic geometries, as well as distributions of ion channels on cell membranes, contribute significantly to distinct behaviours of electrical signal filtration and integration in different neuronal types (even in the cases of receiving identical inputs *in vitro*).

In this thesis I mainly address the importance of dendritic geometry, by studying its effects on electrical signal modulation at the level of single neurons via mathematical and computational approaches. By "geometry", I consider both branching structures of entire dendritic trees and tapered structures of individual dendritic branches. The mathematical model of dendritic membrane potential dynamics is established by generalising classical cable theory. It forms the theoretical benchmark for this thesis to study neuronal signal modulation on dendritic trees with tapered branches. A novel method to obtain analytical response functions in algebraically compact forms on such dendrites is developed. It permits theoretical analysis and accurate and efficient numerical calculation on a neuron as an electrical circuit. By investigating simplified but representative dendritic geometries, it is found that a tapered dendrite amplifies distal signals in comparison to the non-tapered dendrite. This modulation is almost a local effect, which is merely influenced by global dendritic geometry. Nonetheless, global geometry has a stronger impact on signal amplitudes, and even more on signal phases. In addition, the methodology employed in this thesis is perfectly compatible with other existing methods dealing with neuronal stochasticity and active behaviours. Future works of large-scale neural networks can easily adapt this work to improve computational efficiency, while preserving a large amount of biophysical details.

Abbreviations

- IF - Integrate-and-Fire
- EPSC - Excitatory Post-Synaptic Current
- EPSP - Excitatory Post-Synaptic Potential
- LTI - Linear Time-Invariant
- RC - Resistor-Capacitor
- LRC - Inductor-Resistor-Capacitor
- STDP - Spike-Timing-Dependent Plasticity
- CR - Coupling Ratio
- SDS - Spike-Diffuse-Spike
- FDF - Fire-Diffuse-Fire

Units

- ms - millisecond
- min - minute
- kHz - kilohertz
- µm - micrometer
- cm - centimeter
- nA - nanoampere
- mV - millivolt
- Ω - ohm
- MΩ - megaohm
- H - henry
- µF - microfarad
- dB - decibel

Chapter 1

Introduction

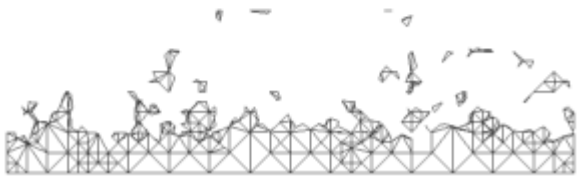

1.1 Overview of thesis

A nerve cell, also known as a *neuron*, is the basic unit in any nervous system. A human brain, probably the most complex nervous system, consists of approximately 10^{11} neurons; the number is of the same order as that of the stars in our galaxy, but the interactions among neurons are not dominated by the single force of gravity. Most neurons shares a typical structure, consisting of a soma (i.e. cell body), an axon and dendrites. Via neurites (i.e. dendrites and axons) and synapses (chemical or electrical), a typical neuron can connect to and communicate with thousands of other cells, locally and distantly, forming small neuronal circuits, large neural networks and eventually an entire nervous system. Since the exemplary works of Ramón y Cajal [1], scientists started to study the complex branching structures of neuronal dendrites, which is probably the most distinguishable feature of neurons. As composed by Spencer [2] that, *"Everywhere structures in great measure determine functions; and everywhere functions are incessantly modifying structures"*, the interplay between anatomy and physiology in dendrites is evidently vital [3–8]. In particular, different types of neurons modulate electrical signals differently, because of their distinct dendritic geometries [5–8].

This thesis tries to understand how dendritic geometry modulates neuronal signal transmission on a single neuron from a theoretical perspective, mainly by mathematical analysis accompanied with numerical results. Although the functional differences between neurons are also considerably determined by species of ion channels on cell membranes [9–16], their types and distributions are completely encoded into the electrical parameters in the simplified mathematical models of dendritic electrophysiology to be employed in this thesis. In the following sections of this **Chapter 1**, I will introduce, from a mathematical modelling point of view, neuronal morphology and electrophysiology respectively in the content of neuroscience in general. These two aspects of dendrites are then brought together and synthesised in the mathematical formalism "dendritic cable theory" [17]. **Chapter 2** will find a mathematical approach to find electrical response functions on neurons of arbitrary dendritic geometry, which is the principal task of this thesis. For simplicity, individual dendritic branches are modelled by cylindrical segments here. Based on the path integral formulation, the sum-over-trips framework is derived and extended [18–20]. I then develop the method of local point matching, a novel approach to find analytical Green's functions in compact algebraic forms on dendritic trees of arbitrary branching structures. The sum-over-trips framework will then be extended in **Chapter 3**, from the original one on cylindrical dendrites to a generalised framework on ta-

pered dendrites. In **Chapter 4**, I will consider several neuronal models of simplified but representative dendritic geometries. The local point matching method will be employed to calculate the analytical Green's functions, and then explicit effects of dendritic geometry on signal modulation will be investigated over the numerical results. Finally in **Chapter 5**, I will summarise this thesis, discuss the results and finish by proposing several natural extensions and implications.

1.2 Mathematical modelling of neuronal dendrites

The term *dendrite*, coined by Wilhelm His in 1889 [21], originates from Greek, which literally means *a tree*, or *a tree-like form* [22]. Scientific investigation on neuronal dendrites started with Ramón y Cajal [1], and the classification of neurons by their distinct morphologies is one of the most common and conventional perspectives, e.g. pyramidal neurons (see Fig. 1.1 for more examples). Such anatomical varieties can directly lead to functional differences. Computer simulations have shown that, with identical ion channel types and distributions, different morphologies present distinct signal propagation and firing patterns when responding to the same input currents (see Fig. 1.2) [6, 7]. However, due to the natural heterogeneous distributions of ion channels on dendrites (and axons) [16], it is difficult to conduct real experiments on neurons of different morphologies with the ion channel distributions as control variables. Thus, theoretical approaches as taken by this thesis may help to shed light on the modulation of neuronal signals by dendritic geometries.

This section aims to build mathematical models of dendrites. By "mathematical modelling", two interdependent aspects of dendrites are considered: dendritic morphology, the geometry of the typical tree structure, and dendritic electrophysiology, the dynamics of membrane potentials.

1.2.1 Digital reconstructions

To obtain the morphological structure of a real neuron, *neuron tracing* is employed by neuroscientists. It has become one of the most fundamental tasks in neuroscience, particularly in computational neuroscience, as digital reconstructions obtained by neuron tracing are useful in computer simulations on single neurons or neural networks with realisitic neuronal morphologies [24]. There are online databases nowadays, e.g. Neuromorpho.org [25], which permit access to numerous neuron reconstructions.

Conventionally, neurons are stained and imaged in fixed brain tissue by the Golgi's method, which was invented by Camillo Golgi, employed by Ramón y Cajal,

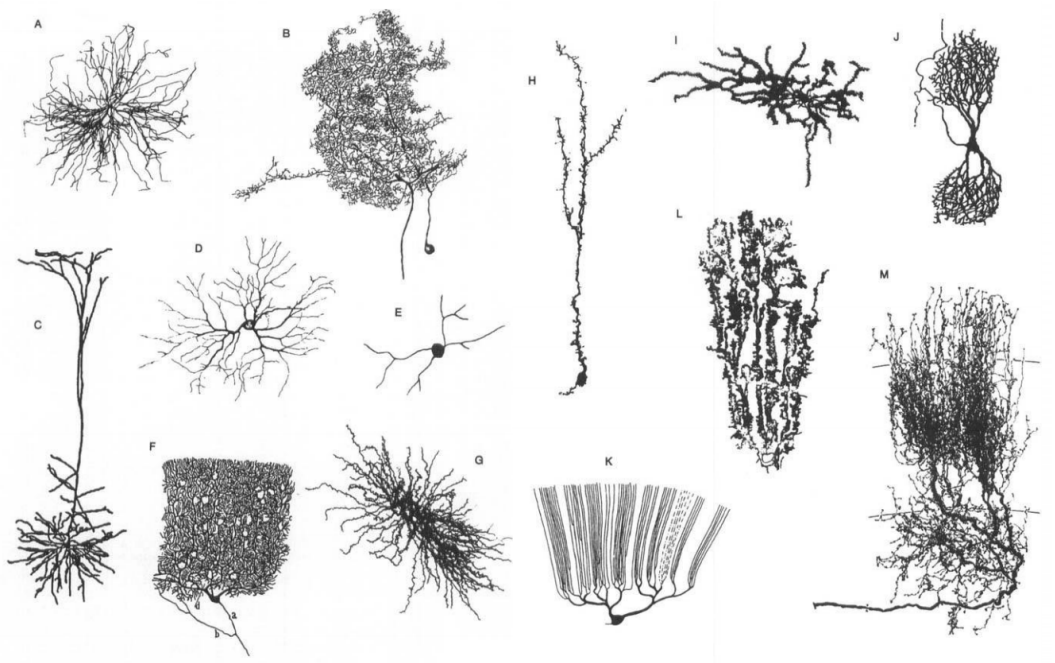

Figure 1.1: Distinct morphologies of different neurons. (**A**): Alpha motor neuron in spinal cord of cat. (**B**): Spiking interneuron in mesothoracic ganglion of locust. (**C**): Layer 5 neocortical pyramidal neuron in rat. (**D**): Retinal ganglion neuron in postnatal cat. (**E**): Amacrine neuron in retina of larval tiger salamander. (**F**): Cerebellar Purkinje neuron in human. (**G**): Relay neuron in ventrobasal thalamus of rat. (**H**): Granule neuron in olfactory bulb of mouse. (**I**): Spiny projection neuron in rat striatum. (**J**): Neuron in the Nucleus of Burdach in human fetus. (**K**): Purkinje neuron in mormyrid fish. (**L**): Golgi epithelial (glial) neuron in cerebellum of normal-reeler mutant mouse chimera. (**M**): Axonal arborization of isthmotectal neurons in turtle. Copied from [23].

and is still in use by modern neuroscientists, whereas recent developments permit functional imaging [26, 27]. The work of Glaser and Van der Loos [28] is one of the first attempts on automation in neuron tracing. They employed computers to interact with the microscope and to store point coordinates, which were manually indicated by a human operator. In spite of many efforts to reduce the amount of human labour [29, 30], neuron tracing had remained as a difficult problem (see Fig. 1.3) [31, 32] until tremendous progress in the fields of computer science and computer vision occured in the recent years [33].

Instead of directly recording neuronal morphologies by some automatic process, nowadays it is preferred to acquire the entire image data first. These image data are initially refined by several image preprocessing techniques so that segmentation methods could be effectively employed. Segmenting usually starts with identifying

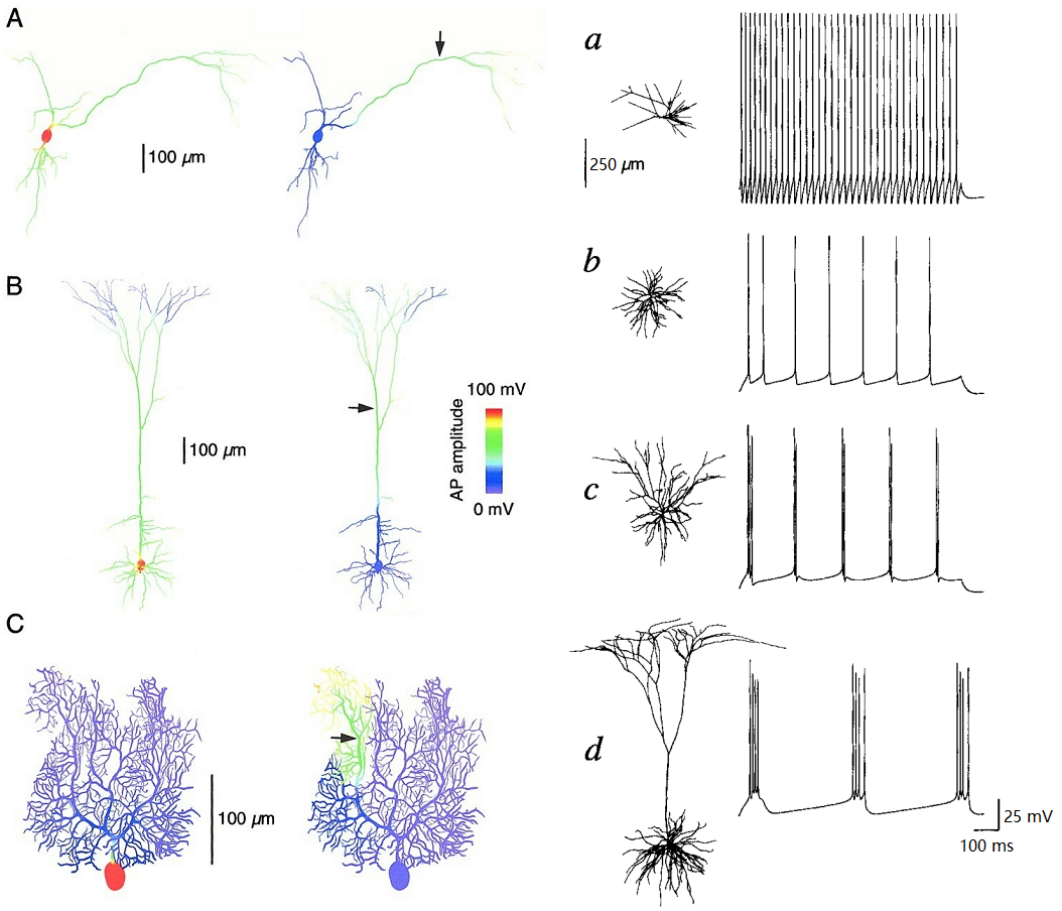

Figure 1.2: Different morphologies of neurons with identical ion channel types and distributions have distinct repsonses. (**A-C**): Backpropagation (from soma) and forward propagation (from location at $\rightarrow$) of action potentials. Copied from [7]. (**a-d**): Characteristic firing patterns evoked by somatic current injection. All the neurons are two-dimensional projections of three-dimensional digital reconstructions from rat brains. Copied from [6]. (**A**): Substantia nigra dopamine neuron. (**B**): Neocortical layer 5 pyramidal cell. (**C**): Cerebellar Purkinje cell. (**a**): Layer 3 aspiny stellate. (**b**): Layer 4 spiny stellate. (**c**): Layer 3 pyramid. (**d**): Layer 5 pyramid.

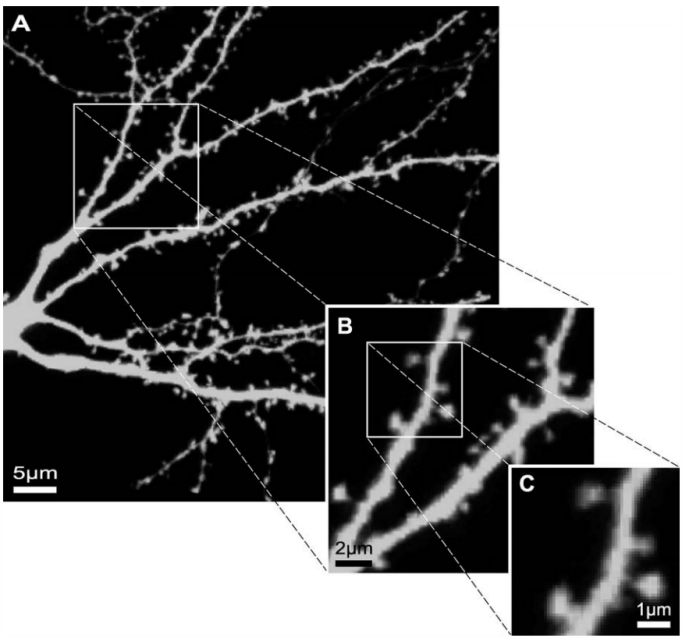

Figure 1.3: The multiscale nature of a dendritic tree. (**A**): The level of a individual neuron. (**B**): The level of dendritic branches and bifurcations. (**C**): The level of individual spines. While this is a fairly high-quality data set, several branches are still poorly stained in (**A**) and spines in (**C**) are usually poorly imaged due to the limited resolution and can be further blurred by noises, in particular in live-cell imaging experiments, thereby causing visual ambiguities and enhancing the complexity of the problem. Copied from [33].

soma, especially in the case where multiple neurons are present, neurites are the next to be tracked, and finally spines are detected [33]. The processing order is not only heuristic but also insightful, because a successive step can employ or even rely on the results of its preceding steps. After measuring parameters for all segments identified, automatic tracing is complete. It is however more rigorous to conduct proof-editing at this stage, because structural errors in reconstructions, if not corrected, could potentially take researchers more time to find out than conducting manual tracing [34].

One may run realistic computer simulations on such neuron reconstructions, e.g. the reconstruction in Fig. 1.4 employed by [19]. One may also conduct experiments by simulations that are nearly impossible in reality but insightful in theory. For example, the reconstructions shown in Fig. 1.2 are modelled with identical ion channels for different morphologies [6, 7]. The digital reconstruction of a neuron usually preserves the most comprehensive information of its three-dimensional morphology. Without any model reduction of the original reconstruction, mathematical analysis

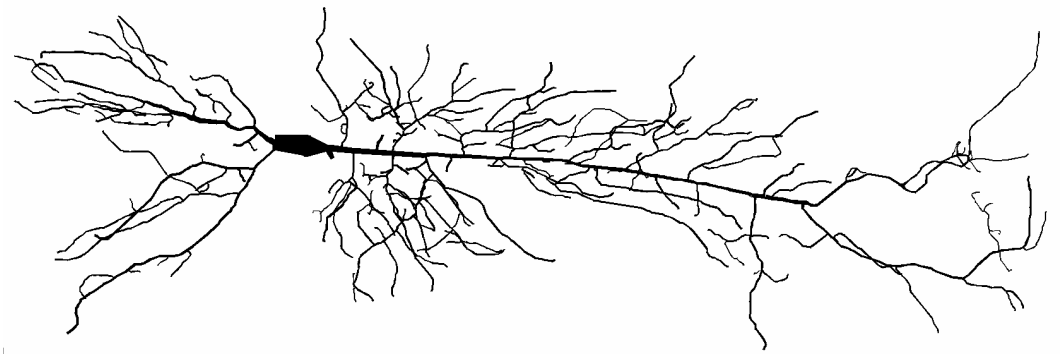

Figure 1.4: A reconstructed neuron from a rat CA1 hippocampal pyramidal cell. The reconstruction consists of 396 branches and a soma and is compartmentalised into 3961 cylindrical segments. Adapted from [19].

is extremely difficult, and numrical simulations are computationally expensive. As a result, there are very few but grand projects, e.g. the Human Brain Project [35], that does simulate a "large" network with such morphologically detailed neurons, in the hope of shedding light on the biological foundation of consciousness and intelligence. For example, Markram et al. [36] simulated a microcircuitry of the somatosensory cortex in a juvenile rat, which contains approximately 31,000 neurons.

1.2.2 Simplified geometries

To clearly exhibit branching structures of dendrites, a *dendrogram* is conventionally employed. Dendrograms are firstly introduced by Sholl [37] and thus are also known as Sholl diagrams (see Fig. 1.5 for an example). In order to draw theoretical insights and to save computational expenses, morpohologies of neuron reconstructions can be simplified and often considered as multi-compartment models (see schematic diagrams in Fig. 1.6). Since such a multi-compartment model virtually spans in a two-dimensional plane, the morphology of a neuron can be formally modelled as a weighted graph $\Gamma = (\mathcal{N}, \mathcal{B})$, in particular a weighted tree. Its vertices represent soma and branching nodes, and the edges represent dendritic branches. Moreover, Γ is a metric graph, as the weights of its edges are assigned to be the physical lengths of the corresponding branches. Based on this mathematical definition, methods of graph theory can be employed to study the dendritic geometry, e.g. algorithms for finding minimum spanning trees [38, 39].

It is practical and reasonable to study such simplified models for two main reasons. First, it is in principle impossible to acquire perfect details of dendritic morphology by simply increasing imaging resolution or reconstruction accuracy, because

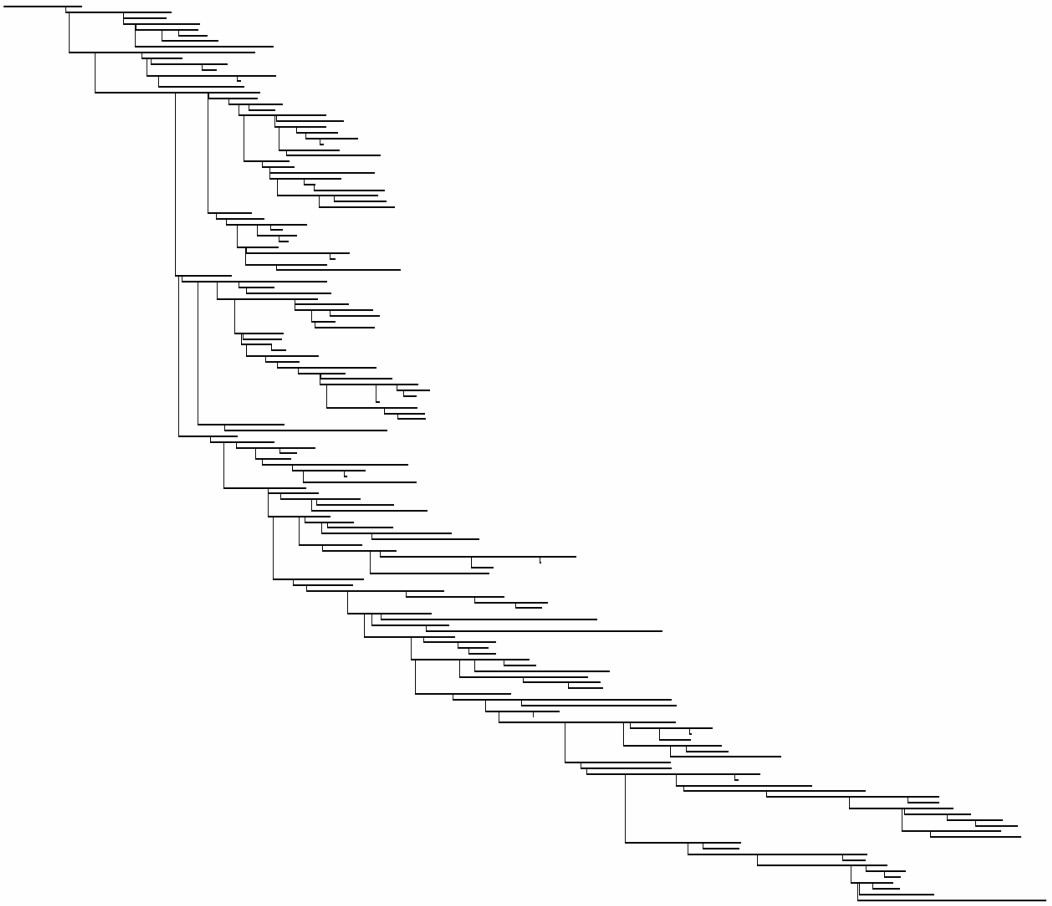

Figure 1.5: Dendrogram of the pyramidal cell shown in Fig. 1.4. Each horizontal segment represents a dendritic segment with its physical length and each vertical segment corresponds to a branching point.

a dendritic tree is constantly changing its structure due to the motility of dendritic spines [40]. Second, it is relatively straightforward to investigate neuronal electrophysiology (to be introduced in §1.2.3) on simplified morphologies by either mathematical analysis or computer simulations.

To further simplify dendritic geometry, one may consider a point neuron without any branching structure. It can be treated as the most extremely reduced model with only one compartment (see Fig. 1.6), or an isopotential neuron whose dendrites and axons function with instant signal propagation, communicating with other point neurons via metaphysical synapses. Although this thesis does not consider point neurons because there are virtually no dendrites, they are useful in studying models of neuronal membrane potential dynamics (see §1.2.3). In addition, since the groundbreaking work of McCulloch and Pitts [41], especially in the recent decade,

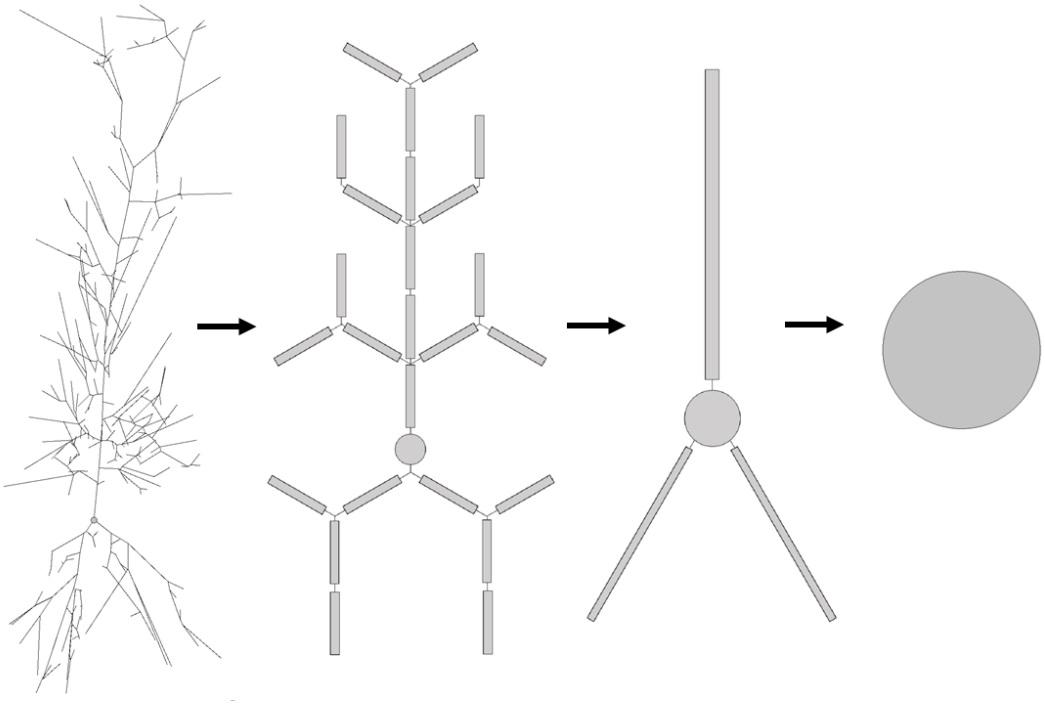

Figure 1.6: Schematic diagram of morphological model reduction at different leveles of the pyramidal cell shown in Fig. 1.4 (up to rotation), from 397 compartments (leftmost), down to 26, 4, and only 1 compartment (rightmost). Although the soma (represented by a disc) in each model here is an isopotential compartment, it is not necessarily the case. For example, the soma in the reconstruction in Fig. 1.4 (which is essentially a multi-compartment model as well) consists of 3 segments.

artificial neural networks consisting of point neurons have proven themselves efficient and powerful in many applications. For example, the automation and digitalisation of neuron tracing mentioned in §1.2.1 have largely benefited from the development of techniques in pattern recognition in the field of machine learning, which heavily employs artificial neural networks.

1.2.3 Membrane potentials

Cell membranes separate intra-cellular plasma from extra-cellular environment in order to maintain cellular homeostasis. Neuronal membranes, in particular, modulate the flows of charged ions selectively by its pore-forming membrane proteins. There are thus differences in ionic densities at the two sides of neuronal membranes, which create a difference between intra- and extra-cellular electric potentials, i.e. membrane potentials. To study the dynamics of membrane potentials, a quantative model based on the analogy of electrical circuits (see Fig. 1.7) can be employed.

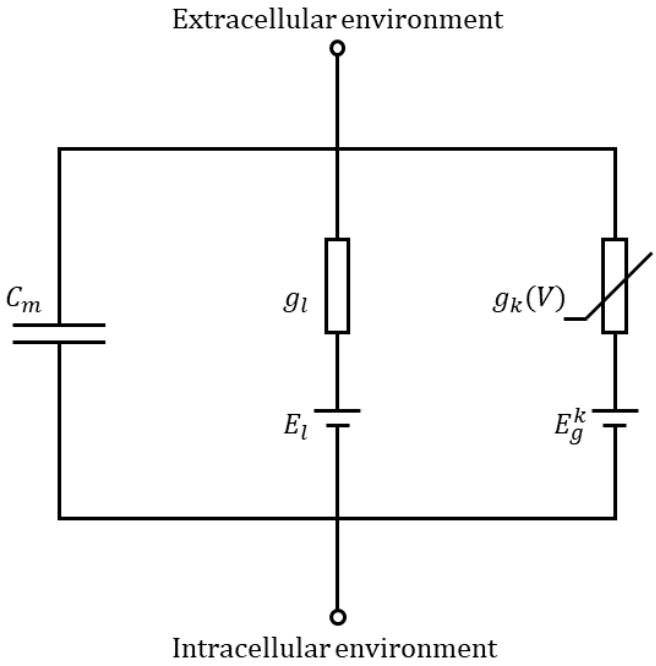

Figure 1.7: A circuit diagram of a general conductance-based model. The membrane potential V is the voltage difference between the intra- and extra-cellular potentials, which is measured at the lipid bilayer, represented by a capacitor. The membrane leakage is analogous to the series circuit of a resistor g_l and a battery E_l, and a voltage-gated ion channel of ionic species k is the series circuit of a non-linear voltage-dependent conductor $g_k(V)$ and a battery E_g^k. If there are multiple ionic species, they are all parallel circuits to one another.

Notably, here a point neuron (introduced in §1.2.2) is assumed, and notations and terms from control theory.

Capacitors: lipid bilayer

The cell membrane of a neuron is a lipid bilayer, which prevents ions at the both sides moving freely across it. It thus behaves as a capacitor, that is, it can be charged up by an injection of a current I_m (generally varying with respect to time t) into the plasma, or mathematically,

$$I_m(t) = C_m A_m \frac{dV}{dt}, \tag{1.1}$$

where C_m is the capacitance per unit area, A_m is the surface area of the membrane, and $V(t)$ is the membrane potential.

Resistors: leakage channels

The lipid bilayer of the cell membrane is not perfectly dielectric, and at the same time there are *leakage* ion channels that allow selective ionic species to travel across the membrane. In reality most of leakage channels behave as rectifiers, that is, they conduct better in one fixed direction than the other. Nonetheless, leakage channels are simply assumed to be resistors (i.e. linear conductors). As they follow Ohm's law, the leakage current can be written as

$$I_l(t) = \sum_k g_l^k A_m (V - E_l^k), \tag{1.2}$$

where g_l^k is the leakage conductance per unit area and E_l^k is the reversal potential of ionic species k. Since both g_l^k and E_l^k are constants predetermined by the ionic species k, the leakage current (1.2) can be therefore recast into a simpler form,

$$I_l(t) = g_l A_m (V - E_l), \tag{1.3}$$

where

$$g_l = \sum_k g_l^k$$

is the total leakage conductance per unit area, and

$$E_l = \frac{\sum_k g_l^k E_l^k}{g_l}$$

is the passive resting membrane potential.

If the membrane potential of a point neuron is determined only by the currents (1.1) and (1.3), Kirchhoff's current law gives

$$I_m(t) + I_l(t) = I_0(t), \tag{1.4}$$

where $I_0(t)$ is the input current. The neuron in this case is purely *passive*. It is equivalent to a resistor-capacitor (RC) circuit, whose output voltage, i.e. solution to Eq. (1.4), is proportional to an exponential-filtered input current.

Inductors: h-channels

Many neurons have the h-channels on their membranes. They permit hyperpoloarisation-activated depolarising I_h currents, and thus prevent the neurons from too strong

hyperpolarisations. The h-channels can be modelled as inductors, that is,

$$\frac{L_h}{A_m}\frac{dI_h}{dt} = -\frac{r_h}{A_m}I_h + (V - E_l), \tag{1.5}$$

where L_h is the inductance and r_h the resistance per unit area.

The neuron whose membrane potential dynamics is determined by the currents (1.1), (1.3) and (1.5) is analogous to an resistor-inductor-capacitor (RLC) circuit, which is also known to be a *resonant* circuit. It is explicitly described by

$$I_m(t) + I_l(t) + I_h(t) = I_0(t), \tag{1.6}$$

where $I_0(t)$ is the input current, and Kirchhoff's current law is applied.

Non-linear conductors: voltage-gated channels

To explain the initiation and the propagation of action potentials in the squid giant axon, the Hodgkin-Huxley model [42] considers a conductance-based model consisting of the currents (1.1), (1.3), and the following two non-linear ion channels,

$$I_{\mathrm{Na}} = \bar{g}_{\mathrm{Na}} m^3 h (V - E_{\mathrm{Na}}), \tag{1.7a}$$

$$I_{\mathrm{K}} = \bar{g}_{\mathrm{K}} n^4 (V - E_{\mathrm{K}}), \tag{1.7b}$$

where $\bar{g}_k = g^k_{\max} A_m$ is the maximal conductance for ionic species $k \in \{\mathrm{K}, \mathrm{Na}\}$ (potassium and sodium), A_m is the surface area of the membrane, and $n, m, h \in [0, 1]$ are gating variables for the activation of potassium channels, the fast activation and the slow inactivation of sodium channels, respectively.

In general, such *voltage-gated* ion channels can be modelled as non-linear conductors, which permit the following current through these channels,

$$I_g(t) = \sum_k g^k_{\max} w^k(V) A_m (V - E^k_g), \tag{1.8}$$

where, for each ionic species k, $g^k_{\max}$ is the maximal active conductance per unit area, E^k_g is the reversal membrane potential, and $w^k(V) \in [0, 1]$ describes the fractions of channels that are open. For any ion species k, in general,

$$w^k(V) = \prod_i n_i^{\eta_i},$$

where the gating variable $n_i \in [0, 1]$ models the probability of ion channel activation

or inactivation at different time scales which changes in V, and η_i is the number of the independent (in)activation gates of the channel. Assume $\alpha_{n_i}(V)$ the opening rate (the transition rate that a channel changes its gating state from close to open) and $\beta_{n_i}(V)$ the closing rate. The gating variable follows

$$\frac{dn_i}{dt} = \alpha_{n_i}(V)(1 - n_i) - \beta_{n_i}(V)n_i, \tag{1.9}$$

which can be recast as

$$\tau_{n_i}(V)\frac{dn_i}{dt} = w^k_\infty(V) - n_i, \tag{1.10}$$

where

$$\tau_{n_i}(V) = \frac{1}{\alpha_{n_i}(V) + \beta_{n_i}(V)}, \tag{1.11}$$

$$n_{i,\infty}(V) = \frac{\alpha_{n_i}(V)}{\alpha_{n_i}(V) + \beta_{n_i}(V)}. \tag{1.12}$$

Thermodynamics suggests the shape of $n_{i,\infty}(V)$ to be a sigmoid function [43], whereas $\alpha_{n_i}(V), \beta_{n_i}(V)$ and η_i can only be obtained by fitting models with experimental data. A general conductance-based model can then be obtained by applying Kirchhoff's current law with the currents (1.1), (1.3) and (1.8), plus an input current $I_0(t)$, that is,

$$I_m(t) + I_l(t) + I_g(t) = I_0(t). \tag{1.13}$$

Since $w^k(V)$ is dependent on V, the current $I_g(t)$ is non-linear, and thus the model is not analytically solvable, whereas the non-linear current can be approximated by a linearised current (in a similar form to I_h) if small enough [19, 44].

Batteries: reversal potentials

The reversal potentials E^k_l, E^k_g in Eqs. (1.2) and (1.8) are analogous to batteries in the electrical circuit. A reversal potential E^k of an ionic species k is defined to be the membrane potential at which the net flow across membrane is zero. It can be derived directly from this definition and is explicitly given by the famous Nernst equation,

$$E^k = \frac{k_B T}{z_k q} \log\left(\frac{N^e_k}{N^i_k}\right),$$

where k_B is the thermal energy in Joules per ion, T is the body temperature in Kelvins and q is the charge of an electron in Coulomb [45]. Since they are all constants and the algebraic charge z_k and the external and internal ionic densities N^e_k, N^i_k are completely predetermined by the ionic species k, E^k is assumed to be

constant from the beginning of all neuronal models in this thesis.

1.2.4 Cable theory

In 1952, Hodgkin and Huxley [42] successfully explained the initiation and the propagation of action potentials in the squid giant axon by a cable equation with nonlinear voltage gated channels. The model was a milestone in the development of neuronal cable theory, it won Hodgkin and Huxley a Nobel Prize in 1963, and it has been since known as the *Hodgkin-Huxley model*. As a matter of fact, about a century before that, Von Helmholtz [46] experimentally measured the signal velocity in nerve fibers of a frog, and only a few years later Thomson [47] developed the prototypic cable theory to study transmission of telegraphic signals in long cables, which established the theoretical foundation of cable theory but its relevance to neuronal cables was not noticed upon that time. With the development of sharp micropipette electrodes, dynamics of dendritic membrane potentials also started to be revealed by intra-cellular recordings, and their observations can be elaborated by *dendritic cable theory*. The theory was thoroughly studied by Wilfrid Rall, whose significant contribution to the topic is well summarised in the book of Segev et al. [48]. Classical cable theory essentially extends the models for a point neuron (discussed in §1.2.3) to a neuronal cable [49, 50], and dendritic cable theory aims to apply cable theory on a complex dendritic morphology.

It is ideal to build models of dendritic membrane potential dynamics in the three-dimensional space, because *"any other approach risks excluding important features of the three-dimensional structure or incorporating three-dimensional features incorrectly"* [51]. Nonetheless, the standard cable equation is one-dimensional in space, since all radial currents are assumed to be transmembrane, an assumption can be justified by the fact that the diameter of a typical neurite is considerably small comparing to its length [52]. It is also shown in [51] that the one-dimensional standard cable equation is the limit of their three-dimensional model given common assumptions. Below I first derive the general cable equation of a single dendritic branch with continuously varying radius $r(x)$, into which an input current $I_{in}(x;t)$ is applied. It is then straightforward to obtain the classical standard cable equation and other simplified models.

General cable equation

To begin with, I focus on a little section of the dendritic branch from x to $x + \Delta$. Kirchhoff's current law (the conservation of electrical currents at a point) gives

$$I_m(x) + I_l(x) + I_g(x) + I(x + \Delta) + I_{in}(x + \Delta) = I(x) + I_{in}(x), \tag{1.14}$$

where $I(x)$ is the axial current flowing into the section and $I(x + \Delta)$ is the axial current flowing out. The other currents can be found in Eqs. (1.1), (1.3) and (1.8). Substituting them into Eq. (1.14) leads to

$$C_m \frac{\partial V}{\partial t} + g_l(V - E_l) + \sum_k g^k_{\max} w^k (V - E^k_g) = \frac{I(x) - I(x + \Delta) + I_{in}(x) - I_{in}(x + \Delta)}{A_m(x, x + \Delta)}, \tag{1.15}$$

where the surface area of the section is

$$A_m(x, x + \Delta) = 2\pi \int_x^{x+\Delta} \rho(s) ds, \tag{1.16}$$

and

$$\rho(s) = r(s)\sqrt{1 + (r'(s))^2}, \tag{1.17}$$

as the cross-sectional area is assumed to be perfectly round. Only the right hand side of Eq. (1.15) depends on Δ and thus by taking the limit $\Delta \downarrow 0$,

$$\lim_{\Delta \downarrow 0} \left[-\frac{[I(x + \Delta) - I(x) + I_{in}(x + \Delta) - I_{in}(x)]/\Delta}{A_m(x, x + \Delta)/\Delta} \right] = -\frac{\partial I/\partial x + \partial I_{in}/\partial x}{2\pi\rho(x)}. \tag{1.18}$$

If the input current of a total strength of I_{inj} is injected only into the section from y to $y + \Delta$, given the same limit $\Delta \downarrow 0$,

$$\left. \frac{\partial I_{in}}{\partial x} \right|_{y^+} = -I_{\text{inj}} \delta(x - y), \tag{1.19}$$

where $\delta(x - y)$ is the Dirac delta function. Without loss of generality, from now on all input currents are assumed to be point processes. It is worth noting that the results for a region of input can be recovered by integrating over the input region.

At the same time, the axial current $I(x)$ flowing through the section can be calculated by Ohm's law, that is,

$$V(x + \Delta) - V(x) = -I(x)R, \qquad R = \frac{R_a \Delta^2}{\int_x^{x+\Delta} A_c(s) ds}, \tag{1.20}$$

where R_a is the axial resistivity and $A_c(x) = \pi r^2(x)$ is the cross-sectional area. It follows from the above equations that

$$I(x) = -\frac{\int_x^{x+\Delta} A_c(s)ds}{R_a\Delta}\frac{V(x+\Delta)-V(x)}{\Delta},$$

and again with the limit $\Delta \downarrow 0$,

$$I(x) = -\frac{1}{r_a}\frac{\partial V}{\partial x}, \tag{1.21}$$

where

$$r_a(x) = \frac{R_a}{\pi r^2(x)}, \tag{1.22}$$

is the axial resistance. Thus,

$$\frac{\partial I}{\partial x} = -\frac{\pi}{R_a}\frac{\partial}{\partial x}\left[r^2(x)\frac{\partial V}{\partial x}\right]. \tag{1.23}$$

The general cable equation of a radius-varying dendritic cable with non-linear channels are obtained by substituing Eqs. (1.19) and (1.23) into Eq. (1.18), that is,

$$C_m\frac{\partial V}{\partial t} = -g_l(V-E_l) - \sum_k g^k_{\max}w^k(V-E^k_g) + \frac{1}{2R_a\rho(x)}\frac{\partial}{\partial x}\left[r^2(x)\frac{\partial V}{\partial x}\right] + I_0, \tag{1.24}$$

where

$$I_0 = \frac{I_{\text{inj}}\delta(x-y)}{2\pi\rho(x)} \tag{1.25}$$

could be considered as the driving force in Eq. (1.24), and is notably determined only by the input location y (not x), because $\delta(x-y) = 0$ if and only if $x = y$.

Simplified cable equations

As most of voltage-gated channels are non-linear, Eq. (1.24) is generally impossible to solve analytically. Nonetheless, in the sub-threshold regime, they could be linearised (see §1.2.3). For simplicity, here I consider only h-channels which permit I_h currents. Substituting the non-linear currents (1.24) by the I_h current (1.5), the *resonant (quasi-active) tapered cable equation* is obtained,

$$C_m\frac{\partial V}{\partial t} = -g_l V - I_h + \frac{1}{2R_a\rho(x)}\frac{\partial}{\partial x}\left[r^2(x)\frac{\partial V}{\partial x}\right] + I_0, \tag{1.26a}$$

$$L_h\frac{\partial I_h}{\partial t} = -r_h I_h + V. \tag{1.26b}$$

where notably the membrane potential is from now on measured from E_l.

A further simplification is to remove the I_h current from the model. It can be experimentally realised by blocking the h-channels, and is mathematically equivalent to take the limit $r_h \to +\infty$. The *passive tapered cable equation* is thus obtained,

$$C_m \frac{\partial V}{\partial t} = -g_l V + \frac{1}{2R_a \rho(x)} \frac{\partial}{\partial x} \left[r^2(x) \frac{\partial V}{\partial x} \right] + I_0. \tag{1.27}$$

An alternative simplification of the system (1.26) is to assume constant dendritic radius $r(x) = r_c$ while keeping the I_h current in the model, which gives the *resonant cylindrical cable equation*,

$$C_m \frac{\partial V}{\partial t} = -g_l V - I_h + \frac{r_c}{2R_a} \frac{\partial^2 V}{\partial x^2} + I_0, \tag{1.28a}$$

$$L_h \frac{\partial I_h}{\partial t} = -r_h I_h + V. \tag{1.28b}$$

Reducing the model with both simplifications results in the *passive cylindrical cable equation*, i.e. the classical standard cable equation,

$$C_m \frac{\partial V}{\partial t} = -g_l V + \frac{r_c}{2R_a} \frac{\partial^2 V}{\partial x^2} + I_0, \tag{1.29}$$

or, in a more well known form,

$$\tau_m \frac{\partial V}{\partial t} = -V + \lambda^2 \frac{\partial^2 V}{\partial x^2} + \frac{I_0}{g_l}, \tag{1.30}$$

where

$$\lambda^2 = \frac{r_c}{2 g_l R_a}, \tag{1.31}$$

and $\tau_m = C_m / g_l$ is defined by Eq. (5.4). It is worth noting that the tapered cable equations (1.26) and (1.27) work for general radius-varying dendrites as clearly shown in the derivation, not only for "tapered cables". The term "taper" is chosen because the tapered dendrites are to be investigated in more details in **Chapter 3**. This thesis mainly studies these simplified cable equations (1.26), (1.27) and (1.28) due to their mathematical tractability.

Input currents

An input current can be produced due to synaptic activities, or directly from experimental injection. An input current in either case is considered as a point process with its location specified by $\delta(y)$. The duration and strength of the input is de-

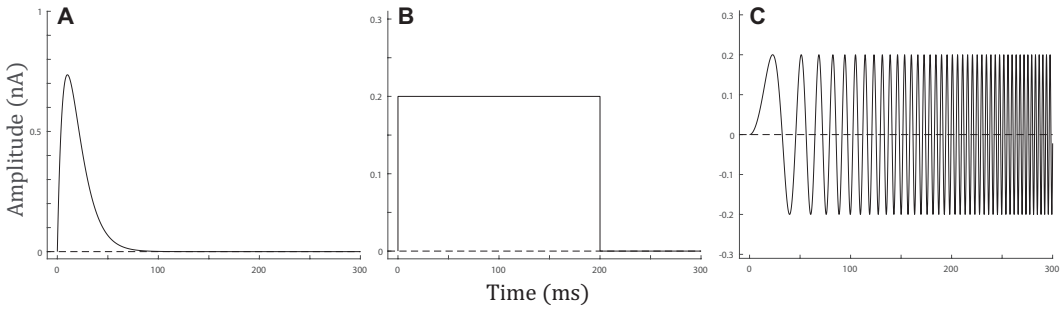

Figure 1.8: Current profiles of three types of inputs with $A_0 = 0.2$ nA. (**A**): An EPSC modelled by an alpha function (1.32) with $B_0 = 0.1$. (**B**): A rectangle input (1.33). (**C**): A chirp current (1.34) with $\omega_{\text{chirp}} = 0.003$ kHz.

termined by $I_{\text{inj}}(t)$. If $I_0 = 0$, the cable equations (1.26) - (1.29) are homogeneous differential equations. Since they are all linear, the solutions to the corresponding heterogenous equations with different $I_0 \neq 0$ are additive. Therefore, it is straightforward to generalise the input from a point process to a field.

The time profiles of $I_{\text{inj}}(t)$ can vary from cell to cell due to different synaptic activities, or from case to case under different experimental protocols. For simplicity, an excitatory post-synaptic current (EPSC) can be modelled by the alpha function (see Fig. 1.8A) [53–56],

$$I_{\text{EPSC}}(t) = A_0 t e^{-B_0 t}, \tag{1.32}$$

for $t = 0$ the time the post-synaptic neuron starts to depolarise due to synaptic activities. The function reaches the maximal value of $A_0(B_0 e)^{-1}$ at time $t = B_0^{-1}$. However, any post-synaptic current is actually dependent on the temporal membrane potential at its location; Eq. (1.32) is notably an extremely simplified model of an EPSC in the case of no shunting currents that would have varied the membrane conductance are presented. This model can be useful for experiments investigating single neurons *in vitro*, whereas it is probably unrealistic for neurons *in vivo*, since they could constantly receive signals from thousands of synapses.

In addition, rectangle inputs and a chirp currents (see Fig. 1.8B,C) are also widely employed in experiments to investigate the asymptotic and oscillating behaviours of electrical systems respectively. The rectangle input can be described by

$$I_{\text{rect}}(t) = A_0 H(t - t_0) H(t_0 + \tau_{\text{rect}} - t), \tag{1.33}$$

where A_0 is the strength of the current, $H(t)$ is the Heaviside function, t_0 is the onset

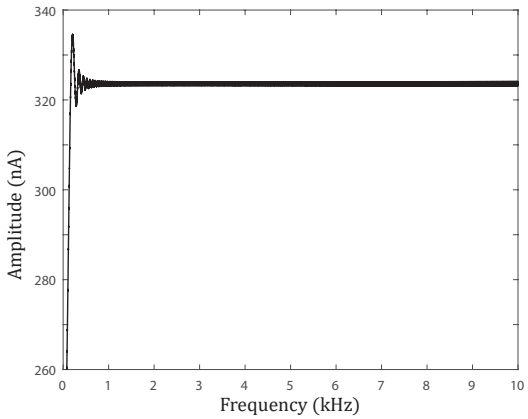

Figure 1.9: Amplitude of the chirp current in Fig. 1.8B in the Fourier frequency domain.

time of the stimulus, and τ_{rect} is its duration. If $\tau_{\text{rect}} \to +\infty$, the input becomes a step current. A step current drives a neuron to some new steady-state voltage. It can be employed to find input and tranfer impedances (see §1.3.2) and is thus usually a primary indicator of signal attenuation on dendrites.

The chirp current can be defined as

$$I_{\text{chirp}}(t) = A_0 \sin\left(\omega_{\text{chirp}} t^2\right), \tag{1.34}$$

whose instantaneous frequency can be found as

$$f(t) = \frac{1}{2\pi}\frac{d}{dt}\left(\omega_{\text{chirp}} t^2\right) = \frac{\omega_{\text{chirp}}}{\pi} t,$$

where $\omega_{\text{chirp}}/\pi$ is the chirpyness, i.e. the rate of frequency. As the frequency is varying linearly in time, Eq. (1.34) particularly defines a linear chirp. Since the amplitude of the response in the Fourier domain is almost constant for a wide range of frequencies (see Fig. 1.9), which implies that the power spectrum of the chirp input is similar to that of a Dirac delta impulse, the envelope of the corresponding oscillating response in time domain roughly traces the Green's function (which is by definition the response of a Dirac delta input). Therefore, such chirp inputs are useful in experiments to characterise resonant systems. It is worth noting that, however, the phases of a chirp input and a Dirac delta impulse are different, and thus the chirp responses cannot provide an accurate experimental measurement of the Green's function.

Boundary conditions

Membrane potential dynamics on all individual branches of a dendritic tree are modelled by the system (1.26) in this thesis, whereas different branches in general have different morphological or electrophysiological parameters. Moreover, four types of boundary conditions (see Fig. 1.10) are considered. They are enforced at the nodes where dendritic branches are connected or terminated. All boundary conditions are determined by two physical contraints, Kirchhoff's current law and the continuity of membrane potentials. The study of dendritic cable theory in this thesis is basically the mathematical analysis of the system (1.26) given all boundary conditions. Notably in this section the spatial coordinate is changed case by case so that the boundary under investigation is at the location $x = 0$, whereas it is common to fix the coordinate globally when studying a particular neuronal model.

A *terminal* is the end of a dendritic branch. It is assumed to be either open or closed. An open terminal means that there is no barrier for ions to move freely into or out from the neuron, which corresponds to the situation where the dendritic branch is cut off at $x = 0$. Mathematically,

$$V(0;t) = 0. \tag{1.35}$$

In this thesis I assume the terminal of a natural dendritic branch is closed, that is, there are no axial currents at $x = 0$, which gives

$$\frac{\partial V}{\partial x}(0;t) = 0. \tag{1.36}$$

A *branching node* is a point at which several dendritic branches are attached together. Assume there are N branches attached to the point $x = 0$. The two conditions for axial currents and membrane potentials respectively give

$$\sum_{i=1}^{N} \frac{1}{r_{a,i}(0)} \frac{\partial V_i}{\partial x}(0;t) = 0, \tag{1.37}$$

$$V_i(0;t) = V_j(0;t), \tag{1.38}$$

for $i, j \in \{1, 2, 3, \ldots, N\}$ indexing the different branches, where $r_{a,i}$ is the axial resistance for branch i, whose definition can be found in (1.22).

A *soma* is treated as an isopotential sphere that is mathematically equivalent to the model of a point neuron as in §1.2.3. Similarly only the resonant model is employed for the soma, and its active properties are to be discussed in §5.1.4. Given

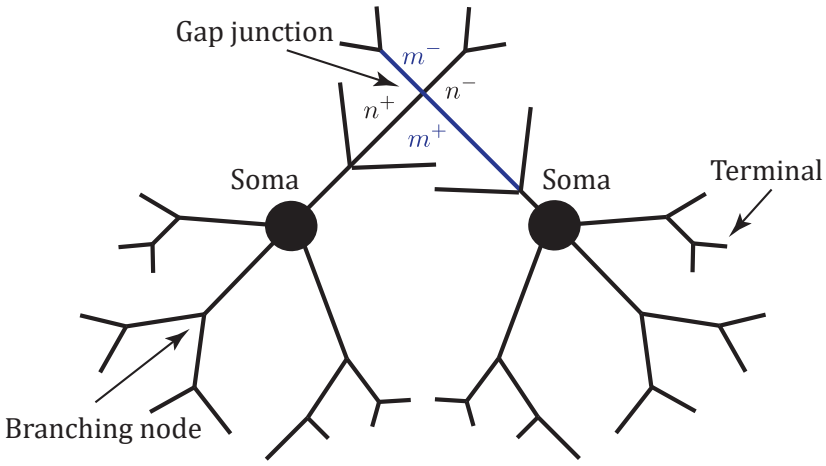

Figure 1.10: A schematic of a network of two neurons connected by a gap junction.

the somatic parameters $C_S = C_{\text{soma}} A_{\text{soma}}$, $g_S = g_{\text{soma}} A_{\text{soma}}$, $L_S = L_{\text{soma}}/A_{\text{soma}}$, $r_S = r_{\text{soma}}/A_{\text{soma}}$, the explicit conditions for the somatic node can be written as

$$C_S \frac{\partial V_S}{\partial t} = -g_S V_S + \sum_{i=1}^{N} \frac{1}{r_{a,i}(0)} \frac{\partial V_i}{\partial x}(0;t) - I_S(t), \tag{1.39a}$$

$$L_S \frac{\partial I_S}{\partial t} = -r_S I_S(t) + V_S(t), \tag{1.39b}$$

$$V_S(t) = V_i(0;t), \tag{1.39c}$$

where V_S is the somatic membrane potential, I_S is the somatic resonant current, and V_i is the membrane potential of the dendritic branch i. Eqs. (1.39a) and (1.39b) are imposed by the Kirchhoff's current law and Eq. (1.39c) by the continuity of membrane potentials.

In addition, electrical synapses are considered, which are also known as *gap junctions*. A gap junction is a mechanical coupling between adjacent neurons that permits direct ion flows between them without a orientation preference, which can be simply modelled by resistors whose conductance is $g_{GJ} = R_{GJ}^{-1}$ [20]. This assumption is able to elaborate the observations that a signal passing through a gap junction always attenuates but is almost instant. Explicitly, it follows Ohm's law,

$$\frac{1}{r_{a,m}} \left[\frac{\partial V_{m^-}}{\partial x}(0;t) + \frac{\partial V_{m^+}}{\partial x}(0;t) \right] = g_{GJ}(V_{m^-}(0;t) - V_{n^-}(0;t)), \tag{1.40a}$$

$$\frac{1}{r_{a,n}} \left[\frac{\partial V_{n^-}}{\partial x}(0;t) + \frac{\partial V_{n^+}}{\partial x}(0;t) \right] = g_{GJ}(V_{n^-}(0;t) - V_{m^-}(0;t)), \tag{1.40b}$$

where m^- and m^+ (n^- and n^+) are the two segments of dendritic branch m (branch n) before and after the gap junction. At the same time, the membrane potentials are continuous on the same branches, that is,

$$V_{m^-}(0;t) = V_{m^+}(0;t), \tag{1.41a}$$

$$V_{n^-}(0;t) = V_{n^+}(0;t). \tag{1.41b}$$

We can thus consider not only a single neuron, but also multiple neurons coupled by gap junctions, while keeping the entire model relatively simple.

1.3 Solutions by Green's function formalism

In order to obtain the solution to the cable equations, a classical approach is to solve them without the input currents I_0 first. For example, Eq. (1.29) without I_0 is simply a one-dimensional heat equation (with an additional term of heat loss), which is homogeneous. It can be solved analytically by separation of variables. I_0 can be then added back into the system, playing a role of initial and boundary conditions. Alternatively, the Green's function formalism is employed in this thesis to solve the resonant tapered cable equation (1.26) and its simplifications, because they are all diffusion equations that can reduce to Helmholtz equations, whose Green's function is known. A Green's function is an impulse response to an inhomogeneous linear differential equation. It is conventionally a tool for solving inhomogeneous linear differential equations, first developed by and thus later named after the British mathematician, George Green [57]. While the term *fundamental solution* is preferred instead in modern mathematics, especially in distribution theory [58], Green's functions are still commonly employed in many-body problems in physics, and are called *propagators* when it comes to quantum mechanics [59, 60]. In control theory (or linear time-invariant theory), *transfer functions*, a term appearing regularly in frequency domain analysis, are no more than Green's functions in the frequency domain [61]. In this thesis the term *Green's function* is consistently employed, whereas occasionally I refer to the other terms when linking to works of others.

In general, a Green's function is defined as,

$$LG(\alpha, \beta) = \delta(\beta - \alpha), \tag{1.42}$$

where L is a linear differential operator. It is thus employed to solve inhomogeneous

linear differential equations of the form,

$$Lu(\alpha) = f(\alpha),$$

where $\alpha, \beta \in \mathbb{R}^n$, because the solution can be directly written as

$$u(\alpha) = \int G(\alpha, \beta) f(\beta) d\beta + f_0, \tag{1.43}$$

where f_0 is a constant, often determined by initial conditions, or simply,

$$u = G * f + f_0, \tag{1.44}$$

where $*$ represents the convolution of the two functions. In this thesis, $f(\beta) = I_0(x;t)$ represents input currents into a dendritic tree at some location and time, while $u(\alpha) = V_m(x;t)$ represents output membrane potentials measured at some other location and time. This thesis is focused on finding Green's functions on dendritic trees, because they establish direct and complete relations between input currents and output membrane potentials, and encode all together the information of dendritic geometrical and electrophysiological properties. Formally, I consider the geometry modelled by a metric graph $\Gamma = (V, E)$ for V the set of vertices and E the set of edges in the graph. Since each edge $e \in E$ is equipped with a differential operator D_e acting on the function of membrane potential dynamics, Γ is a *quantum graph* (see [62, 63] for a review). Therefore, in mathematical terms, this thesis attempts to find the following mapping,

$$\mathcal{M} : (\Gamma, \alpha, \beta) \to G_\Gamma(\alpha, \beta), \tag{1.45}$$

which determines the Green's function G_Γ for any Γ that satisfies the modelling criteria in this thesis, given arbitrary output-input pairs (α, β). The differential operator D_e in this thesis is mainly the Helmholtz operator. Their Green's functions can be constructed by the path integral formulation, that is, the Green's function $G_\Gamma(\alpha, \beta)$ is found by summing over all the random walk paths between α and β on the quantum graph Γ. Notably I consider only the deterministic limit in this thesis, whereas realistic neuronal membrane potential dynamics is stochastic. By the law of large numbers, it should be justified that such deterministic limits well describe average behaviours of the membrane potentials, as there are a large number of charged ions moving inside neurons or across cell membranes.

1.3.1 Properties of Green's functions

Below several important properties of Green's functions are discussed. They generally work for any linear systems.

A chain of convolutions

Assume $L = L_1 L_2$ and G_1, G_2 are the Green's functions of L_1, L_2 respectively. By applying Eq. (1.44) twice with respect to L_1, L_2 in order,

$$u = G_2 * G_1 * f, \tag{1.46}$$

and, if G is the Green's function of L,

$$G = G_2 * G_1, \tag{1.47}$$

or explicitly,

$$G(\alpha, \beta) = \int G_2(\alpha, \zeta) G_1(\zeta, \beta) d\zeta. \tag{1.48}$$

By mathematical induction, the corollary of a chain of convolution follows,

$$G = G_N * G_{N-1} * \cdots * G_2 * G_1, \tag{1.49}$$

if $L = L_1 L_2 L_3 \dots L_N$, where G_k is the Green's function of the linear operator L_k for $k \in \{1, 2, 3, \dots, N\}$, and G is the Green's function of L.

Linear time-invarient system

The resonant cable equation (1.26) is by definition a linear system. It is also easy to see that the system is time-invariant because all the coefficients in the differential equations are constant in t. It is thus a linear time-invariant (LTI) system, whose Green's function with respect to t can be rewritten in a convenient way, that is,

$$G(t, t_0) = G(t - t_0). \tag{1.50}$$

Moreover, an LTI system can be completely characterised by the Green's function, because the output is simply

$$u(t) = \int_{-\infty}^{\infty} G(t - t_0) f(t_0) dt_0, \tag{1.51}$$

which is essentially a special case of Eq. (1.43).

Due to Eq. (1.49), Eq. (1.50) can be extended to a series of time points t_0, t_1, $t_2, \ldots, t_N = t$,

$$G(t, t_0) = G(t - t_0) = G(t - t_{N-1})G(t_{N-1} - t_{N-2}) \ldots G(t_2 - t_1)G(t_1 - t_0). \quad (1.52)$$

Additivity of multiple inputs

The additivity of multiple inputs is essentially determined by the linear operator, which leads to

$$V(x, \mathbf{y}; \omega) = \mathbf{G}(x, \mathbf{y}; \omega){\mathbf{I_0}}^T(\mathbf{y}; \omega), \quad (1.53)$$

where $\mathbf{y} = (y_1, y_2, y_3, \ldots, y_N)$ is an array of N input locations, and $\mathbf{G}, \mathbf{I_0}$ are arrays of size N whose individual elements are successively defined by the corresponding elements of $\mathbf{y}$. Moreover, Eq. (1.53) can be easily rewritten into an integration form in y, by assuming the points of $\mathbf{y}$ locate closely in a certain region and taking the limit so that these points are continously distributed, that is,

$$V(x, y; \omega) = \int G(x, y; \omega) I_0(y; \omega) dy, \quad (1.54)$$

where $I_0(y; \omega)$ is a region of input that has a continuous density in amplitude. This enables calculation of general inputs directly from the point processes assumed by Eq. (1.19).

Notably the property (1.53) is purely a mathematical result, which is approximately valid only if the individual inputs are small or distant enough. For example, when an experimentalist injects a single current into a dendritic branch. However, it has been long since the existence of non-linear interactions of synaptic inputs on dendrites were discovered [64], and a typical neuron *in vivo* could constantly receive thousands of inputs due to synaptic activities. A single input is assumed throughout this thesis; I will leave the discussion of such non-linear behaviours in §5.1.5.

Reciprocity between input and output

Since the resonant cable equation (1.57) (in the frequency domain) is a second order linear ordinary differential equation, it can be rewritten in the Sturm-Liouville form. Since the Sturm-Liouville operator is self-adjoint, the Green's function must be symmetric [65], that is,

$$G(x, y) = G(y, x), \quad (1.55)$$

which is known to be the reciprocity principle. This result can notably be generalised from a single cable to a dendritic tree given appropriate boundary conditions.

Nonetheless, I will give an alternative proof of the reciprocity on dendrites in §2.3.3.

1.3.2 Laplace and Fourier transforms

The Laplace transform $\mathcal{L}$ of a function $f(t)$ is defined as

$$F(\omega) = \mathcal{L}\{f(t)\} = \int_0^\infty f(t)e^{-\omega t}dt, \tag{1.56}$$

where ω is the complex frequency.

Applying the Laplace transform on Eq. (1.26) results in

$$\mathcal{E}(\omega)V(x;\omega) = \frac{1}{2R_a\rho(x)}\frac{\partial}{\partial x}\left[r^2(x)\frac{\partial V(x;\omega)}{\partial x}\right] + I_0(\omega) + U_0(\omega), \tag{1.57}$$

where

$$\mathcal{E}(\omega) = C_m\omega + g_l + \frac{1}{r_h + L_h\omega}, \tag{1.58}$$

$$U_0(\omega) = C_mV(t=0) + \frac{L_hI_h(t=0)}{r_h + L_h\omega}. \tag{1.59}$$

As it is an LTI system, it is safe to assume zero initial conditions, that is, $V(t = 0) = I_h(t = 0) = 0$, which gives $U_0 = 0$. Since a Green's function in the frequency domain is one-to-one correspondence to a Green's function in the time domain, it completely characterises the system. In addition, convolution in the time domain is equivalent to multiplication in the frequency domain, that is, Eq. (1.51) becomes

$$u(\omega) = G(\omega)f(\omega), \tag{1.60}$$

which is easier to analyse and compute.

To recover the function in time domain, the inverse Laplace transfrom $\mathcal{L}^{-1}$ is employed,

$$f(t) = \frac{1}{2\pi i}\int_{c-i\infty}^{c+i\infty} F(\omega)e^{t\omega}d\omega, \tag{1.61}$$

for c an arbitrary real number that guarantees the coutour integration to be convergent with respect to $F(\omega)$.

At the same time, the Fourier transform is defined as

$$\hat{f}(\bar{\omega}) = \int_{-\infty}^{\infty} f(t)e^{-i\bar{\omega}t}dt. \tag{1.62}$$

Although the Fourier frequency $\bar{\omega}$ is usually understood as a real number, it can be

in general treated as complex, in which cases the two transforms (1.56) and (1.62) are indifferent as long as $f(t) = 0$ for $t < 0$, which is assumed throughout this thesis.

If $\bar{\omega}$ is real valued, the Fourier frequency is then merely the complex component of the Laplace frequency, which characterises the periodic behaviours of the system, while the real component of the Laplace transform is responsible for the transient behaviours. Moreover, the inverse Fourier transform,

$$f(t) = \frac{1}{2\pi} \int_{-\infty}^{\infty} \hat{f}(\bar{\omega}) e^{-it\bar{\omega}} d\bar{\omega}, \tag{1.63}$$

is equivalent to the inverse Laplace transform (1.61), if c can be chosen as zero, that is, if all singularities are in the left half-plane. It is worth noting that this condition roughly implies that there exists some $F(\omega)$, such that c cannot be set as zero, in which cases the inverse Fourier transform will not converge. However, this thesis does not give any mathematical proof on whether or not the two transforms are interchangeable for any particular Green's function, because it will be easier to check the convergence after obtaining explicit expressions.

Although the terminology for the Laplace transform will be employed for consistency, it is more convenient particularly in numerical integrations to use the Fourier transform because algorithms of the fast Fourier transform (and its inverse) is efficient and accurate.

Final values of responses

By injecting a step current into a neuron, it is expected that the entire system finally reaches some steady state. Assume $I_{\text{inj}}(t) = I_{\text{step}}(t)$ is the step input of strength A_0 occuring at time t_0. It is the special case of a rectangle input (1.33), whose Laplace transform can be found as,

$$I_{\text{step}}(\omega) = \frac{A_0}{\omega} e^{-t_0 \omega}. \tag{1.64}$$

In order to obtain the final value, the *final value theorem* for the Laplace transform can be applied, which states that,

$\lim_{t\to\infty} f(t) = \lim_{\omega\to 0} \omega F(\omega)$, *if all poles of* $\omega F(\omega)$ *are in the left half-plane.*
By the theorem,

$$V(x, y; t) = G(x, y; t) * I_{\text{inj}}(t) = \mathcal{L}^{-1}\{G(x, y; \omega) I_{\text{inj}}(\omega)\}, \tag{1.65}$$

which simply gives

$$\lim_{t\to\infty} V(x,y;t) = \lim_{\omega\to 0} \omega \left[G(x,y;\omega)\frac{A_0}{\omega} e^{-t_0\omega} \right] = A_0 G(x,y;\omega=0). \tag{1.66}$$

For a passive system $G(x,x;\omega=0)$ is by definition the input resistance at x, because A_0 in the strength of the injected current and $\lim_{t\to\infty} V(x,x;t)$ is the steady state voltage. However, this measure cannot fully characterise a resonant neuron, as overshoots and undershoots are to be observed before the system reaches to its steady state.

In order to account for the oscillating behaviours of a neuron, a sinusoidal signal of the following form,

$$I_{\sin}(t) = A_0 \sin(\omega_0 t), \tag{1.67}$$

can be applied to the system. The system will reach a sinusoidal final state,

$$V_{\mathrm{SS}}(x,y;t) = B_0 \sin(\omega_0 t + \phi_K), \tag{1.68}$$

where the amplitude,

$$B_0 = A_0 |K(x,y;\omega)|, \tag{1.69}$$

and the phase shift,

$$\phi_K = \arg(K(x,y;\omega)), \tag{1.70}$$

can be found with $K(x,y;\omega) = G(x,y;\bar{\omega})$ where $\bar{\omega} = i\omega$ for real ω [61].

Therefore, the Green's function can be obtained experimentally by measuring the sinusoidal final state responses to sinusoidal inputs with all frequencies. Koch [44] terms $K(x,y;\omega)$ as the frequency-dependent transfer impedance, and in particular $K(x,x;\omega) = G(x,x;\bar{\omega})$ is the input impedance, which is a generalisation of the input resistance $G(x,x;\omega=0)$. Recall the implication of chirp inputs introduced in §1.2.4. Since the frequencies are instanteously varying, the system in principle never reaches any sinusoidal final state (1.68), which is the reason why the envelope of the oscillating response can only roughly, but never accurately, capture the shape of the Green's function.

1.4 Summary

In this chapter, I have presented an overview of this thesis in §1.1, an introduction to the mathematical models of neuronal dendrites, and a mathematical formalism for investigating them.

In §1.2, dendritic cable theory is established. Firstly, the technique of neural tracing is briefly reviewed. It provides us with the raw data of neuronal morphologies in the form of digital recontructions. By assuming dendritic lengths much longer than dendritic radii, the branching tree structure of dendrites is formally modelled by a metric graph. Secondly, the cable equations are derived to describe membrane potential dynamics on dendritic branches. They are subjected to several boundary conditions, enforced by nodes in the dendritic tree, and an initial condition, provided by a single current input. The Green's function formalism is then introduced in §1.3. It can be employed to solve the linear cable equations.

Chapter 2

Local Point Matching on Cylindrical Dendrites

2.1 Introduction

In the previous chapter, resonant dendritic cable theory is derived. Since there are in general many boundary conditions on an arbitrary dendritic tree, it is not trivial to obtain response functions analytically. Nonetheless, the early works [66, 67] have shown that response functions (in the frequency domain) on resonant cylindrical dendrites can be found in closed analytical forms. Although nowadays numerical simulations on reconstructed neurons can be performed by exisiting environments, e.g. NEURON [68], analytical solutions are still useful in theoretical analysis, because they are written explicitly in terms of all the parameters.

In this chapter, I employ an approach first established in [18] for obtaining Green's functions on a passive cylindrical dendritic tree by the path integral formulation of quantum mechanics (in §2.2). The approach was later termed as *sum-over-trips* [69]. It is recently generalised in [19] for resonant dendritic trees, and in [20] for neuronal networks coupled by gap junctions. The inclusion of gap junctions admits the possibility of the presence of loops in a neuronal network, and the methods by [66, 67] cannot deal with such loops (reviewed in §2.3). This sum-over-trips approach bypasses the non-trivial boundary condition problem by encoding the information of boundary conditions into factors to be used when constructing Green's functions. However, such a solution is in terms of an infinite sum, which converges badly in numerical computations [70]. The novel method of local point matching is developed to overcome this problem (see §2.4). It is based on the framework of sum-over-trips but solutions are in closed algebraic forms, and thus theoretical analysis and numerical computations can be conducted more accurately and efficiently.

2.2 Path integral on passive dendrites

To begin with, consider cylindrical dendrites whose membrane potential dynamics is described by the passive cylindrical cable equation (1.30). The equation can be recast into the following form,

$$\frac{\partial V}{\partial T} = \frac{\partial^2 V}{\partial X^2} - V + I_c(X;T), \tag{2.1}$$

where

$$I_c(X;T) = \frac{I_{\text{inj}}(t)\delta(x-y)}{2\pi r_c g_l}, \tag{2.2}$$

by absorbing the constants τ_m and λ defined in (5.4) and (1.31) into the differential operator, that is, introducing the following dimensionless temporal and spatial

variables,

$$T = \frac{t}{\tau_m}, \tag{2.3}$$

$$X = \frac{x}{\lambda}. \tag{2.4}$$

2.2.1 Random walks on an infinite cable

In order to obtain the Green's function of Eq. (2.1), we can apply the path integral formulation. We firstly construct a set of random walks starting from X and terminating at Y of duration T. The number of such random walks are infinite, and each of them becomes a stochastic process continuous in time as the step size becomes infinitesimal. We can thus find the Green's function by averaging over all the continuous stochastic process.

An infinite cable

First, consider a single cable of an infinite length, that is, Eq. (2.1) is subject to no boundary conditions. Any random walk is constructed to start from X, to move forwards or backwards by length $(2t/N)^{1/2}$ along it with equal probability $p_0 = 1/2$ at each step, and to stop after N steps in a total time T. By averaging all (infinitely many) the random walks of infinitesimal step sizes, we obtain

$$G_0(X - Y; T) = \lim_{N \to +\infty} \lim_{P \to +\infty} \sum_{\text{from } x \text{ to } y}^{\text{paths}} \exp(-T), \tag{2.5}$$

where P is the number of such paths. By the path integral formulation [18], Eq. (2.5) is the Green's function of Eq. (2.1) on the infinite cable, and can be rewritten in the following compact form,

$$G_0(X - Y; T) = \frac{1}{2\sqrt{\pi T}} \exp\left[-\frac{(X - Y)^2}{4T} - T \right]. \tag{2.6}$$

A semi-infinite cable

Here we still consider a single cable of an infinite length. However, it has an open or closed terminal at the origin $X = 0$. We call such cables "semi-infinite".

Now Eq. (2.1) is subject to a single boundary condition (1.35) or (1.36) at $X = 0$, which implies that $G(0, Y; T)$, the Green's function of Eq. (2.1) evaluated at $X = 0$, also satisfies either boundary condition. From the path integral point of view, the random walk is the same as in the previous case except for the origin, where the

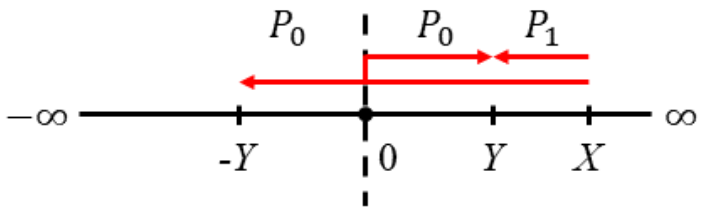

Figure 2.1: Partitions of random walks on an infinite cable starting from X. All the random walks terminating at $-Y$ must pass through the origin $X = 0$, namely P_0. By the reflection principle, there is an equal number of random walks reflecting at the origin and terminating at Y. In addition, the other partition of the random walks terminating at Y does not touch the origin, namely P_1.

probability of escaping from the cable is 1 for the open terminal, and 0 for the closed terminal. On the infinite cable, for $X, Y > 0$,

$$G_0(X - Y; T) = P_0 + P_1, \tag{2.7}$$

where P_0 is the sum of all paths that touch the origin and P_1 is the sum of all other paths that do not (see Fig. 2.1). At the same time,

$$G_0(X + Y; T) = P_0, \tag{2.8}$$

because Y and $-Y$ are symmetric to the origin and thus the reflection principle applies. To be more specific, since all paths starting from X and terminating at $-Y$ must pass the origin, and by reversing only the direction of the random walks at the origin, there is a one-to-one correspondence between the paths terminating at $-Y$ and Y, which guarantees that the two sums are equal as they are of the equal probability to move in either direction.

On the semi-infinite cable, if the terminal is open, all paths touching the origin escape from the cable, that is, the sum only consists of paths that do not touch the origin,

$$G_o(X, Y; T) = P_1 = G_0(X - Y) - G_0(X + Y). \tag{2.9}$$

If the terminal is closed, all paths touching the origin are forced to reverse direction, that is, the paths terminating at $-Y$ change their destination symmetrically to Y, which gives,

$$G_c(X, Y; T) = 2P_0 + P_1 = G_0(X - Y) + G_0(X + Y). \tag{2.10}$$

It can be easily checked that the Green's functions (2.9) and (2.10) satisfy the boundary conditions (1.35) and (1.36) respectively.

A branching node

We now consider a branching node χ that connects K semi-infinite cables (forming a set of branches $\mathcal{B}_\chi$). The Green's functions on this branching structure can be constructed by applying the same idea as in the previous case.

Assume that $G_{ij}(X, Y; T)$ is the Green's function for the input at location Y on branch j and the output at location X on branch i for $i, j \in \mathcal{B}_\chi$. The probability p_i that the random walk moves into cable i when it stands at the branching node should sum up to 1 over all i, and turns out to be proportional to the axial conductance, which implies,

$$p_i = \frac{r_i^{3/2}}{\sum_{k \in \mathcal{B}_\chi} r_k^{3/2}}, \tag{2.11}$$

assuming the axial resistivity R_a is the same for all the cables. Following the same arguments as in the previous case, if X, Y locate on the same cable i,

$$G_{ii}(X, Y; T) = 2p_i P_0 + P_1. \tag{2.12}$$

Otherwise, if X, Y locate on different branches, i.e. $i \neq j$,

$$G_{ij}(X, Y; T) = 2p_j P_0. \tag{2.13}$$

Substituting the values of P_0, P_1 thus gives

$$G_{ij}(X, Y; T) = \delta_{ij} G_0(X - Y; T) + (2p_j - \delta_{ij}) G_0(X + Y; T), \tag{2.14}$$

for any $i, j \in \mathcal{B}_\chi$, where δ_{ij} is the Kronecker delta. It is not difficult to check that the Green's function (2.14) satisfies the boundary conditions (1.37) and (1.38).

2.2.2 Random walks on an arbitrary tree

Now consider a passive dendritic tree with branching nodes, terminals and semi-infinite ends in an arbitrary geometry. Recall any Green's function is a probability distribution constructed from random walks,

$$G_{ij}(X, Y; T) = \mathbb{P}(Y \in j | X \in i; T). \tag{2.15}$$

Notably any random walk by our construction has the Markovian property, that is, the movement along the dendritic tree is independent of its past history. Thus, the probability on the right hand side can be split into a sum of probabilities conditional on intermediate states Z,

$$\mathbb{P}(Y \in j | X \in i; T) = \sum_k \int_0^{L_k} \mathbb{P}(Y \in j | Z \in k; T - \epsilon) \mathbb{P}(Z \in k | X \in i; \epsilon) dZ, \quad (2.16)$$

which is a Chapman-Kolmogorov equation, and can be rewritten in terms of Green's functions by Eq. (2.15),

$$G_{ij}(X, Y; T) = \sum_k \int_0^{L_k} G_{ik}(X, Z; \epsilon) G_{kj}(Z, Y; T - \epsilon) dZ, \quad (2.17)$$

for k running over all the dendritic segments, where L_k is the scaled length of branch k. Since $G_{ij}(X, Y; T)$ is an LTI system, the value of ϵ can be chosen arbitrarily and Eq. (2.17) is indeed well defined due to the properties (1.49) and (1.52) of Green's functions. At a particular node on the dendritic tree with the limit $\epsilon \downarrow 0$, the probability that the paths forming $G_{ik}(X, Z; \epsilon)$ do not touch other nodes is 1, and thus virtually no boundary conditions other than those at the node, i.e. Eqs. (1.37) and (1.38), have to be considered.

Therefore, although it is not trivial to contruct Green's functions directly on an arbitrary tree as in the previous cases due to the presence of multiple boundary conditions, it is possible to decomposite any Green's function similarly to Eq. (2.14) locally at individual nodes. The Green's function can eventually be rewritten as an infinite sum over G_0's by such decompositions with coefficients and arguments to be determined. Formalising this idea, Abbott et al. [18] introduced the framework of sum-over-trips. An individual trip is defined to be a highly restricted random path that starts from x and terminates at y but can only change direction at nodes. The electrotonic length of each trip is

$$L_r(x, y) = \mu(l_r(x, y)) = \mu_i(x) + \cdots + \mu_k(l_k) + \cdots + \mu_j(y), \quad (2.18)$$

where l_k is the physical length of segment k,

$$X = \mu_i(x) \quad (2.19)$$

defines a spatial scaling mapping induced by λ_i on each segment i in the same form

as Eq. (2.4), and

$$\mu : x \to X, \tag{2.20}$$

is an ensemble of μ_i for all i. Whenever each trip changes direction at nodes from segment n to m, it picks up a node factor $\alpha_{nm} = p_m$, and the product of all its node factors gives the trip coefficient A_r. Each trip is thus weighted $A_r G_0(L_r(x, y); T)$ and the infinite sum over all trips (forming a set $\mathbb{T}$),

$$G_{ij}(X, Y; T) = \sum_{r \in \mathbb{T}} A_r G_0(L_r(x, y); T), \tag{2.21}$$

gives the Green's function.

The framework is essentially a reformulation of the path integral on a metric graph. A trip is virtually equivalent to a family of random walk paths that share the same boundary conditions. Due to the Markovian property, the total probability is the product of the transition probabilities at the boundaries and the transition probability from x to y on a cable without considering any boundaries. The transition probability at the boundaries lead to A_r, and the random walks on an infinite cable give G_0. The deduction of the sum-over-trips framework and the proof of its equivalence to the path integral formulation are omitted here, as it is much easier to check its rules are valid after presenting them. The detailed rules shown in [18] are also omitted here, since they only work for a passive dendritic tree, and in the next section §2.3, the rules generalised for constructing Green's functions on a resonant dendritic tree will be listed. Moreover, a detailed deduction of the rules of the sum-over-trips framework on tapered dendrites, the most recent generalisation, can be found in §3.3.

2.3 Sum-over-trips on resonant dendrites

Here cylindrical dendrites with resonant membranes are considered, that is, the membrane potential dynamics is described by the resonant cylindrical cable equation (1.28). The equation can be rewritten in terms of the dimensionless spatial variable X introduced in (2.4),

$$\tau_m \frac{\partial V}{\partial t} = -V + \frac{\partial^2 V}{\partial X^2} + \frac{I_0(X; t)/\lambda - I_h}{g_l}, \tag{2.22a}$$

$$L_h \frac{\partial I_h}{\partial t} = -r_h I_h + V, \tag{2.22b}$$

where

$$I_0(X;t) = \frac{I_{\text{inj}}(t)\delta(X-Y)}{2\pi r_c} = \frac{I_{\text{inj}}(t)\lambda\delta(x-y)}{2\pi r_c} = \lambda I_0(x;t) \tag{2.23}$$

due to the property of the Dirac delta function when $\delta(y)$ is transformed into $\delta(Y)$.

Although in theory we can find the Green's function of Eq. (2.22) by the path integral formulation as in §2.2, an alternative approach is taken below for its relative simplicity. Nonetheless, the interpretion by random walks is sometimes employed because it is intuitive and equivalent.

2.3.1 Green's functions on an infinite cable

Consider a resonant cable without any boundary conditions. Instead of solving Eq. (2.22) directly, we take its Laplace transform and aim to solve it in the frequency domain. Explicitly,

$$\left[\gamma^2(\omega) - \frac{\partial^2}{\partial X^2}\right] V = \frac{I_0(X;\omega)/\lambda + U_0(\omega)}{g_l}, \tag{2.24}$$

where

$$\gamma^2(\omega) = \tau_m\omega + 1 + \frac{1}{g_l(r_h + L_h\omega)}, \tag{2.25}$$

and $U_0(\omega)$ defined in (1.59) equals 0 by assuming zero initial conditions. Eq. (2.24) can be then recast into

$$\left[\nabla^2 + (i\gamma(\omega))^2\right] V = -\frac{I_0(X;\omega)}{\lambda g_l}, \tag{2.26}$$

where ∇^2 is the Laplacian on V over $X \in \mathbb{R}$ and i the imaginary unit. Eq. (2.26) is notably in the form of an one-dimensional inhomogeneous Helmholtz equation with a wavenumber $k = i\gamma(\omega) \in \mathbb{C}$. The solution to the following canonical form of the Helmholtz equation,

$$\left[\nabla^2 + k^2\right] G_h(X) = -\delta(X-Y), \tag{2.27}$$

is known to be

$$G_h(X-Y) = \frac{i\exp(ik|X-Y|)}{2k}, \tag{2.28}$$

given no boundary conditions. Thus, the Green's function of Eq. (2.26) on an infinite cable is in particular

$$G_H(X-Y;\omega) = \frac{\exp(-\gamma(\omega)|X-Y|)}{2\gamma(\omega)}. \tag{2.29}$$

Since $I_0(X;\omega)$ contains $\delta(X-Y)$ by definition (2.23),

$$V(X;\omega) = G_H(X-Y;\omega)\frac{I_0(Y;\omega)}{2\pi r_c g_l \lambda}, \tag{2.30}$$

or, equivalently in the original x-coordinate,

$$V(x;\omega) = \frac{r_a \exp(-\lambda^{-1}\gamma(\omega)|x-y|)}{2\lambda^{-1}\gamma(\omega)} I_{\text{inj}}(\omega), \tag{2.31}$$

where the axial resistance r_a is defined in (1.22). By absorbing the characteristic length parameter λ,

$$\gamma_c(\omega) = \frac{\gamma(\omega)}{\lambda} = \sqrt{\frac{1}{D}\left[\omega + \frac{1}{\tau_m} + \frac{1}{C_m(r_h + L_h\omega)}\right]}, \tag{2.32}$$

where

$$D = \tau_m \lambda^2 = \frac{r_c}{2R_a C_m} \tag{2.33}$$

is the diffusion constant, we obtain the transfer impedance (i.e. the transfer function, or the Green's function in the frequency domain),

$$G_\infty(x;\omega|y) = G_\infty(x,y;\omega) = \frac{r_a}{2\gamma_c(\omega)} \exp(-\gamma_c(\omega)|x-y|). \tag{2.34}$$

It also proves useful later to consider $l(x,y) = |x-y|$ as the distance between x and y, $L(x,y) = \mu(l(x,y))$ the electrotonic distance, and $\mathcal{L}(x,y) = \gamma(L(x,y))$ the normalised distance, where $\gamma : X \to \mathcal{X}$ is a spatial normalising mapping defined by

$$\mathcal{X} = \gamma(\omega)X. \tag{2.35}$$

I call $\mathcal{L}(x,y)$ the normalised distance, because the mapping γ normalises Eq. (2.26) into

$$(\nabla^2 + i^2)V(\mathcal{X};\omega) = -I_N(\mathcal{X};\omega), \tag{2.36}$$

where

$$I_N(\mathcal{X};\omega) = \frac{I_0(X;\omega)}{\gamma(\omega)\lambda g_l}, \tag{2.37}$$

and Eq. (2.36) is a normalised Helmholtz equation with a wavenumber $k = i = \sqrt{-1}$. It is however worth noting that, $\mathcal{X}$ is a normalised but complex-valued variable, so the Green's function (2.28) cannot be used directly for Eq. (2.36), because $\mathcal{X} \notin \mathbb{R}$.

Nonetheless, by writing $|X| = X\mathrm{sgn}(X)$ we obtain

$$H_\infty(\mathcal{X}) = \frac{\exp(-\mathcal{X}\mathrm{sgn}(\mathcal{X}/\gamma(\omega)))}{2}, \tag{2.38}$$

as the Green's function of Eq. (2.36). It is then straightforward to check that this result agrees with the Green's function (2.34), which can be rewritten in terms of the normalised distance as

$$G_\infty(x, y; \omega) = \frac{1}{z(\omega)} H_\infty(-\mathcal{L}(x, y)), \tag{2.39}$$

where

$$z(\omega) = \frac{\gamma_c(\omega)}{r_a} \tag{2.40}$$

is the characteristic admittance, i.e. $z^{-1}(\omega)$ is the characteristic impedance. Notably $G_\infty(x, y; \omega)$ in Eqs. (2.34) and (2.39) is different by a factor $2\pi r_c C_m = D r_a$ from that in [19] where the Green's function is convoluted with I_0 instead of I_{inj}. The definition in (2.34) and (2.39) is preferred in this thesis because it separates the information of the input and the system, while in the definition in [19] the strength of I_0 is dependent on the input location.

2.3.2 Green's functions on an arbitrary tree

Now consider a dendritic tree as a metric graph Γ, at whose node χ a boundary condition introduced in §1.2.4 is applied, and on whose branch i the membrane potential dynamics is described by Eqs. (1.28). Explicitly, on branch i of length l_i,

$$\tau_{m,i} \frac{\partial V_i}{\partial t} = -V_i + \frac{\partial^2 V_i}{\partial X^2} + \frac{\delta_{ij} \lambda_j I_{0,j}(X; t) - I_{h,i}}{g_{l,i}}, \tag{2.41a}$$

$$L_{h,i} \frac{\partial I_{h,i}}{\partial t} = -r_{h,i} I_{h,i} + V_i, \tag{2.41b}$$

for $X = x/\lambda_i \in [0, L_i]$, where $L_i = l_i/\lambda_i$, and

$$I_{0,j}(X; t) = \frac{I_{\mathrm{inj}}(t)\delta(X - Y)\delta_{ij}}{2\pi r_c}. \tag{2.42}$$

In other words, the spatial scaling mapping μ scales the metric graph Γ to a new graph $\mu(\Gamma)$ whose edges are now measured in electrotonic length.

The system (2.41) is almost identical to Eqs. (2.22), except for the additional subscripts i, j to denote the dependence of variables on branches and the extra Kronecker delta δ_{ij} as only a single input is assumed on the tree (located on branch

j). We can thus follow the same steps as before, taking the Laplace transform and assuming zero initial conditions, and obtain

$$\left[\frac{\partial^2}{\partial X^2} + (i\gamma_i(\omega))^2\right] V_i = -\frac{I_{0,j}(X;\omega)}{\lambda_j g_{l,i}}, \tag{2.43}$$

where

$$\gamma_i(\omega) = \sqrt{\tau_{m,i}\omega + 1 + \frac{1}{g_{l,i}(r_{h,i} + L_{h,i}\omega)}}. \tag{2.44}$$

An ensemble of $\gamma_i(\omega)$ for all i naturally forms a spatial normalising mapping:

$$\gamma : X \to \mathcal{X}, \tag{2.45}$$

which reduces Eq. (2.43) to

$$(\nabla^2 - 1)V_i(\mathcal{X};\omega) = -I_N(\mathcal{X};\omega), \tag{2.46}$$

where

$$I_N(\mathcal{X};\omega) = \frac{I_{0,j}(X;\omega)}{\gamma_j(\omega)\lambda_j g_{l,i}}. \tag{2.47}$$

$\Gamma_0 = \gamma_c(\Gamma)$ is therefore a quantum graph, where

$$\gamma_c = \gamma \cdot \mu, \tag{2.48}$$

because Γ_0 is a metric graph, and the operator acting on all of its edges is $(\nabla^2 - 1)$ in Eq. (2.46). Therefore, the Green's function of the system (2.46) would have been (2.38), equivalently, the Green's function of the resonant system (2.43) would have been (2.39), if no boundary conditions are presented, which is unusual for a dendritic tree.

Inspired by the Green's function (2.21) by the sum-over-trips framework for the passive dendrites, we take the following ansatz for the resonant dendrites,

$$G_{ij}(x,y;\omega) = \sum_{r\in\mathbb{T}} A_r(\omega) G_\infty(\mathcal{L}_r(x,y);\omega), \tag{2.49}$$

where $A_r(\omega)$ is the trip coefficient, a product of node factors to be discussed in the next section, $\mathcal{L}_r(x,y) = \gamma(L_r(x,y))$ is the normalised trip length. Since the electrotonic length $L_r(x,y) \geq 0$, we can rewrite the Green's function (2.49) by

substituting in (2.38) as

$$G_{ij}(x,y;\omega) = \frac{1}{z_j(\omega)} \sum_{r\in\mathbb{T}} A_r(\omega) H_\infty(\mathcal{L}_r(x,y)), \tag{2.50}$$

where $z_j(\omega)$ is the local characteristic admittance of segment j, generalising from the definition (2.40). In order to obtain the Green's function in the time domain $G(x,y;t)$, the inverse Laplace transform of Eq. (2.50) needs to be taken in the end. Nonetheless, to obtain the solution to the system (2.22), it is more convenient to transform $I_{\text{inj}}(t)$ into the frequency domain to compute

$$V_{ij}(x,y;\omega) = G_{ij}(x,y;\omega) I_{\text{inj}}(\omega), \tag{2.51}$$

and take the inverse Laplace transform to obtain $V(x,y;t)$, rather than performing the convolution (1.51) of $G_{ij}(x,y;t)$ and $I_{\text{inj}}(t)$ in the time domain.

The node factors

A trip picks up a node factor α_{nm} whenever it changes direction at some node from segment n to m. Each node factor encodes the information of the boundary condition(s) at the local node, and contributes to the trip coefficient $A_r(\omega)$ in the Green's function (2.50).

At an open terminal,

$$\alpha_{mm} = -1, \tag{2.52}$$

and, if the terminal is closed,

$$\alpha_{mm} = 1. \tag{2.53}$$

At a branching node,

$$\alpha_{nm} = 2p_m - \delta_{nm}, \tag{2.54}$$

where the transition probability

$$p_m = \frac{z_m(\omega)}{\sum_k z_k(\omega)}. \tag{2.55}$$

The node factor for a somatic node shares the same expression as Eq. (2.54) but

$$p_{S,m} = \frac{z_m(\omega)}{z_S(\omega) + \sum_k z_k(\omega)}, \tag{2.56}$$

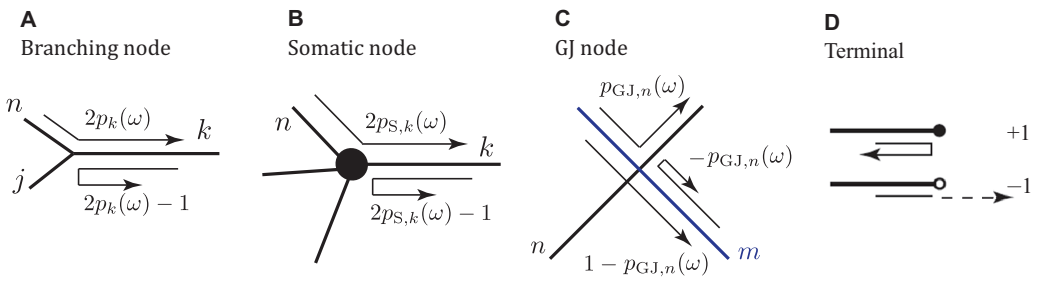

Figure 2.2: The node factors of different types of nodes defined by the sum-over-trips frameworks.

where

$$z_S(\omega) = C_S\omega + \frac{1}{R_S} + \frac{1}{r_S + L_S\omega} \tag{2.57}$$

is the admittance of the somatic membrane, i.e. $z_S^{-1}(\omega)$ is the somatic admittance. At a gap junction,

$$\alpha_{nm} = p_{GJ,m}, \tag{2.58}$$

and

$$\alpha_{mm} = -p_{GJ,n}, \tag{2.59}$$

if the trip reflects at the gap junction, but

$$\alpha_{mm} = 1 - p_{GJ,n}, \tag{2.60}$$

if the trip passes by the gap junction without changing direction, where

$$p_{GJ,m} = \frac{z_m(\omega)}{z_m(\omega) + z_n(\omega) + 2R_{GJ}z_m(\omega)z_n(\omega)}. \tag{2.61}$$

It is now straightforward to check that Eq. (2.50) with node factors defined as above (summarised in Fig. 2.2) is the Green's function of Eq. (2.43) and satisfies all the boundary conditions in §1.2.4. The detailed deductions of the terminal, branching and somatic node factors can be found in [19] and that of the gap-junctional node factors in [20].

2.3.3 General properties of sum-over-trips

Here two nice properties and one major limitation of the sum-over-trips framework are discussed.

Loops in dendrites

A single dendritic tree has no loops but a neuronal network has and is commonly highly recurrent, in particular locally. It is noted firstly in [18] that the sum-over-trips framework can deal with graphs with loops, not only on trees, which is a nice property inherited from the path integral formulation. However, the original framework by [18] was used on passive dendrites of a branching geometry only, while it was shown by [66, 67] that response functions (in the frequency domain) on such dendrites without loops can be found in compact analytical forms (instead of infinite sums by the sum-over-trips framework). Nonetheless, the inclusion of gap junctions into the framework by [20] allows us to find the Green's function on a network of resonant neurons coupled by electrical synapses, where loops can be presented, while the methods by [66, 67] cannot deal with any loops.

The reciprocity principle

We can easily see the reciprocity principle (1.55) from the Green's function (2.34) on a single cable. However, it is not trivial to see that the principle is also valid for the Green's function (2.50) on a dendritic tree. Below I prove this fact.

On an arbitrary dendritic tree, assume the trip coefficient of a particular trip to be,

$$A_r(\omega) = \alpha_{ik_1}\alpha_{k_1k_2}\alpha_{k_2k_3}\dots\alpha_{k_{n-1}k_n}\alpha_{k_nj}. \tag{2.62}$$

The trip coefficient of the reversal trip, denoted by $-r$ can be written as

$$A_{-r}(\omega) = \alpha_{jk_n}\alpha_{k_nk_{n-1}}\alpha_{k_{n-1}k_{n-2}}\dots\alpha_{k_2k_1}\alpha_{k_1i}, \tag{2.63}$$

simply because the reversal trip travels in the opposite direction. The ratio between them is

$$\frac{A_r(\omega)}{A_{-r}(\omega)} = \frac{z_j(\omega)}{z_i(\omega)}, \tag{2.64}$$

because $\alpha_{nm} = \alpha_{mn}$ if $m = n$, and by definition any pair of α_{nm}, α_{mn} share the same denominator and

$$\alpha_{nm} \propto z_m(\omega), \tag{2.65}$$

if $m \neq n$. Since, for any trip from x to y, its reversal trip has exactly the same (normalised) length, i.e. $\mathcal{L}_r(x,y) = \mathcal{L}_{-r}(y,x)$,

$$\frac{\sum A_r(\omega)H_\infty(\mathcal{L}_r(x,y))}{\sum A_{-r}(\omega)H_\infty(\mathcal{L}_{-r}(y,x))} = \frac{z_j(\omega)}{z_i(\omega)}, \tag{2.66}$$

which, by Eq. (2.50), gives

$$G_{ij}(x, y; \omega) = G_{ji}(y, x; \omega), \tag{2.67}$$

and the similar equality holds for the Green's function in the time domain.

It is worth noting that Eq. (2.67) is essentially the reciprocity identity mentioned in [18, 19]. However, since they define the Green's function differently from this thesis (up to the constant scale $2\pi r_c$, as discussed in §2.3.1), there are constant coefficients (dependent on the locations of input and output) in their reciprocity equations.

Convergence of the infinite sum

We naturally expect the convergence of the infinite sum in the Green's function (2.50). However, only in the simplest cases of an infinite cable and a single node connecting semi-infinite cable(s), that is, when none or one boundary condition is presented, finitely many trips are constructed. In all other cases, infinitely many trips can be constructed, because a trip can reflect at two boundaries infinitely many times as long as there are at least two boundary conditions presented. In theory, a mathematical proof for the convergence of infinite sum in the Green's function (2.50) can be found in [69], whereas it only considers passive dendrites. However, for numerical computations there is no existing method to enumerate all trips in order for an arbitrary dendritic tree, and it is in general not a trivial task to rewrite such an infinite sum as a convergent series, except special simple cases.

For example, for a model of a single dendritic branch AB with a finite length l (with A located at $x = 0$ and B at $x = l$), all the trips can be sorted into four classes based on four skeleton trips (see Fig. 2.3), as any other trip with more reflections consists of one skeleton trip and multiple recurrences ($yABy$ or $yBAy$). Since the recurrences $yABy$ and $yBAy$ both gives the same factor $R = \alpha_A \alpha_B H_\infty(2\mathcal{L})$, where α_A and α_B are the node factors for a trip reflecting at the two ends, the Green's function in this case can be found as

$$G(x, y; \omega) = \frac{1}{z(\omega)} \sum_{n=0}^{\infty} R^n \sum_{i=1}^{4} C_i, \tag{2.68}$$

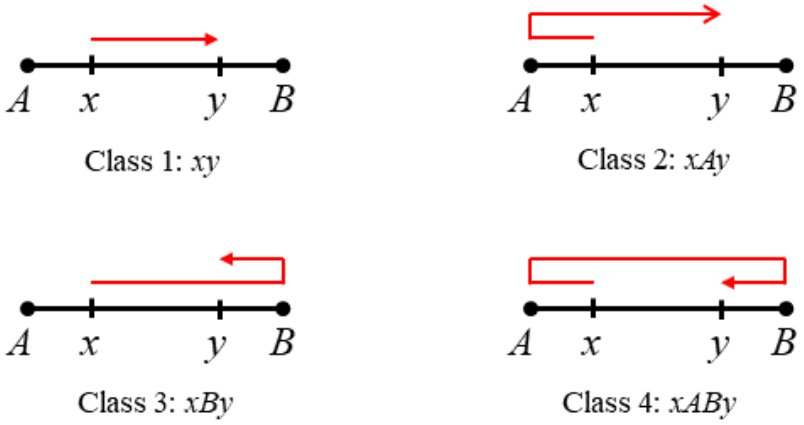

Figure 2.3: The four classes of trips on a single finite dendritic branch. Class 1: xy, the most direct trip not touching two ends. Class 2: xAy, the trips reflecting at one end without passing y. Class 3: xBy, the trip passing y and then reflecting at the other end. Class 4: the trip reflecting at both ends $xABy$.

where, assuming $\mathcal{X}, \mathcal{Y}$ the normalised coordinates of x, y and $x \leq y$,

$$C_1 = H_\infty(\mathcal{Y} - \mathcal{X}), \tag{2.69a}$$

$$C_2 = \alpha_A H_\infty(\mathcal{X} + \mathcal{Y}), \tag{2.69b}$$

$$C_3 = \alpha_B H_\infty(2\mathcal{L} - \mathcal{X} - \mathcal{Y}), \tag{2.69c}$$

$$C_4 = \alpha_A \alpha_B H_\infty(2\mathcal{L} + \mathcal{X} - \mathcal{Y}), \tag{2.69d}$$

are the factors contributed by the four skeleton trips. Since Eq. (2.68) is a geometric series, it can be reduced to an algebraic form that does not contain infinite sums. A model with two finite segments yields such compact solutions as well. Timofeeva et al. [20] considered an example in which the two finite segments are connected by a gap junction and the system is solved by introducing the method of "words". This method names each trip with a word consisting of letters that corresponds to its successive movements. It then identifies four shortest words which play the same roles as the four skeleton trips in the previous case (see Fig. 2.3), and proves that any other trips can be constructed by inserting fixed letter pairs into the shortest words. The compact solution is found by combinatorics and appears to be a geometric series again.

However, these methods cannot be generalised to an arbitrary tree. In practice, numerical computations can only sum up finite terms, and therefore truncations and approximations are necessary in computing the Green's function (2.50). Cao and

Abbott [71] offered an algorithm based on finding the shortest trip, and Caudron et al. [70] proposed a method with four main trips, plus local recurrences. The four main trips are essentially constructed with the same idea as in Fig. 2.3, and the algorithm is named as the four-classes algorithm. Caudron et al. [70] further introduced the length-priority algorithm and compares its convergent errors with the errors when employing the four-classes algorithm on different dendritic morphologies (see Fig. 2.4). Other approaches, e.g. the Monte-Carlo method, are also investigated in the paper, and a more comprehensive study of these numerical methods can be found in [72]. It is clear from Fig. 2.4 that the numerical approximations converge better on the binary tree, a simple geometry, while the computational convergences are considerably worse on realistic dendritic trees. These algorithms are thus inefficient and ineffective for computation, comparing to existing simulation environments, e.g. NEURON [68].

2.4 Method of local point matching

In this section, I will derive the method of local point matching, which allows us to rewrite the Green's function (2.50) in a closed algebraic form for any dendritic geometry. The method and its derivation are based on the sum-over-trips framework. In theory, the derivation of the method serves as a constructive proof for the convergence of the infinite sum in the Green's function (2.50). In practice, since there are no more infinite sums to be considered, numerical results can be computed with high efficiency and accuracy.

2.4.1 Derivation of the method

Firstly, the following function is introduced,

$$J_{ij}(x, y; \omega) = 2z_j(\omega)G_{ij}(x, y; \omega), \tag{2.70}$$

which can be rewritten as

$$J_{ij}(x, y; \omega) = \sum_{r \in \mathbb{T}} A_r(\omega) f(L_r(x, y)), \tag{2.71}$$

by Eq. (2.50), where

$$f(L_r(x, y)) = 2H_\infty(\mathcal{L}_r(x, y)). \tag{2.72}$$

Assume the point y is not located at the endpoints v, w of the segment j, explicitly, $v_j = 0 < y < l_j = w_j$. Since all trips terminating at y must have passed v or

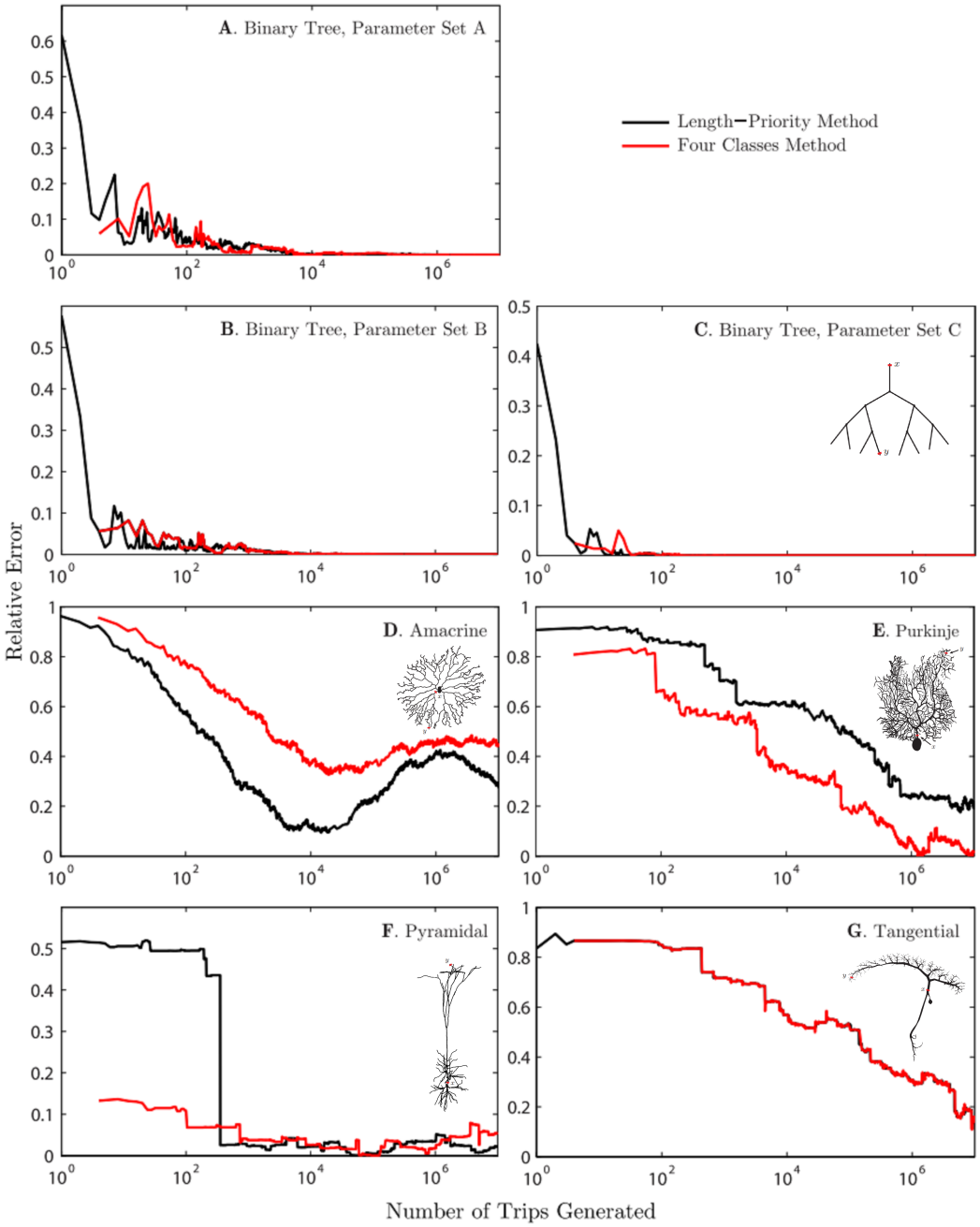

Figure 2.4: Convergence of the four-classes (red) and the length-priority (black) algorithms on different dendritic morphologies, shown by the relative error as a function of the number of trips generated according to the two algorithms. The relative error is the difference between the accurate solutions and the approximations, normalised by the values of the accurate solutions. The accurate solutions are computed in NEURON with high precision. The approximations are computated by the Green's functions found by the four-classes and the length-priority algorithms. Copied from [70].

w for the last time changing directions (at a node), the infinite sum of trips in Eq. (2.71) can be partitioned into two mutually exclusive groups, i.e. $\mathbb{T}_v \cap \mathbb{T}_w = \emptyset$ and $\mathbb{T}_v \cup \mathbb{T}_w = \mathbb{T}$,

$$J_{ij}(x, y; \omega) = \sum_{r \in \mathbb{T}_v} A_r(\omega) f(L_r(x, y)) + \sum_{r \in \mathbb{T}_w} A_r(\omega) f(L_r(x, y)), \tag{2.73}$$

where $\mathbb{T}_v$ (or $\mathbb{T}_w$) is the set of all trips whose final change of directions are at v (or w). Since a trip cannot change directions at any points except nodes,

$$f(L_r(x, y)) = f(\mu_j(d(v_j, y)))f(L_r(x, v_j)), \qquad \text{for } r \in \mathbb{T}_v, \tag{2.74a}$$
$$f(L_r(x, y)) = f(\mu_j(d(w_j, y)))f(L_r(x, w_j)), \qquad \text{for } r \in \mathbb{T}_w, \tag{2.74b}$$

which can be substituted into Eq. (2.73), and gives

$$J_{ij}(x, y; \omega) = f(\mu_j(d(v_j, y)))J_{ij}(x, v_j; \omega) + f(\mu_j(d(w_j, y)))J_{ij}(x, w_j; \omega), \tag{2.75}$$

where

$$J_{ij}(x, v_j; \omega) = \sum_{r \in \mathbb{T}_v} A_r(\omega) f(L_r(x, v_j)), \tag{2.76a}$$
$$J_{ij}(x, w_j; \omega) = \sum_{r \in \mathbb{T}_w} A_r(\omega) f(L_r(x, w_j)). \tag{2.76b}$$

It is worth noting that the definitions (2.76) are consistent with the form of (2.71), by assuming, without loss of generality, that all trips terminating at v_j explicitly means that they terminate at node v and change the direction to segment j, including the trips coming from segment j. One should be warned that the trips terminating at v (without specifying the segment) instead of v_j are considered ill-defined; I will discuss the cases when the input y is located at a node in §2.4.1, which is confusing but different.

Now by simplifying the notations as $J_{ij}(x, y; \omega) = J_y$, $J_{ij}(x, v_j; \omega) = J_{v_j}$ and $J_{ij}(x, w_j; \omega) = J_{w_j}$, Eq. (2.75) can be rewritten as

$$J_y = f(Y)J_{v_j} + f(L_j - Y)J_{w_j}, \tag{2.77}$$

as $\mu_j(v_j) = 0$ and $\mu_j(w_j) = L_j$. If the point y is located on a semi-infinite branch and w_j is the end at infinity, then $|L_j - Y| \to +\infty$, implying $f(L_j - Y)J_{w_j} = 0$, and thus in this case

$$J_y = f(Y)J_{v_j}. \tag{2.78}$$

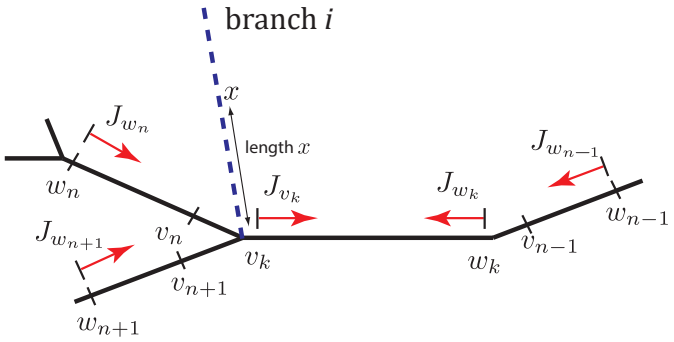

Figure 2.5: Part of a network with the placed pairs of points (v_k, w_k) and the corresponding functions J_{v_k} and J_{w_k}.

Following similar steps, any J_{v_n} (or J_{w_n}) can be rewritten in terms of J_{v_n} (and/or J_{w_n}) from all the branches connected to node v (or w). For example, consider a set of branches $\mathcal{B}_v$ are connected at node v as in Fig. 2.5, J_{v_k} for $k \in \mathcal{B}_v$ can be found as

$$\begin{aligned} J_{v_k} &= \sum_{n\in\mathcal{B}_v} \sum_{r\in\mathbb{T}_{w_n}} A_{w_n}(\omega) f(L_r(x, w_n)) \alpha_{nk} f(L_n) \\ &= \sum_{n\in\mathcal{B}_v} \alpha_{nk} f(L_n) \sum_{r\in\mathbb{T}_{w_n}} A_{w_n}(\omega) f(L_r(x, w_n)) \\ &= \sum_{n\in\mathcal{B}_v} \alpha_{nk} f(L_n) J_{w_n}, \end{aligned} \tag{2.79}$$

where $L_n = \mu_n(l_n)$ is the electrotonic length of segment n. However, if $x \in [0, l_i]$ is located on branch $i \in \mathcal{B}_v$, an additional term representing a direct trip from the starting point x to v_k needs to be added,

$$J_{v_k} = \sum_{n\in\mathcal{B}_v} \alpha_{nk} f(L_n) J_{w_n} + \alpha_{ik} f(X). \tag{2.80}$$

Therefore, combining Eqs. (2.79) and (2.80) gives

$$J_{v_k} = \sum_{n\in\mathcal{B}_v} \alpha_{nk} f(L_n) J_{w_n} + \delta_{ik}\alpha_{ik} f(X). \tag{2.81}$$

Since each J_{v_k} can be written in terms of one another by Eq. (2.81), an ensemble of all J_{v_k} naturally forms a system of linear equations, where J_{v_k} are the unknown variables. For a fixed dendritic tree the number of these unknowns is equal to the degree sum of the corresponding quantum graph Γ_0. It is possible to show that the system of equations is linearly independent and therefore has a unique solution. By

solving the linear system, J_{v_j} and J_{w_j} can be found and $J_y = J_{ij}(x, y; \omega)$ can be obtained by Eq. (2.77). If both x and y are located on the same segment, the direct trip from x to y is added because Eq. (2.77) only considers trips from the two ends of the segment, that is,

$$J_y = f(Y)J_{v_j} + f(L_j - Y)J_{w_j} + f(|X - Y|). \tag{2.82}$$

The Green's function $G_{ij}(x, y; \omega)$ can then be calculated from Eq. (2.70) as

$$G_{ij}(x, y; \omega) = \frac{1}{2z_j(\omega)} J_y. \tag{2.83}$$

Note that the coefficient in front of J_y is different from that in Yihe and Timofeeva [73] where the method is firstly published, because the original definition of the Green's function (2.34) is modified as explained in §2.3.1.

Input located at a node

In practice, experimentalists can inject current into a node, e.g. a soma. In the path integral formulation, locating the input at a node is well defined, because a random walk path starting from (or terminating at) a point infinitesimally close to a node is virtually equivalent to the path starting from (or terminating at) that node, since the transition probability between the two points is asymptotically 1. However, it is assumed in the above derivation of the local point matching method that the input y is not located at any nodes, as it causes ambiguity in the choice of the last node factor. Nonetheless, since the Green's function $G_{ij}(x, y; \omega)$ on an arbitrary dendritic tree is continuous in x due to the boundary conditions considered in §1.2.4, the reciprocity principle (2.67) guarantees its continuity in y. Thus, for an input located at a node χ, the sum-over-trips framework and the local point matching method can be used as if $y = \chi_k$ for any fixed branch $k \in \mathcal{B}_\chi$, where $\mathcal{B}_\chi$ is the set of branches attached to χ. In other words, we always consider the input is virtually located on a segment, and the assumption made in the above derivation causes no loss of generality.

2.4.2 Summary of the algorithm

Here the main steps of the algorithm of the local point matching method are summarised:

1. Compute the spatial normalising mapping γ_c defined in (2.48) that normalises Γ into a quantum graph Γ_0 whose segments are measured in normalised length

$\mathcal{L}_k(\omega)$;

2. Compute node factors α_{nm} by Eqs. (2.52) to (2.61) (summarised in Fig. 2.2) at all the nodes;

3. Construct the linear system of J_v and J_w by Eq. (2.81) based on the local connectivity, using $\mathcal{L}_k(\omega)$ and α_{nm};

4. Solve the constructed linear system by matrix inversion and multiplication;

5. Compute
$$J_y = f(Y)J_{v_j} + f(L_j - Y)J_{w_j} + \delta_{ij}f(|X - Y|). \tag{2.84}$$
If the input is located at a node, fix y on an arbitrary branch attached to the node.

6. Compute the Green's function $G_{ij}(x, y; \omega)$ by Eq. (2.83), and obtain $G_{ij}(x, y; t)$ by the inverse Fourier transform (equivalent to the inverse Laplace transform).

2.4.3 Results on toy examples

Applications of the local point matching method are investigated below on toy models of neuronal systems. More numerical results on concrete models are to be discussed in **Chapter 4**.

A "ball-and-stick" model

A "ball-and-stick" model of a single neuron consists of a lumped soma and a single cylindrical dendritic branch attached to it. The model is probably the simplest neuronal model with the presence of dendrites. Assume that the soma is located at $x = 0$, and that the branch attached to it is of length l_0 with a closed terminal (see Fig. 2.6).

The membrane potential dynamics of the system is described by Eqs. (2.41) for $x \in [0, l_0]$, and is subject to the boundary conditions (1.39) at $x = 0$ and (1.36) at $x = l_0$. To solve this system analytically in the frequency domain, we take the Laplace transform and assume zero initial condition, the equations become
$$\left[\gamma^2(\omega) - \lambda^2 \frac{\partial^2}{\partial x^2}\right] V(x; t) = \frac{I_0(x; \omega)}{g_l}, \tag{2.85}$$
where $\gamma(\omega)$ and λ are defined in (2.44) and (1.31) respectively, and
$$I_0(x; \omega) = \frac{I_{\text{inj}}(\omega)\delta(x - y)}{2\pi r_c}. \tag{2.86}$$

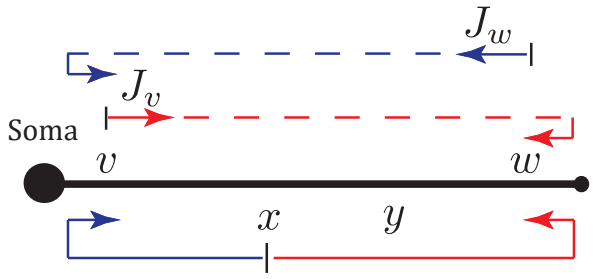

Figure 2.6: A schematic of a neuron with a soma and a single dendrite. The terms of Eq. (2.92a) are shown by blue arrows, and those of Eq. (2.92b) are shown by red arrows.

At the same time, the boundary conditions become

$$z_S(\omega)V(0;\omega) = \frac{1}{r_a}\frac{\partial V(x;\omega)}{\partial x}\bigg|_{x=0}, \tag{2.87a}$$

$$0 = \frac{\partial V(x;\omega)}{\partial x}\bigg|_{x=l_0}, \tag{2.87b}$$

where $z_S(\omega)$ and r_a are defined in (2.57) and (1.22) respectively.

To obtain the Green's function of Eq. (2.85) satisfying the boundary conditions (2.87), we could apply the sum-over-trips framework directly. Since there is only one segment in the model, the method of four classes (see Fig. 2.3) can be used, which gives the Green's function (2.68), explicitly,

$$G(x,y;\omega) = \frac{1}{z(\omega)}\sum_{n=0}^{\infty} R^n \sum_{i=1}^{4} C_i, \tag{2.88}$$

where

$$C_1 = \frac{1}{2}\exp(\gamma_c(\omega)|x-y|), \tag{2.89a}$$

$$C_2 = (2p_{S,c}-1)\frac{1}{2}\exp(\gamma_c(\omega)(x+y)), \tag{2.89b}$$

$$C_3 = \frac{1}{2}\exp(\gamma_c(\omega)(2l_0-x-y)), \tag{2.89c}$$

$$C_4 = (2p_{S,c}-1)\frac{1}{2}\exp(\gamma_c(\omega)(2l_0+x-y)), \tag{2.89d}$$

are the factors contributed by the four skeleton trips, and

$$R = (2p_{S,c}-1)\frac{1}{2}\exp(\gamma_c(\omega)l_0) \tag{2.90}$$

is the factor of reccurence. Notably $(2p_{S,c}-1)$ is the reflective somatic node factor, where

$$p_{S,c} = \frac{z(\omega)}{z_S(\omega)+z(\omega)} \tag{2.91}$$

according to the definition (2.56), and the reflective terminal node factor is $+1$. One can check the Green's function (2.88) is only different by a factor $2\pi r_c$ from that derived in [74] for the reasons discussed in §2.3.1.

Alternatively, we can use the local point matching method to construct the following system of J_v and J_w (see the arrows in Fig. 2.6),

$$J_v = \left[\frac{1}{2}\exp(\gamma_c(\omega)l_0)J_w + \frac{1}{2}\exp(\gamma_c(\omega)x)\right](2p_{\mathrm{S},c}-1), \tag{2.92a}$$

$$J_w = \frac{1}{2}\exp(\gamma_c(\omega)l_0)J_v + \frac{1}{2}\exp(\gamma_c(\omega)(l_0-x)). \tag{2.92b}$$

Solving the system results in

$$J_v = \frac{(2p_{S,c}-1)[\exp(\gamma_c(\omega)(2l_0-x))+\exp(\gamma_c(\omega)x)]/2}{1-(2p_{S,c}-1)\exp(2\gamma_c(\omega)l_0)/2}, \tag{2.93a}$$

$$J_w = \frac{[(2p_{S,c}-1)\exp(\gamma_c(\omega)(l_0+x))+\exp(\gamma_c(\omega)(l_0-x))]/2}{1-(2p_{S,c}-1)\exp(2\gamma_c(\omega)l_0)/2}, \tag{2.93b}$$

which gives

$$G(x,y;\omega) = \frac{1}{2z(\omega)}[\exp(\gamma_c(\omega)y)J_v+\exp(\gamma_c(\omega)(l_0-y))J_w+\exp(\gamma_c(\omega)|x-y|)] \tag{2.94}$$

by Eqs. (2.83) and (2.84). It can be shown that the Green's functions (2.88) and (2.94) obtained by the two methods are identical, as Eq. (2.88) is a geometric series.

Consider the somatic responses only, the somatic Green's function in this "ball-and-stick" model can be found as

$$G(0,y;\omega) = \frac{1}{z(\omega)\tanh\gamma_c(\omega)l_0 + z_S(\omega)}\frac{\cosh\gamma_c(\omega)(l_0-y)}{\cosh\gamma_c(\omega)l_0}, \tag{2.95}$$

from Eq. (2.94). The special case of somatic input $G(0,0;\omega)$ is plotted in Fig. 2.7. It is clear from the Bode magnitude plot Fig. 2.7b that the model behaves as a band-pass filter with a resonant frequency around 1 kHz. Variations in membrane potentials of a relatively high frequency are likely to be smoothed out. This mechanism is economic in neural information transmission, because high frequency signals are often caused by noises, and even when they encode information, the higher the frequency is, the smaller the amount of information can be transmitted [75].

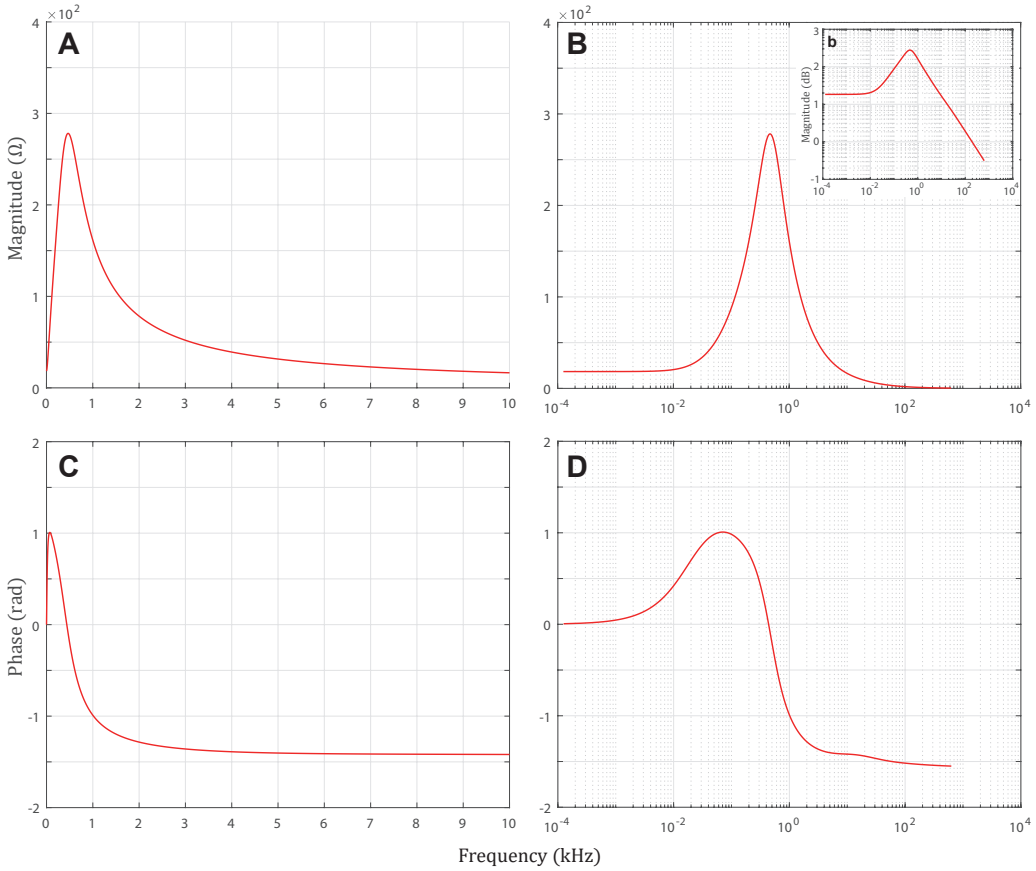

Figure 2.7: The somatic input impedances in the "ball-and-stick" model. (**A,B,b**): The magnitudes of the the impedances. The unit of the vertical axis in (**b**) is decibel (dB), which is by definition logarithmic in the magnitudes. (**C,D**): The phases of the impedances. The impedance functions (2.95) are complex, because the imaginary frequencies in the Laplace domain (i.e. the real frequencies in the Fourier domain) are employed. (**b**) and (**D**) together are commonly known as the Bode plots in control theory. Geometric parameters: $r_c = 1$ µm, $r_S = 12.5$ µm and $l_0 = 100$ µm. Electrical parameters: $C_m = C_{\text{soma}} = 1$ µF·cm^{-2}, $R_m = R_{\text{soma}} = 2000$ Ω·cm^2, $R_a = 100$ Ω·cm, $r_h = r_{\text{soma}} = 1000$ Ω·cm^2 and $L_h = L_{\text{soma}} = 5$ H·cm^2.

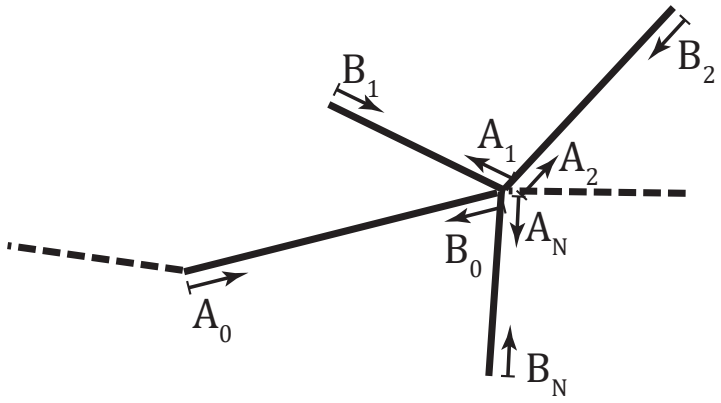

Figure 2.8: A schematic of a branching node in an arbitrary dendritic tree. The node connects N terminal segments, index from 1 to N, and segment 0 that eventually links this branching node to the soma (on the left).

Conditions for equivalent cylinders

An electrotonic equivalent cylinder is a virtual dendritic branch transformed from (a part of) a dendritic tree, so that the solutions obtained for the equivalent cylinder are directly applicable to this dendritic tree [17]. In many situations (e.g. [76]), the branching geometry of dendrites can be replaced by such equivalent cylinders, and the computational study of such models can be largely simplified; ideally, an entire dendritic tree can be equivalent to the "ball-and-stick" model discussed above (e.g. [17, 54]).

Here I consider a local branching geometry of $N+1$ dendritic branches (see Fig. 2.8). The branches are indexed here by $i \in \{0, 1, 2, \ldots, N\}$, and branch i is of length l_i. Except branch 0 connected to other parts of the dendritic tree, all other branches have closed terminals. Below I aim to find the conditions for the equivalent cylinder for these branches $i \in \{1, 2, \ldots, N\}$.

Using the method of local point matching on the dendritic tree, we construct on segment $i \in \{1, 2, 3, \ldots, N\}$ that

$$a_i = b_i f_i (2p_i - 1) + \sum_{j=1}^{N} b_j f_j 2p_i + a_0 f_0 2p_i, \qquad \text{for } j \neq i, \tag{2.96a}$$

$$b_i = a_i f_i, \tag{2.96b}$$

which gives

$$a_i = \frac{2p_i}{1+f_i^2}\left[a_0 f_0 + \sum_{j=1}^{N} a_j f_j^2\right], \tag{2.97}$$

where $f_i = \exp(\gamma_{c,i}(\omega) l_i)/2$ and $a_i = J_{A_i}, b_i = J_{B_i}$ being the local trips towards the terminals and the soma, respectively. By introducing new variables,

$$A = \sum_{j=1}^{N} a_j f_j^2, \tag{2.98}$$

$$B = \sum_{i=1}^{N} \frac{2p_i f_i^2}{1+f_i^2}, \tag{2.99}$$

Eq. (2.97) becomes

$$A = \frac{a_0 f_0 B}{1-B}, \tag{2.100}$$

and thus,

$$b_0 = a_0 f_0 (2p_0 - 1) + \sum b_i f_i 2p_0 = a_0 f_0 \left[\frac{2p_0}{1-B} - 1\right], \tag{2.101}$$

where

$$p_0 = \frac{z_0(\omega)}{z_0(\omega) + \sum_{i=1}^{N} z_i(\omega)}. \tag{2.102}$$

Assume the output x is not located on the local segments under investigation, and that the equivalent cylinder keeps the Green's function invariant when all the branches $i \in \{1, 2, 3, \ldots, N\}$ are replaced by it. Following the same steps,

$$b_0^* = a_0^* f_0 \left[\frac{2p_0^*}{1-B^*} - 1\right], \tag{2.103}$$

where

$$p_0^* = \frac{z_0(\omega)}{z_0(\omega) + z_1^*(\omega)}, \tag{2.104}$$

$$B^* = \frac{2p_1^* f_1^{*2}}{1+f_1^{*2}}, \tag{2.105}$$

and all the variables in the equivalent model are denoted by the superscript $*$.

In order to guarantee the equivalence, it is necessary and sufficient to show a_0, b_0 are unchanged given the replacement, because the geometry of the other parts of the dendritic tree is arbitrary but fixed, that is,

$$\frac{p_0^*}{1-B^*} = \frac{p_0}{1-B}. \tag{2.106}$$

Comparing Eqs. (2.99) to (2.105) and (2.102) to (2.104), the conditions for the equivalence are $f_i = f_1^*, B = B^*$, which gives

$$\gamma_{c,1}^*(\omega) l_1^* = \gamma_{c,i}(\omega) l_i, \qquad \text{for } i \in \{1, 2, 3, \ldots, N\}, \tag{2.107}$$

$$z_1^*(\omega) = \sum_{i=1}^{N} z_i(\omega). \tag{2.108}$$

It is straightforward to see now that if the input y is not located on any segment $i \in \{1, 2, 3, \ldots, N\}$, the Green's functions of the original branching model and the equivalent cylindrical model are indifferent. If the input is located on segment $i \in \{1, 2, 3, \ldots, N\}$, with a distance of y away from the branching node,

$$J_y = a_i f(\gamma_{c,i}(\omega) y) + b_i f(\gamma_{c,i}(\omega)(l_i - y)). \tag{2.109}$$

By Eqs. (2.96b) and (2.97), J_y can be rewritten as

$$J_y = \frac{2p_i}{1 + f_i^2} \left[a_0 f_0 + \sum_{j=1}^{N} a_j f_j^2 \right] [f(\gamma_{c,i}(\omega) y) + f(\gamma_{c,i}(\omega)(2l_i - y))]. \tag{2.110}$$

Similarly, for the equivalent cylinder,

$$J_y^* = \frac{2p_1^*}{1 + f_1^{*2}} \left[a_0 f_0 + a_1^* f_1^{*2} \right] [f(\gamma_{c,1}^*(\omega) y) + f(\gamma_{c,1}^*(\omega)(2l_1^* - y))]. \tag{2.111}$$

It can be checked that, if $\gamma_{c,1}^*(\omega) = \gamma_{c,i}(\omega)$ is additionally assumed,

$$\frac{J_y}{J_y^*} = \frac{z_i(\omega)}{z_i^*(\omega)}, \tag{2.112}$$

which leads to identical Green's functions in the two cases due to Eq. (2.83). Furthermore, due to the reciprocity identity (2.67), the equivalent cylinder works for any pair of input and output locations.

It is worth noting that the conditions are exactly the famous 3/2 branching rule. Eq. (2.107) requires identical electrotonic lengths, while Eq. (2.108) can be rewritten as

$$r_1^{*3/2} = \sum_{i=1}^{n} r_i^{3/2}, \tag{2.113}$$

where r_i is the radius of the segment i in the original model and r_1^* is the radius of the equivalent cylinder, if all the electrical parameters are identical in the two models.

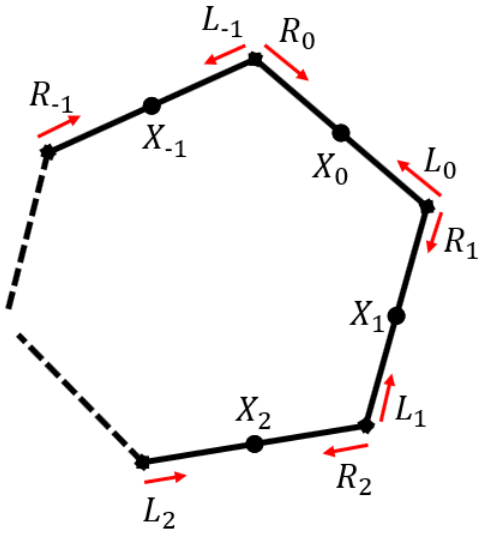

Figure 2.9: A schematic of a ring of N neurons. Positive indices are used clockwise, and negative indices are counter-clockwise. The arrows denote the terms in Eqs. (2.114) constructed by the local point matching method.

A ring of electrically coupled neurons

Here a simplified model of a ring of neurons is considered. All N neurons are assumed to be identical: they are cylindrical in geometry (of electrotonic length L) with middle points indexed by $X_n, n \in \{0, 1, 2, \ldots, N-1\}$ (as we are mostly concerned about the membrane potentials at these locations), and the characteristic admittance is constantly $z(\omega)$; in addition, each of them is connected to adajcent neurons by identical gap junctions at both ends (see Fig. 2.9). This simplified model is studied here, because no previous methods except numerical simulations can find its solution, while the local point matching method can find the analytical solution in the frequency domain. Moreover, it is known that jellyfishes have so-called "nerve rings" as their central nervous systems; a nerve ring is literally a circular bundle of nerve cells, and they are coupled by gap junctions [77, 78].

By the method of local point matching, we can construct the following system (see arrows in Fig. 2.9):

$$R_n = L_n \alpha_r f(2L) + R_{n-1} \alpha_t f(2L) + X_n \alpha_r f(L) + X_{n-1} \alpha_t f(L), \tag{2.114a}$$

$$L_n = R_n \alpha_r f(2L) + L_{n+1} \alpha_t f(2L) + X_n \alpha_r f(L) + X_{n+1} \alpha_t f(L), \tag{2.114b}$$

where R_n, L_n (playing the same roles as J_v, J_w in previous sections) denote clockwise and counter-clockwise local trips respectively on neuron n, and α_t, α_r are the node

factors for reflecting and passing through respectively at a gap junction. Notably only one output needs to be considered, and without loss of generality we assume $X_0 = 1, X_{n\neq 0} = 0$. To save notations, we can write

$$\widetilde{X}_n = \frac{X_n}{f(L)}, \tag{2.115a}$$

$$\widetilde{R}_n = R_n + \widetilde{X}_n, \tag{2.115b}$$

$$\widetilde{L}_n = L_n + \widetilde{X}_n, \tag{2.115c}$$

$$q_\cdot = \alpha_\cdot f(2L), \tag{2.115d}$$

which simplifies the system (2.114) into

$$\widetilde{R}_n - \widetilde{X}_n = q_r \widetilde{L}_n + q_t \widetilde{R}_{n-1}, \tag{2.116a}$$

$$\widetilde{L}_n - \widetilde{X}_n = q_r \widetilde{R}_n + q_t \widetilde{L}_{n+1}. \tag{2.116b}$$

Since $\widetilde{R}_n, \widetilde{L}_n$ in the system (2.116) are defined recursively, we obtain

$$\widetilde{R}_{n+1} - q_r \widetilde{L}_{n+1} = q_t \widetilde{R}_n + \widetilde{X}_{n+1}, \tag{2.117a}$$

$$-q_t \widetilde{L}_{n+1} = q_r \widetilde{R}_n - \widetilde{L}_n + \widetilde{X}_n, \tag{2.117b}$$

which can be recast into the following matrix form:

$$\mathbf{Q_1 J}_{n+1} = \mathbf{Q_0 J}_n + \mathbf{C}_n, \tag{2.118}$$

where

$$\mathbf{J}_n = \begin{bmatrix} \widetilde{R}_n \\ \widetilde{L}_n \end{bmatrix}, \tag{2.119a}$$

$$\mathbf{Q_0} = \begin{bmatrix} q_t & 0 \\ q_r & -1 \end{bmatrix}, \qquad \mathbf{Q_1} = \begin{bmatrix} 1 & -q_r \\ 0 & -q_t \end{bmatrix}, \tag{2.119b}$$

$$\mathbf{C}_n = \begin{bmatrix} \widetilde{X}_{n+1} \\ \widetilde{X}_n \end{bmatrix}. \tag{2.119c}$$

We can now recall the assumption $X_0 = 1, X_{n\neq 0} = 0$. It simply gives

$$\mathbf{C}_0 = \begin{bmatrix} 0 \\ \widetilde{X}_0 \end{bmatrix}, \qquad \mathbf{C}_{-1} = \begin{bmatrix} \widetilde{X}_0 \\ 0 \end{bmatrix}, \qquad \mathbf{C}_{n\notin\{0,-1\}} = \begin{bmatrix} 0 \\ 0 \end{bmatrix}. \tag{2.120}$$

Notably here negative index are used to denote neurons in a counter-clockwise order;

on this ring, $n = N - m$ if and only if $-m, n$ denote the same neuron. Therefore, Eq. (2.118) can be rewritten as

$$\mathbf{J}_0 = \mathbf{B}\mathbf{J}_{-1} + \mathbf{Q_1}^{-1}\mathbf{C}_{-1}, \tag{2.121a}$$

$$\mathbf{J}_1 = \mathbf{B}\mathbf{J}_0 + \mathbf{Q_1}^{-1}\mathbf{C}_0, \tag{2.121b}$$

$$\mathbf{J}_n = \mathbf{B}\mathbf{J}_{n-1}, \qquad \text{for } n \geq 2, \tag{2.121c}$$

where $\mathbf{Q_1}^{-1}$ is the inverse matrix of $\mathbf{Q_1}$, and

$$\mathbf{B} = \mathbf{Q_1}^{-1}\mathbf{Q_0}. \tag{2.122}$$

For $m, n \in \{2, 3, 4, \ldots, N-1\}$, Eq. (2.121c) implies

$$\mathbf{J}_{-m} = \mathbf{B}^{1-m}\mathbf{J}_{-1}, \tag{2.123a}$$

$$\mathbf{J}_n = \mathbf{B}^{n-1}\mathbf{J}_1. \tag{2.123b}$$

We can now apply the cyclic boundary condition,

$$\mathbf{J}_n = \mathbf{J}_{-m}, \tag{2.124}$$

for $n = N - m$. Without loss of generality, consider $m, n \in \{2, 3, 4, \ldots, N-1\}$, substituting Eqs. (2.123a) into (2.124) gives

$$\mathbf{B}^{n-1}\mathbf{J}_1 = \mathbf{B}^{1-m}\mathbf{J}_{-1}, \tag{2.125}$$

and further substituting Eqs. (2.121a) and (2.121b) results in

$$\mathbf{J}_{-1} = -(\mathbf{I_2} + (\mathbf{B}^N - \mathbf{I_2})^{-1}(\mathbf{B}^{-1}\mathbf{Q_1}^{-1}\mathbf{C}_{-1} + \mathbf{B}^{-2}\mathbf{Q_1}^{-1}\mathbf{C}_0), \tag{2.126}$$

where $\mathbf{I_2}$ is the identity matrix of rank 2. All $\mathbf{J}_n$ can thus be found by Eq. (2.118) in closed analytical forms, and the system (2.114) is solved. $G(x, y; \omega)$ to any input location y for x the middle points of each neuron can then be obtained.

An infinite array of neurons

Here we consider a model of an infinite array of neurons (see Fig. 2.10). To be specific, the model is considered to be identical in all aspects as the previous nerve ring model, except that there is an infinite number of neurons and no neuronal loop. In fact, it is possible to treat this case as a ring of infinite number of cells, that is, we may use directly the results from the previous example with $N \to +\infty$.

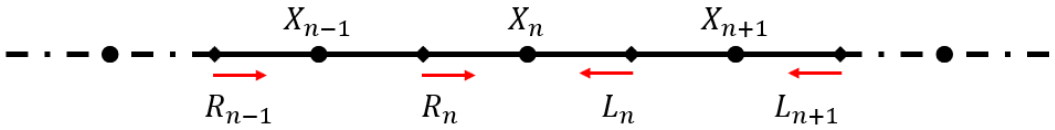

Figure 2.10: A schematic of an infinite array of neurons. The arrows denote the terms in Eqs. (2.114) constructed by the local point matching method. The equations are identical to those in the previous example, but the boundary condition here is given by the spatial symmetry (2.128), instead of cyclic boundaries.

If we solve this model directly by the local point matching method (following the arrows in Fig. 2.10), we construct the system (2.114) and its matrix representation (2.118). Now instead of the cyclic boundary condition (2.124), we note the the spatial symmetry about X_0, which gives

$$\widetilde{R}_1 = \widetilde{L}_{-1}, \tag{2.127a}$$

$$\widetilde{L}_1 = \widetilde{R}_{-1}, \tag{2.127b}$$

or equivalently

$$\mathbf{J}_{-1} = \mathbf{R_2}\mathbf{J}_1, \tag{2.128}$$

where

$$\mathbf{R_2} = \begin{bmatrix} 0 & 1 \\ 1 & 0 \end{bmatrix}. \tag{2.129}$$

Combining Eqs. (2.121a), (2.121b) and (2.128), we obtain

$$\mathbf{J}_1 = (\mathbf{I_2} - \mathbf{B}^2\mathbf{R_2})^{-1}(\mathbf{B}{\mathbf{Q_1}}^{-1}\mathbf{C}_{-1} + {\mathbf{Q_1}}^{-1}\mathbf{C}_0). \tag{2.130}$$

All $\mathbf{J}_n, n \in \mathbb{Z}$ can thus be found by Eq. (2.118) in closed analytical forms, and the system (2.114) is solved. $G(x, y; \omega)$ to any input location y for x the middle points of each neuron can then be obtained.

On top of the linear membrane dynamics, if we assume the middle point of each neuron is a hot spot that can be excited when the membrane potential reaches some threshold, we obtain a Spike-Diffuse-Spike (SDS) model. Such models consider dendritic spines as active points equipped with the IF properties, and distributed in a discrete and uniform density along a dendritic branch [79–82]. With the solution of $G(x, y; \omega)$, the voltage at the hot spot (spine) in each neuron can be checked simultaneously for firing; if some neuron fires, a spike can be considered as a new input added back into the system at this hot spot. Such procedure is computation-

ally cheaper than brutal-force simulation, especially when a relatively long duration of the model is studied and many spikes are possibly generated. Since the Fire-Diffuse-Fire (FDF) models for intra-cellular calcium releases and waves [83–85] are similar to the SDS models in their mathematical expressions, the results can be also employed for the FDF models. For example, Harris and Timofeeva [85] found the analytical Green's function on such a model directly by the sum-over-trips framework, but since it has an infinite sum, approximation of the Green's function by truncation are used in their further numerical investigation.

2.5 Summary

In this chapter, I have reviewed the methods to obtain Green's functions on cylindrical neuronal dendrites from passive to resonant membranes and from single cables to dendritic geometries [18, 19], and derived the new method of local point matching, which allows us to find analytically the Green's functions in closed algebraic forms.

In §2.2, the path integral formulation is employed to find the Green's function on a dendritic cable and a dendritic tree with passive membranes, which leads to the original development of the sum-over-trips framework. The framework is essentially a special application of the path integral formulation on metric graphs, by showing that the weight of a single trip is the sum of the weights of a family of paths, for the trip and the paths that share the same boundary conditions. The sum-over-trips framework is then extended in §2.3, so that it becomes able to deal with resonant dendrites and more types of boundary conditions (offered by different nodes). By modelling the dendritic geometry as a metric graph and reducing all differential equations describing membrane potential dynamics to the normalised Helmholtz equation (2.36), our dendritic model is reduced to a quantum graph. The sum-over-trips framework is shown to be applicable on such quantum graphs. Its properties and one main limitation in numerical computation due to poor convergence of infnite sums are discussed.

In §2.4, a novel method named local point matching is developed based on the sum-over-trips framework. The method overcomes the limitation of the framework, as it results in solutions in closed algebraic form, instead of infinite sums by the framework. Thus, numerical computation by the local point matching method can be both accurate and efficient. Several toy examples are investigated to exhibit the potential applications of the method.

Chapter 3

Sum-Over-Trips on Tapered Dendrites

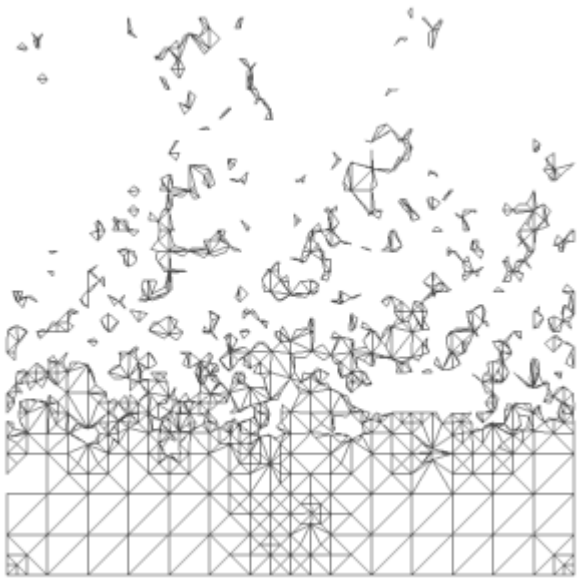

3.1 Introduction

In the previous chapter, the sum-over-trips framework on cylindrical dendrites are studied. However, cylinders are idealised geometries, as the radius of a real dendritic branch could vary along its length (see Fig. 3.1 for an example). Dendritic tapers may be different for various types of neurons, or at different locations of a single cell. Additionally, considering constant change of dendritic geometries and imperfect reconstructions by neuron tracing, a conclusion on how real dendrites taper or which theoretic type of taper is the best model has yet not been drawn. Nonetheless, such phenomena are mostly noticeable in the distal segments where the dendritic branches taper and terminate. Real dendrites are typically reported to exhibit initial rapid decay in radius [55, 86–88]. Thus, in theoretical works, tapered structures that described by exponential decays [88, 89] and by power laws [39, 90] are the most favoured models, because they lead to realistic shapes and have simple mathematical expressions, whereas many works [39, 88, 89] employ multi-compartment models with cylinders of radii decreasing successively by a common factor as numerical approximations. Models with (piece-wise) linear taper are also commonly used [89, 91, 92], which is in principle a special case of power laws, but usually treated as a different type.

Mathematical modelling of the membrane potential dynamics on a tapered dendrite dates back at least to Rall [17]. Poznanski [93] later followed up the theoretical

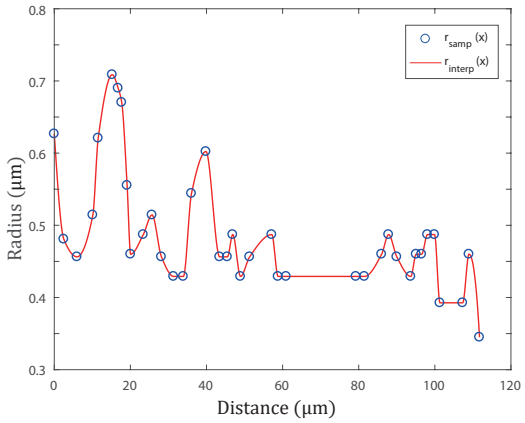

Figure 3.1: An example of the non-trivial continuously varying radius of one terminal dendritic branch (of index 34) in the reconstructed rat pyramidal cell as in Fig. 1.4. The blue circles are the dendritic radius from the reconstructed sample data, and the solid red curve is interpolation of them (by the MATLAB function `interp1` with the method of `pchip`).

investigation into the tapered cable equation derived in [17], and identified all the constraints on the dendritic tapers under which the tapered cable equation is analytically solvable (reviewed in §3.2). The two works can only deal with tapered dendrites that can be reduced to an equivalent tapered cable; in particular, they can only deal with the special case of cylindrical dendrites by an equivalent cylinder. As the previous chapter has shown that the sum-over-trips framework can be employed for general cylindrical dendrites, this chapter will show the framework can also be employed to tapered dendrites, under the same constraints identified by [93] for single tapered cables (see §3.3). In addition, I will also discuss dendrites with more general types of taper (in §3.4), and show the theoretical potential of the sum-over-trips framework to be further extended to be applicable in these cases, whereas it seems to be more practical to employ the finite element method by discretising tapered dendrites into small cylindrical compartments.

3.2 Cable equations on tapered cables

Here we consider a single resonant dendritic cable whose radius $r(x)$ is continuously varying in location x. Its membrane potential dynamics is modelled by the resonant tapered cable equation (1.26). Since the charateristic length parameter

$$\lambda(x) = \left[\frac{1}{2R_a g_l}\frac{r^2(x)}{\rho(x)}\right]^{1/2}, \tag{3.1}$$

is now a variable in x [17, 93, 94], rather than the constant defined in (1.31) for cylindrical dendrites, the bijective mapping μ is defined by

$$X = \mu(x) = \int_0^x \frac{1}{\lambda(y)} dy, \tag{3.2}$$

to scale the physical length x into the electrotonic length X. Notably this mapping μ is reduced to (2.4) if constant radius is considered. Applying μ to the system (1.26) leads to the following equations,

$$\tau_m \frac{\partial V}{\partial t} = \frac{\partial^2 V}{\partial X^2} - V + \frac{d\ln F}{dX}\frac{\partial V}{\partial X} + \frac{I_0(\mu^{-1}(X);t) - \widehat{I}_h}{g_l}, \tag{3.3a}$$

$$L_h \frac{\partial \widehat{I}_h}{\partial t} = -r_h \widehat{I}_h + V, \tag{3.3b}$$

where the constant time parameter τ_m is defined in (5.4), $\mu^{-1} : X \to x$ is the inverse map of μ, $\widehat{I}_h(X;t) = I_h(x;t)$, and

$$F(X) = F(\mu(x)) = F_0 \frac{r^2(x)}{\lambda(x)} \tag{3.4}$$

is defined to be the geometric ratio [93]. It is worth noting that $F(X)$ is a dimensionless variable and the constant scaling F_0 in it has unit in length; however, the value of F_0 can be arbitrarily chosen. Here I consider $F_0 = [F(0)]^{-1}$, which implies $F(0) = 1$, for its simplicity.

3.2.1 Green's functions on a reducible taper

In this section I will show, for several special types of geometric ratio $F(x)$, the system (3.3) can be transformed into the frequency domain and reduced to a normalised Helmholtz equation; a dendritic branch with this property is called a "reducible taper" in this thesis.

By introducing a new variable $V^*(X;t)$ that satisfies

$$V(X;t) = V^*(X;t)\phi(X), \tag{3.5}$$

where

$$\phi(X) = \left[\frac{F(0)}{F(X)}\right]^{\frac{1}{2}}, \tag{3.6}$$

the system (3.3) can be rewritten as

$$\tau_m \frac{\partial V^*}{\partial t} = \frac{\partial^2 V^*}{\partial X^2} - \beta(X)V^* + \frac{I_0(\mu^{-1}(X);t) - \widehat{I}_h}{g_l \phi(X)}, \tag{3.7a}$$

$$L_h \frac{\partial \widehat{I}_h}{\partial t} = -r_h \widehat{I}_h + V^*(X;t)\phi(X), \tag{3.7b}$$

where

$$\beta(X) = 1 + \frac{\xi^2(X)}{4} + \frac{1}{2}\frac{d\xi}{dX}, \tag{3.8}$$

$$\xi(X) = \frac{d \ln F}{dX} = \frac{1}{F}\frac{dF}{dX}. \tag{3.9}$$

Applying the Laplace transform and assuming zero initial conditions, the system (3.7) becomes

$$\left[\gamma^2(X;\omega) - \frac{\partial^2}{\partial X^2}\right] V^*(X;\omega) = \frac{I_0(\mu^{-1}(X);\omega)}{g_l \phi(X)}, \tag{3.10}$$

Table 3.1: Six geometric types that permit analytic solutions for a tapered dendrite. κ, L are positive constants. $F_0 = 1$. Modified from [93].

Type of taper	$F(X)$	Domain of X	$\beta(X)$
Exponential	$\exp(-2\kappa X)$	$0 \leq X$	$1+\kappa^2$
Hyperbolic sine	$\frac{\sinh^2 \kappa(X-L)}{\sinh^2 \kappa L}$	$0 \leq X \leq L$	$1+\kappa^2$
Hyperbolic cosine	$\frac{\cosh^2 \kappa(X-L)}{\cosh^2 \kappa L}$	$0 \leq X \leq L$	$1+\kappa^2$
Sinusoidal	$\frac{\cos^2 \kappa(X-L)}{\cos^2 \kappa L}$	$0 \leq X \leq \frac{\pi}{2\kappa} + L$	$1-\kappa^2$
Trigonometric	$\cos^2 \kappa X$	$0 \leq X \leq \frac{\pi}{2\kappa}$	$1-\kappa^2$
Quadratic	$(1-X/L)^2$	$0 \leq X \leq L$	1

where

$$\gamma^2(X;\omega) = \tau_m \omega + \beta(X) + \frac{1}{(r_h + L_h\omega)g_l}. \tag{3.11}$$

It is worth noting that $\gamma(X;\omega)$ defined here is essentially an extension from that in (2.25), and it is easy to check that $\beta(X) = 1$ in the case of cylindrical dendrites.

If $\gamma(X;\omega)$ is a constant in X, Eq. (3.10) can be reduced to the same form as Eq. (2.26). This constraint implies that $\beta(X)$ is a constant independent of X, and reduces Eq. (3.8) to a Riccati equation, solution of which with respect to the geometric ratio $F(X)$ provides six types of tapered structures [93]. These six types are listed in Table 3.1 and permit analytical solutions to Eq. (3.10). In Fig. 3.2 these six tapered structures $F(X)$ and their original shapes $r(x)$ are plotted. It can be checked by substituting the six types of $F(X)$ into Eq. (3.8) that $\beta(X)$ is indeed constant for each of the six types.

Constraining a tapered structure to be in these six cases, we can introduce again the spatial normalising mapping (2.35), which reduces Eq. (3.10) to

$$(\nabla^2 + i^2)V^*(\mathcal{X};\omega) = -I_N(\mathcal{X};\omega), \tag{3.12}$$

where

$$I_N(\mathcal{X};\omega) = \frac{I_0(\mu^{-1}(\mathcal{X}/\gamma(\omega));\omega)}{g_l\gamma^2(\omega)\phi(\mathcal{X}/\gamma(\omega))}. \tag{3.13}$$

Eq. (3.12) is notably a normalised Helmholtz equation, and shares the same form with Eq. (2.36). Since the Green's function of Eq. (2.36) is $H_\infty(\mathcal{X})$ defined in

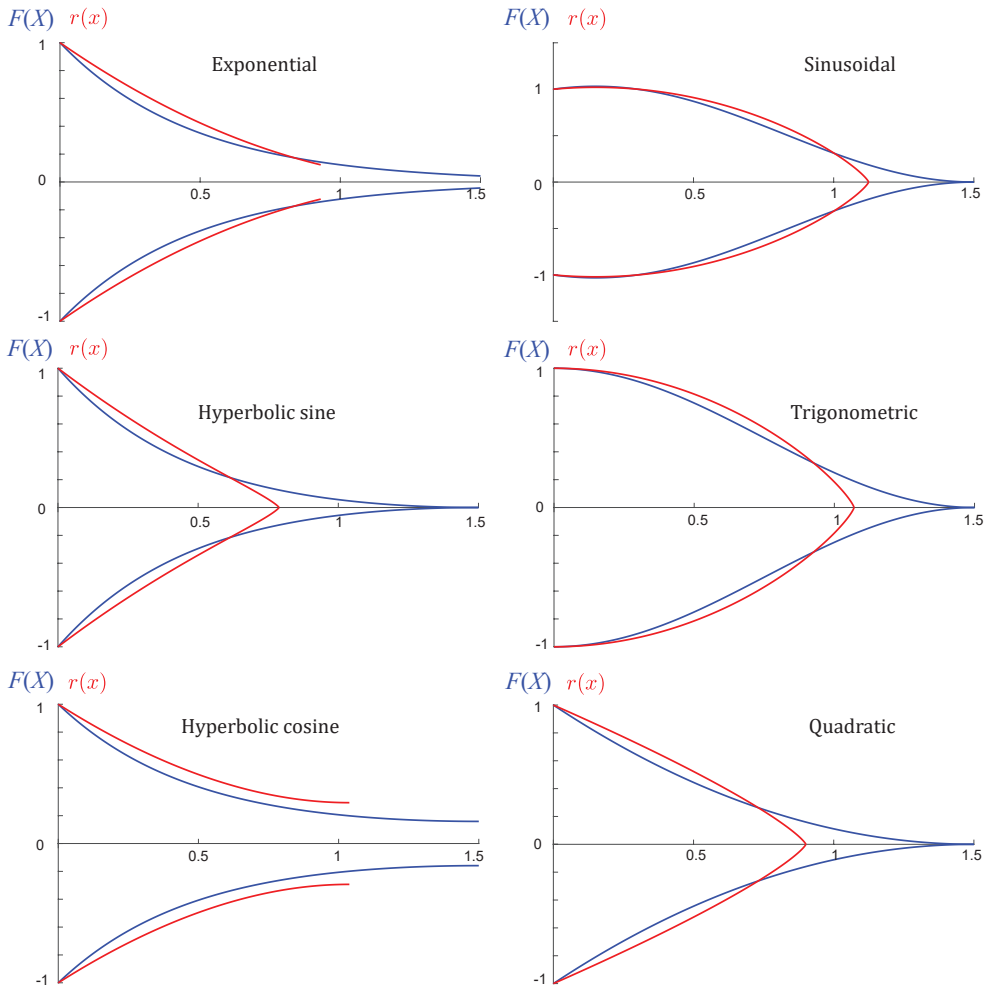

Figure 3.2: Blue curves are tapered cables in the coordinate of $F(X)$ derived from Table 3.1 with parameters (taken the same as in [93]): $\alpha = 1.5$ and $\kappa = \pi/3$, except for the sinusoidal cable where $\alpha = 0.15$ and $\kappa = \pi/2.7$. Red curves are the same cables but in the coordinate of $r(x)$. Note that all functions in this figure are rescaled so that their starting values equal 1.

(2.38), the general solution to Eq. (3.12) is

$$V^*(\mathcal{X};\omega) = \int_{-\infty}^{\infty} H_\infty(\mathcal{X}-\mathcal{Z}) I_N(\mathcal{Z};\omega) d\mathcal{Z}. \tag{3.14}$$

Thus, in the (x,ω,V)-coordinate,

$$V(x;\omega) = \frac{\Phi(y,x)}{z(y;\omega)} H_\infty\left(\gamma(\omega)\int_y^x \frac{1}{\lambda(y)}dy\right) I_{\text{inj}}(\omega), \tag{3.15}$$

where

$$\Phi(y,x) = \frac{\phi(\mu(x))}{\phi(\mu(y))}, \tag{3.16}$$

$$z(y;\omega) = \frac{\gamma(\omega)}{\lambda(y) r_a(y)}, \tag{3.17}$$

$$r_a(x) = \frac{R_a}{\pi r^2(x)}. \tag{3.18}$$

If $I_{\text{inj}}(t) = \delta(t)$, Eq. (3.15) results in the Green's function,

$$G_\infty(x,y;\omega) = \frac{\Phi(y,x)}{2z(y;\omega)} \exp\left(-\gamma(\omega)\left|\int_y^x \frac{1}{\lambda(y)}dy\right|\right), \tag{3.19}$$

which notably reduces to Eq. (2.34) in the cylindrical case.

To obtain the Green's function in time domain, the inverse Laplace transform should be applied. In the special case of a passive system, i.e. in the limit $r_h \to +\infty$, the Green's function can be written explicitly as,

$$G_\infty(x,y;t) = \frac{\Phi(y,x)\lambda(y) r_a(y)}{\sqrt{4\pi\tau_m t}} \exp\left(-\beta(\mu(x))\frac{t}{\tau_m} - \frac{\tau_m}{4t}\left[\int_y^x \frac{1}{\lambda(y)}dy\right]^2\right). \tag{3.20}$$

The Green's function on a single dendritic cable of the Exponential type of taper is plotted in Fig. 3.3 and compared with the heat kernel with leakage on a cylindrical cable (the Green's function of the classical standard cable equation). It is clear that the dendritic taper breaks the spatial symmetry.

Simplified relation between radius and geometric ratio

Although the six types of taper permit analytical solutions for Eq. (3.10), the constraints are for the geometric ratio $F(X)$, whereas we prefer the knowledge of the dendritic shape described by $r(x)$. Given $r(x)$, it is straightforward to find $F(X)$ by Eqs. (3.1), (3.2) and (3.4). However, it is generally only possible to compute $r(x)$

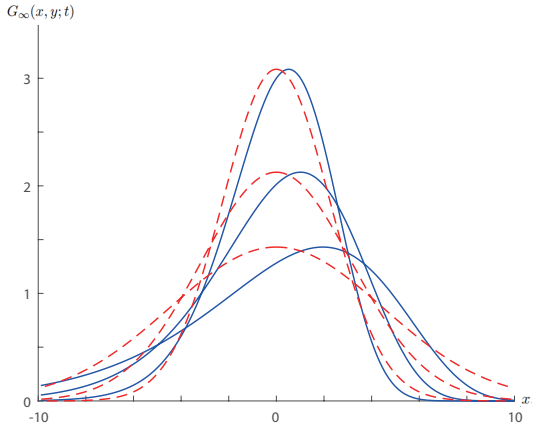

Figure 3.3: The heat kernels on a cylindrical (red) dendritic cable of an infinite length and a tapered (blue) one. The tapered dendrite is of the Exponential type with $\kappa = \pi/3$. The Dirac-delta input is placed at $x = 0$ where $r(x) = 1$. The radius of the cylindrical dendrite is $r_c = 1$. For schematic purpose, $2R_a g_l = 1, R_a = 4\pi^{3/2}, \tau_m = 4$ are assumed in Eq. (3.20) and the voltage distributions are plotted for $t = 0.1, 0.2, 0.4$ successively. All parameters are in arbitrary units here.

from $F(X)$ by numerical methods, because $r(x)$ is implicitly defined by $F(X)$, and these six types are not exceptions. Nonetheless, as the change of dendritic radius is considered to be small in most situations including these six types, it is reasonable to assume $[r'(x)]^2 \ll 1$. Eq. (3.1) thus reduces to

$$\lambda(x) = \lambda_* [r(x)]^{1/2}, \tag{3.21}$$

where

$$\lambda_* = \left[\frac{R_m}{2R_a}\right]^{1/2}. \tag{3.22}$$

As a result, Eq. (3.4) gives

$$F(X) = F_0 \frac{\lambda^3(x)}{\lambda_*^4}, \tag{3.23}$$

which leads to

$$x = \mu^{-1}(X) \approx \lambda_*^{3/4} \int_0^X \left[\frac{F(Y)}{F_0}\right]^{1/3} dY, \tag{3.24}$$

$$r(x) \approx \left[\lambda_* \frac{F(X)}{F_0}\right]^{2/3}. \tag{3.25}$$

It is clear that Eq. (3.25) gives a simplified bijective mapping between $r(x)$ and $F(X)$, if constants F_0 and λ_* are known.

3.2.2 Green's functions on a realistic taper

Although solving the resonant tapered cable equation (1.26) by transforming it into (3.3) does not rely on the assumption $[r'(x)]^2 \ll 1$, it is employed in the previous section so that it is easier to find $r(x)$ from $F(X)$. Here a stronger assumption is made that $[r'(x)]^2 \ll 1$ can be directly applied to Eq. (1.26), which gives

$$C_m \frac{\partial V}{\partial t} = -g_l V - I_h + \frac{1}{2R_a r(x)} \frac{\partial}{\partial x} \left[r^2(x) \frac{\partial V}{\partial x} \right] + I_0(x;t), \tag{3.26a}$$

$$L_h \frac{\partial I_h}{\partial t} = -r_h I_h + V. \tag{3.26b}$$

This assumption is implicitly accepted in [90, 95] where they directly started to study the passive tapered cable equation (1.27) assuming $\rho(x) = r(x)$. This assumption is justified by the observation that the variation of dendritic radius is significantly smaller than the change of membrane potentials [96]. By the Laplace tranform and assuming zero initial conditions, Eq. (3.26) is reduced to

$$\mathcal{E}(\omega) V = \frac{1}{2R_a r(x)} \frac{\partial}{\partial x} \left[r^2(x) \frac{\partial V}{\partial x} \right] + I_0(\omega), \tag{3.27}$$

where $\mathcal{E}(\omega)$ can be found in (1.58). Instead of finding the analytical solutions as in §3.2.1, below I directly investigate the system by assuming $r(x)$ follows the realistic descriptions of dendritic taper, in particular for $r(x)$ following an exponential decay and a power law.

Dendritic tapers described by exponential decays

Consider that the radius of a tapered dendritic branch is described by the following exponential decay,

$$r(x) = r_0 e^{ax}, \tag{3.28}$$

where $a < 0$ is a constant. Note this exponential taper in $r(x)$ is different from the Exponential type $F(X)$ in §3.2.1. The charateristic length parameter is thus

$$\lambda(x) = \lambda_0 e^{ax/2}, \tag{3.29}$$

which gives

$$X = -\frac{2}{\lambda_0 a}\left(e^{-ax/2} - 1\right), \tag{3.30}$$

$$\phi(X) = \left(1 - \frac{\lambda_0 a}{2} X\right)^{3/2}. \tag{3.31}$$

Eq. (3.27) can then be rewritten as

$$\left[R_m \mathcal{E}(\omega) + \frac{15}{4}\left(X - \frac{2}{\lambda_0 a}\right)^{-2} - \frac{\partial^2}{\partial X^2}\right] V^* = \frac{I_0}{g_l \phi}, \tag{3.32}$$

where $V^* = V/\phi$ follows the relationship (3.5). It is clear to see that, Eq. (3.32) cannot be reduced to the normalised Helmholtz equation (2.36). Nonetheless, by a constant translation $2\lambda_0 a$ of X, Eq. (3.32) can be recast into

$$\left[R_m \mathcal{E}(\omega) + \frac{C_0}{X^2} - \frac{\partial^2}{\partial X^2}\right] V^* = \frac{I_0}{g_l \phi}, \tag{3.33}$$

where

$$C_0 = \frac{15}{4}. \tag{3.34}$$

When $I_{\text{inj}}(t) = \delta(t)$, its Laplace transform $I_{\text{inj}}(\omega) = 1$, and solving Eq. (3.33) for V^* results in its Green's function $G^*(X;\omega)$, that is,

$$\left[R_m \mathcal{E} + \frac{C_0}{X^2} - \frac{\partial^2}{\partial X^2}\right] G^* = \frac{\tau_m}{D\lambda r_a \phi}\delta(X - Y), \tag{3.35}$$

where the variable D here is genearalised to be dependent on x by replacing r_c with $r(x)$ in (2.33). Since the variables on the right hand side is completely determined by Y, it is possible to define a length constant γ_y by

$$\gamma_y^2 = \frac{\tau_m}{D\lambda r_a \phi}, \tag{3.36}$$

and to scale X by $\bar{x} = \gamma_y X$. In addition, by introducing $G^{**} = G^*/\gamma_y$, Eq. (3.35) reduces to

$$HG^{**} = \delta(\bar{x} - \bar{y}). \tag{3.37}$$

where

$$H = \frac{R_m \mathcal{E}}{\gamma_y^2} + \frac{C_0}{\bar{x}^2} - \frac{\partial^2}{\partial \bar{x}^2} \tag{3.38}$$

is the linear operator acting on G^{**}. Assume H admits a set of eigenfunctions $g_n(\bar{x})$ which is complete, that is,

$$\sum_{n=0}^{\infty} g_n^{\dagger}(\bar{x}) g_n(\bar{y}) = \delta(\bar{x} - \bar{y}), \tag{3.39}$$

where $g_n^{\dagger}(\bar{x})$ is the complex conjugate of $g_n(\bar{x})$ and μ_n is the corresponding eigenvalue. The Green's function can be constructed as

$$G^{**}(\bar{x}, \bar{y}; \omega) = \sum_{n=0}^{\infty} \frac{g_n^{\dagger}(\bar{x}; \omega) g_n(\bar{y}; \omega)}{\mu_n(\omega)}. \tag{3.40}$$

The eigenfunctions and eigenvalues of H can be found by solving

$$HG^{**} = \mu G^{**}. \tag{3.41}$$

Introducing the new dependent variable K via $G^{**} = \bar{x}^{1/2} K$, Eq. (3.41) can be recast into the canonical form of the Bessel differential equation as

$$\tilde{x}^2 K_{\tilde{x}\tilde{x}} + \tilde{x} K_{\tilde{x}} + (\tilde{x}^2 - \alpha_0^2) K = 0, \tag{3.42}$$

where

$$\tilde{x} = \bar{x} \left[\mu - \frac{R_m \mathcal{E}}{\gamma_y^2} \right]^{1/2}, \tag{3.43}$$

$$\alpha_0 = 2. \tag{3.44}$$

The analytical solutions can be presented by Bessel functions. Since Bessel functions of the first kind with α_0 and $-\alpha_0$ are linearly dependent to each other when α_0 is an integer, Bessel functions of the second kind are additionally needed in this case. Transforming everything back, we obtain the Green's function of Eq. (3.27) in terms of Bessel functions in the case of exponential tapers.

Dendritic tapers described by power laws

Consider that the radius of a tapered dendritic branch can be described by the following power law,

$$r(x) = r_0 \left[\frac{l - x}{l} \right]^{\nu} = r_0 (1 + ax)^{\nu}, \tag{3.45}$$

where $\nu \geq 0$ and $a = -l^{-1} < 0$ are arbitrary constants. Note that $\nu = 0$ recovers the cylindrical cases, and thus $\nu \neq 0$ is assumed in this section.

With the simplified $\lambda(x)$ defined by Eq. (3.21), the mapping μ leads to

$$X = \int_0^x \frac{1}{\lambda_0}(1 + ay)^{-\nu/2} dy, \tag{3.46}$$

where

$$\lambda_0 = \lambda_* r_0^{1/2}. \tag{3.47}$$

If $\nu = 2$,

$$X = \mu(x) = \frac{1}{\lambda_0 a} \ln(1 + ax). \tag{3.48}$$

The geometric ratio can then be found as

$$F(X) = \frac{r_0^{3/2}}{\lambda_*} \exp\left(\frac{3}{2} a \lambda_0 X\right). \tag{3.49}$$

It is worth noting that, by writing

$$\kappa = -\frac{3}{2} a \lambda_0, \tag{3.50}$$

in Eq. (3.49), the Exponential type of taper in §3.2.1 is recovered. In other words, under the assumption $[r'(x)]^2 \ll 1$, the parabolic taper (i.e. dendritic taper following the power law with the power $\nu = 2$) is equivalent to the Exponential type. Goldstein and Rall [97] also showed the equivalence under the same assumption, whereas the proof was conducted in an opposite way, assuming the geometric ratio to be the Exponential type in the beginning. The parabolic taper can thus be well approximated by the Exponential type (3.49), or *vice versa*. Fig. 3.4 shows the Exponential type (transformed back to the original coordinate) versus the parabolic taper, and their differences in the nested plot. The horizontal and vertical axes are notably not presented in the same scale (otherwise the slope of the curve cannot be seen clearly due to $[r'(x)]^2 \ll 1$), but they do share the same unit. Nonetheless, their difference (i.e. the approximation error) is clearly tiny.

In fact, the two Hyperbolic types can also numerically fit the parabolic taper quite well. Nonetheless, the Exponential type is characterised by only the parameter κ, while the two Hyperbolic types need the additional parameter L, which set an upper limit for X (see Table 3.1), and this constraint is enforced by mathematical deductions, rather than biological reality. To remove this mathematical constraint, assume $L \to +\infty$, and the geometric ratios of the two Hyperbolic types can be

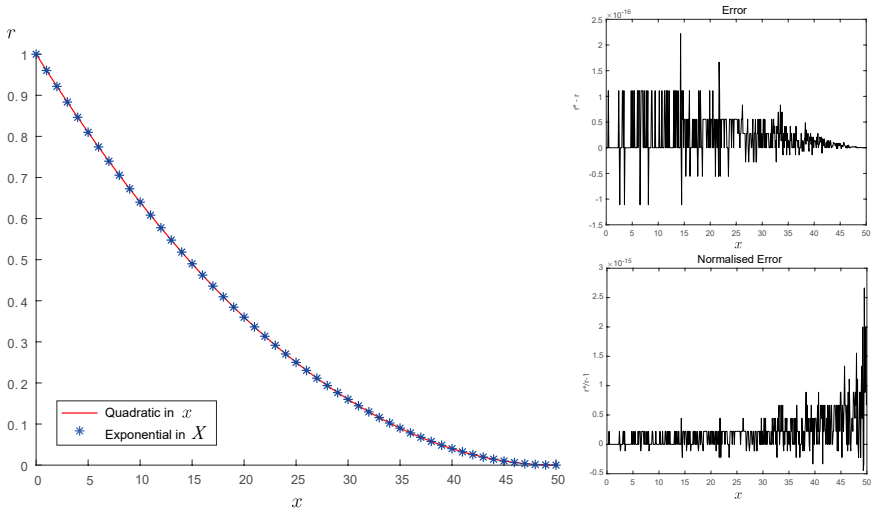

Figure 3.4: Comparison of the original model of parabolic taper defined by Eq. (3.45) for $\nu = 2$ in red and the approximation of the Exponential type defined by Eq. (3.49) in blue asterisks, transformed back from $F(X)$ to $r(x)$ by (3.25), where $l = 50, r_0 = 1, \lambda_0 = 1$.

written in one expression as

$$F(X) = \left[\frac{e^{-\kappa X} \pm e^{\kappa(X-2L)}}{e^{-2\kappa L} \pm 1}\right]^2, \tag{3.51}$$

where $+$ is for the Hyperbolic cosine type and $-$ for the Hyperbolic sine type. The denominator inside the brackets reduces to ± 1 because $\kappa L \to +\infty$, and by the same limit

$$F(X) = \left[e^{-\kappa X}\left(1 \pm e^{-2\kappa(L-X)}\right)\right]^2 = e^{-2\kappa X}, \tag{3.52}$$

which has essentially the same form as the Exponential type. If the parabolic taper has a terminal radius of 0, the mapping μ defined by Eq. (3.48) transforms $x = l$ to $X = +\infty$. It is reasonable to assume $L \to +\infty$ for a tapered dendrite with a tiny terminal radius. Nonetheless, in practice, the dendritic length $l_0 \leq l$ and the terminal radius $r_1 = r(l_0)$ can be predetermined by a neuronal model. For any $l_0 < l$, the mapping μ transforms $x = l_0$ to some finite value $X = L_0$. Thus, it is also easy to set an upper limit of the scaled dendritic length for the Exponential type, and this limit L_0 is meaningful in the biological sense.

If $\nu \neq 2$, the integral (3.46) results in

$$X = \frac{1}{\lambda_0 a(1-\nu/2)} \left[(1+ax)^{1-\nu/2} - 1\right]. \tag{3.53}$$

In addition, $\phi(X)$ defined by Eq. (3.6) can be found explicitly as

$$\phi(X) = \left[\lambda_0 a \left(1 - \frac{\nu}{2}\right) X + 1\right]^{-\frac{3\nu}{4(1-\nu/2)}}. \tag{3.54}$$

Introducing a new spatial variable,

$$\zeta = \frac{(1+ax)^{1-\nu/2}}{a(1-\nu/2)}, \tag{3.55}$$

Eqs. (3.53) and (3.54) can be rewritten as

$$X = \frac{1}{\lambda_0}\left[\zeta - \frac{1}{a(1-\nu/2)}\right], \tag{3.56}$$

$$\phi(X) = w\phi_\zeta, \tag{3.57}$$

where

$$w = \left[a\left(1-\frac{\nu}{2}\right)\right]^{-\frac{3\nu}{4(1-\nu/2)}}, \tag{3.58}$$

$$\phi_\zeta = \zeta^{-\frac{3\nu}{4(1-\nu/2)}}. \tag{3.59}$$

It is shown in [90] that, by the spatial scaling ζ in (3.55) and introducing the new voltage variable $\Psi(\zeta;t)$ via

$$V(\zeta;t) = \phi_\zeta \Psi^*(\zeta;t), \tag{3.60}$$

where

$$\Psi^*(\zeta;t) = e^{-t/\tau_m}\Psi(\zeta;t), \tag{3.61}$$

the passive tapered cable equation (1.27) given $\rho(x) = r(x)$ can be rewritten as

$$-\frac{\partial \Psi(\zeta;t)}{\partial t} = \hat{H}\Psi(\zeta;t), \tag{3.62}$$

where the operator

$$\hat{H} = -D_0 \frac{\partial^2}{\partial \zeta^2} + \frac{3\nu(5\nu-4)}{4(2-\nu)^2}\frac{D_0}{\zeta^2}, \tag{3.63}$$

and

$$D_0 = \frac{\lambda_0^2}{\tau_m}, \tag{3.64}$$

is a constant. Eq. (3.62) can thus be analytically solved if $\nu = 4/5$, in which case it reduces to a normalised Helmholtz equation. The same result immediately extends to the resonant cables. Again, introducing the variable ζ defined by Eq. (3.55), Eq. (3.27) becomes

$$\mathcal{E}(\omega)V = \frac{r_0}{2R_a}\left[\frac{\partial^2 V}{\partial\zeta^2} + \frac{3\nu}{2(1-\nu/2)}\frac{1}{\zeta}\frac{\partial V}{\partial\zeta}\right] + I_0. \tag{3.65}$$

Substituting it into Eq. (3.60) gives,

$$\left[\frac{2R_a}{r_0}\mathcal{E}(\omega) + \frac{3\nu(5\nu-4)}{4(2-\nu)^2}\frac{1}{\zeta^2} - \frac{\partial^2}{\partial\zeta^2}\right]\Psi^* = \frac{2R_a}{r_0\phi_\zeta}I_0. \tag{3.66}$$

Note that both scaled variables ζ and Ψ^* defined in [90] are linear in X and V^* due to Eqs. (3.56) and (3.57). Eq. (3.66) can be therefore rewritten as

$$\left[R_m\mathcal{E}(\omega) + \frac{3\nu(5\nu-4)}{4(2-\nu)^2}\left(X + \frac{1}{\lambda_0 a(1-\nu/2)}\right)^{-2} - \frac{\partial^2}{\partial X^2}\right]V^* = \frac{I_0}{g_l\phi}. \tag{3.67}$$

If $\nu = 4/5$, Eq. (3.67) reduces to

$$\left[R_m\mathcal{E}(\omega) - \frac{\partial^2}{\partial X^2}\right]V^* = \frac{I_0}{g_l\phi}, \tag{3.68}$$

which turns out to be a special case of Eq. (3.10), by noting that $R_m\mathcal{E}(\omega)$ in Eq. (3.68) and $\gamma^2(X;\omega)$ defined by Eq. (3.11) are equal if $\beta(X) = 1$. Among the six types of taper, only the Quadratic type leads to $\beta(X) = 1$. This is not a coincidence. Since the dendritic radius is described by

$$r = r_0(1+ax)^{4/5}, \tag{3.69}$$

the geometric ratio can be found as

$$F(X) = \frac{r_0^{3/2}}{\lambda_*}(1+ax)^{6/5}, \tag{3.70}$$

and Eq. (3.53) gives

$$X = \frac{5}{3\lambda_0 a}\left[(1+ax)^{3/5} - 1\right]. \tag{3.71}$$

$F(X)$ can thus be found explicitly as

$$F(X) = \frac{r_0^{3/2}}{\lambda_*}\left(1 + \frac{3\lambda_0 a}{5}X\right)^2, \tag{3.72}$$

which is essentially the Quadratic type of taper found in §3.2.1 with

$$L = -\frac{5}{3\lambda_0 a}. \tag{3.73}$$

Therefore, the plot of $r(x)$ of the Quadratic type of type in Fig. 3.2 (the red conical curve in the bottom right corner) follows a power law with the power $\nu = 4/5$.

If $\nu \notin \{0, 4/5, 2\}$, Eq. (3.67) cannot be reduced to the normalised Helmholtz equation (2.36). Nonetheless, by a constant translation $(\lambda_0 a(1 - \nu/2))^{-1}$ of X, it can be recast into the same form as Eq. (3.35), where

$$C_0 = \frac{3\nu(5\nu - 4)}{4(2 - \nu)^2}. \tag{3.74}$$

Thus, in this case, we can also obtain the Green's function of (3.67) in terms of Bessel functions.

3.3 Sum-over-trips on reducible tapers

Here we consider a tapered dendritic tree, and the membrane potential dynamics on each branch i of it is described by

$$C_{m,i}\frac{\partial V_i}{\partial t} = -g_{l,i}V_i - I_{h,i} + \frac{1}{2R_{a,i}\rho_i(x)}\frac{\partial}{\partial x}\left[r_i^2(x)\frac{\partial V_i}{\partial x}\right] + I_{0,j}(x;t), \tag{3.75a}$$

$$L_{h,i}\frac{\partial I_{h,i}}{\partial t} = -r_{h,i}I_{h,i} + V_i. \tag{3.75b}$$

where

$$I_{0,j}(x;t) = \frac{I_{\text{inj}}(t)\delta(x - y)\delta_{ij}}{2\pi\rho(x)}. \tag{3.76}$$

Assume all the dendritic branches are constrained to be one of the six types of taper (listed in Table 3.1). As all dendritic branches are reducible tapers, such a dendritic tree is called a "reducible dendrites" in this thesis. We can follow the same steps in §3.2.1, using the spatial mapping μ_i as defined in (3.2) and introducing new voltage variable V_i^* as defined in (3.5) on each branch i, to recast the system (3.75) into the frequency domain as

$$\left[\gamma_i^2(X;\omega) - \frac{\partial^2}{\partial X^2}\right] V_i^*(X;\omega) = \frac{I_{0,j}(\mu^{-1}(X);\omega)}{g_{l_i}\phi_i(X)}, \tag{3.77}$$

where

$$\gamma_i(X;\omega) = \sqrt{\tau_{m,i}\omega + \beta_i(X) + \frac{1}{(r_{h,i} + L_{h,i}\omega)g_{l,i}}}, \tag{3.78}$$

and $\beta_i(X)$ is a constant by assumption. It is now straightforward to see the similarity between Eqs. (3.77) and (2.43), and the two mappings μ, γ formed respectively from the ensembles of μ_i, γ_i for all i are simple generalisations from the mappings (2.20) and (2.45). Therefore, we can follow the same steps as in §2.3.2 to show that, similar to cylindrical dendrites, on a dendritic tree with reducible tapers, $\Gamma_0 = \gamma \cdot \mu(\Gamma)$ is a quantum graph, and that the framework of sum-over-trips and the method of local point matching can be applied. However, the boundary conditions for V^* on Γ_0 are different from those for V on Γ due to the voltage scaling ϕ defined in (3.6). The node factors for tapered dendrites are thus generally different from those for cylindrical dendrites listed in §2.3.2.

3.3.1 Green's functions on reducible dendrites

Since $\gamma_i(X;\omega)$ is constant in X for all i on a reducible dendrites, Eq. (3.77) can be reduces to

$$(\nabla^2 - 1)V_i^*(\mathcal{X};\omega) = -I_N(\mathcal{X};\omega), \tag{3.79}$$

which is identical to Eq. (2.46) in expression, but

$$I_N(\mathcal{X};\omega) = \frac{I_{0,j}(\mu^{-1}(\gamma^{-1}(\mathcal{X}));\omega)}{g_{l,i}\gamma_j^2(\omega)\phi_i(\gamma^{-1}(\mathcal{X}))}. \tag{3.80}$$

The sum-over-trips framework gives

$$V_i^*(\mathcal{X};\omega) = \sum_k \int_0^{\mathcal{L}_k} H_{ik}(\mathcal{X},\mathcal{Z})I_N(\mathcal{Z};\omega)d\mathcal{Z}, \tag{3.81}$$

where

$$H_{ik}(\mathcal{X},\mathcal{Z}) = \sum_{r\in\mathbb{T}} A_r(\omega)H_\infty(\mathcal{L}_r(x,z)). \tag{3.82}$$

with H_∞ defined in (2.38) and $\mathcal{L}_r(x,y) = \gamma(L_r(x,y))$ being the normalised trip length as in §2.3.2, and $A_r(\omega)$ is the trip coefficient, a product of new node factors for tapered dendrites to be determined in §3.3.2. Eq. (3.81) can then be scaled back to the original coordinate by Eq. (3.6), which gives,

$$V_i(x;\omega) = G_{ij}(x,y;\omega)I_{\text{inj}}(\omega), \tag{3.83}$$

where the Green's function on a dendritic tree with the reducible tapers is explicitly

$$G_{ij}(x,y;\omega) = \frac{\Phi_{ji}(y,x)}{z_j(y;\omega)} \sum_{r\in\mathbb{T}} A_r(\omega) H_\infty(\mathcal{L}_r(x,y)). \tag{3.84}$$

The variables

$$\Phi_{ji}(y,x) = \frac{\phi_i(\mu_i(x))}{\phi_j(\mu_j(y))}, \tag{3.85}$$

$$z_j(y;\omega) = \frac{\gamma_j(\omega)}{\lambda_j(y) r_{a,j}(y)}, \tag{3.86}$$

$$r_{a,j}(y) = \frac{R_{a,j}}{\pi r_j^2(y)}, \tag{3.87}$$

are defined in the same forms as in (3.16) - (3.18) for an infinite cable with extra subscripts indexing dendritic branches. The coefficient before the infinite sum here is notably different from that in Eq. (2.50). Nonetheless, the Green's function (3.84) can be reduced to Eq. (2.50) in the cylindrical cases, which is to be shown in §3.3.4.

3.3.2 Node factors for reducible dendrites

Here I derive new node factors for a dendritic tree with reducible tapers. To start with, rewrite Eq. (3.84) as

$$G_{ij}(x,y;\omega) = \eta_j(y)\phi_i(\mu_i(x)) \sum_{r\in\mathbb{T}} A_r(\omega) H_\infty(\mathcal{L}_r(x,y)), \tag{3.88}$$

where

$$\eta_j(y) = \frac{1}{z_j(y;\omega)\phi_j(\mu_j(y))}, \tag{3.89}$$

only dependent on y, is a constant in x for any fixed input. As on cylindrical dendrites, a node factor in the sum-over-trips framework on tapered dendrites also encodes the information of the boundary conditions at the corresponding type of nodes on a dendritic tree. Since their effects are local (explained in §2.2.2 by the Markovian property of random walks), without loss of generality we can derive node factors for different type of nodes attached to semi-infinite dendritic branches (i.e. in absence of other boundary conditions). Thus, in the following sections, I will impose boundary conditions defined by the four types of nodes discussed in §1.2.4 onto the Green's function (3.88). By solving the systems, the generalised node factors for reducible dendrites can be obtained. This procedure also serves as a constructive proof for the original node factors listed in §2.3.2 successively. To save notations,

the spatial coordinates are changed from case to case so that the node always locates at $x = 0$. In addition, ω is omitted in all the expressions.

Terminal node factors

With only one terminal, the dendritic structure is simply a semi-infinite cable. By the sum-over-trips framework, there are two and only two trips, a direct trip and a reflective one. Eq. (3.88) is thus reduced to

$$G(x, y) = \eta(y)\phi(X) \left[H_\infty(\gamma Y - \gamma X) + \alpha_k H_\infty(\gamma Y + \gamma X) \right], \tag{3.90}$$

where α_k for $k \in \{o, c\}$ is the reflective node factor at open and closed terminals respectively. Note that the subscripts of branch indices are omitted due the presence of only one dendritic branch.

If the terminal is open, the boundary condition (1.35) is imposed, which gives

$$G(0, y) = 0. \tag{3.91}$$

Substituting Eq. (3.90) into the condition (3.91) leads to

$$\eta(y)\phi(0)(1 + \alpha_o)H_\infty(\gamma Y) = 0, \tag{3.92}$$

which simply gives

$$\alpha_o = -1, \tag{3.93}$$

because all the other terms on the left hand side in Eq. (3.92) are positively defined.

If the terminal is closed, the boundary condition (1.36) is imposed, which gives

$$\left.\frac{\partial G}{\partial x}\right|_{x=0} = 0. \tag{3.94}$$

By the chain rule,

$$\left.\frac{\partial G}{\partial x}\right|_{x=0} = \frac{dX}{dx}\left.\frac{\partial G}{\partial X}\right|_{X=0} = \frac{1}{\lambda(0)}\left.\frac{\partial G}{\partial X}\right|_{X=0}, \tag{3.95}$$

which implies,

$$\left.\frac{\partial G}{\partial X}\right|_{X=0} = 0. \tag{3.96}$$

To calculate the derivative, the following identity is worth noting,

$$\frac{\partial}{\partial X} H_\infty(\gamma X) = -\gamma H_\infty(\gamma X) \tag{3.97}$$

which can be easily deduced from the definition of $H_\infty(\gamma X)$. Thus,

$$\frac{\partial G}{\partial X} = \eta(y)\phi(X)\left(\left[\gamma - \frac{1}{2}\xi(X)\right]H_\infty(\gamma Y - \gamma X) - \alpha_c\left[\gamma + \frac{1}{2}\xi(X)\right]H_\infty(\gamma Y + \gamma X)\right), \tag{3.98}$$

which gives

$$\left.\frac{\partial G}{\partial X}\right|_{X=0} = \eta(y)\phi(0)\left(\left[\gamma - \frac{1}{2}\xi(0)\right] - \alpha_c\left[\gamma + \frac{1}{2}\xi(0)\right]\right)H_\infty(\gamma Y). \tag{3.99}$$

Substituting Eq. (3.96) into the condition (3.99) gives

$$\alpha_c = \frac{\gamma - \xi(0)/2}{\gamma + \xi(0)/2}. \tag{3.100}$$

Branching node factors

Assume that N semi-infinite dendritic cables are attached to a branching node, and without loss of generality the input location y is on branch 1. There are generally two cases, the output locates either on the same branch 1, or on a different branch $k \neq 1$. Let $\alpha_k = \alpha_{k1}$ for $k \in \{1, 2, 3, ..., N\}$ be the node factors for the trip travels from branch k to 1. The sum-over-trips framework reduces the Green's function (3.88) to

$$G_1(x_1, y) = \eta_1(y)\phi_1(X)\left[H_\infty(\gamma_1 Y - \gamma_1 X) + \alpha_1 H_\infty(\gamma_1 Y + \gamma_1 X)\right], \tag{3.101a}$$

$$G_k(x_k, y) = \eta_1(y)\phi_k(X)\alpha_k H_\infty(\gamma_1 Y + \gamma_k X), \qquad \text{for } k \neq 1. \tag{3.101b}$$

According to the continuity of membrane potentials (1.38),

$$G_1(0, y) = G_k(0, y), \tag{3.102}$$

which gives

$$\phi_1(0)(1 + \alpha_1) = \phi_k(0)\alpha_k, \tag{3.103}$$

for $k \neq 1$, by simply substituting Eqs. (3.101) into the condition (3.103). Meanwhile, the conservation of electrical currents (1.37) must be satisfied, that is,

$$0 = \sum_{k=1}^{N} \frac{1}{r_{a,k}(0)} \left.\frac{\partial G_k}{\partial x}\right|_{x=0} = \sum_{k=1}^{N} \frac{1}{r_{a,k}(0)\lambda_k(0)} \left.\frac{\partial G_k}{\partial X}\right|_{X=0}, \tag{3.104}$$

where

$$\left.\frac{\partial G_1}{\partial X}\right|_{X=0} = \eta_1(y)\phi_1(0)\left(\left[\gamma_1 - \frac{1}{2}\xi_1(0)\right] - \alpha_1\left[\gamma_1 + \frac{1}{2}\xi_1(0)\right]\right) H_\infty(\gamma_1 Y), \quad (3.105a)$$

$$\left.\frac{\partial G_k}{\partial X}\right|_{X=0} = \eta_1(y)\phi_k(0)\left(-\alpha_k\left[\gamma_k + \frac{1}{2}\xi_k(0)\right]\right) H_\infty(\gamma_1 Y). \quad (3.105b)$$

Substituting Eqs. (3.105) into the condition (3.104) leads to

$$0 = 2z_1(0) - (\alpha_1 + 1)\sum_{k=1}^{N} z_k^*(0), \quad (3.106)$$

where

$$z_k^*(x) = \frac{\gamma_k + \xi_k(x)/2}{\lambda_k(x) r_{a,k}(x)}. \quad (3.107)$$

Combining Eqs. (3.103) and (3.106), α_1 can be easily solved and then α_k is found to be,

$$\alpha_1 = \frac{2z_1(0)}{\sum_{k=1}^{N} z_k^*(0)} - 1, \quad (3.108)$$

$$\alpha_k = \frac{2z_1(0)}{\sum_{k=1}^{N} z_k^*(0)}\Phi_{k1}^{(\chi)}, \qquad \text{for } k \neq 1, \quad (3.109)$$

where $z_i(0)$ is defined by Eq. (3.86), χ denotes the node at which segment n is attached to m, and

$$\Phi_{nm}^{(\chi)} = \Phi_{nm}(0,0) = \frac{\phi_m(0)}{\phi_n(0)}, \quad (3.110)$$

It is worth noting that, whereas $\Phi_{nm}^{(\chi)} = 1$ here, it is a local variable that changes every time the spatial coordinate is changed, while all the other variables presented in the node factors (here and those to be found in later sections) are evaluated independent of the spatial coordinate, e.g. $\lambda_k(x), r_{a,k}(x)$. In order to enforce $\Phi_{nm}^{(\chi)}$ to be a global variable, the X-coordinates on all tapered branches should be chosen to satisfy the following condition

$$r_i(x) = r_j(y) \Leftrightarrow F_i(X) = F_j(Y), \qquad \text{for any } x \neq y. \quad (3.111)$$

A convenient choice is $F_0 = 1$ for all branches, which reduces the definition (3.4) of the geometric ratio of any branch i to

$$F_i(X) = F_i(\mu_i(x)) = \frac{r_i^2(x)}{\lambda_i(x)}. \quad (3.112)$$

As a result,

$$\Phi^{(\chi)}_{nm} = \Phi_{nm}(\chi_n, \chi_m) = \frac{\phi_m(\chi_m)}{\phi_n(\chi_n)} = \left[\frac{F_n(\chi_n)}{F_m(\chi_m)}\right]^{1/2}. \tag{3.113}$$

Although χ_m, χ_n coincide at the same point χ, they represent two different spatial coordinates on branch m and n respectively.

Somatic node factors

Assume that N semi-infinite dendritic cables are attached to a soma, and the input location y is on branch 1. Since the branching structure is the same as in the previous section, the Green's functions G_1, G_k here are the same as in Eqs. (3.101). However, the boundary conditions imposed on them are changed due to the presence of the soma instead of an ordinary branching node.

The model of the soma is given by Eqs. (1.39a) and (1.39b). The Laplace transform leads to

$$z_S V_S = \sum_{i=1}^{N} \frac{1}{r_{a,i}(0)} \frac{\partial V_i}{\partial x}\bigg|_{x=0}, \tag{3.114}$$

where z_S is defined in (2.57). In addition, the continuity of membrane potentials (1.39c) implies the same condition as (3.102),

$$G_1(0, y) = G_k(0, y) = G_S(y), \tag{3.115}$$

where $G_S(y)$ is the somatic Green's function, which is the fundamental solution to Eq. (3.114). Equivalently,

$$z_S G_1(0, y) = \sum_{k=1}^{N} \frac{1}{\lambda_k(0) r_{a,k}(0)} \frac{\partial G_k}{\partial X}\bigg|_{X=0}, \tag{3.116}$$

whose left hand side is simply, by substitution,

$$z_S \eta_1(y) \phi_1(0)(1 + \alpha_1) H_\infty(\gamma_1 Y), \tag{3.117}$$

and right hand side can be reduced to

$$\eta_1(y)\phi_1(0) H_\infty(\gamma_1 Y) \left[\frac{2\gamma_1}{\lambda_1(0) r_1(0)} - (\alpha_1 + 1) \sum_k \frac{\gamma_k + \xi_k(0)/2}{\lambda_k(0) r_k(0)}\right], \tag{3.118}$$

by using the derivatives found previously in Eqs. (3.105). The two expressions

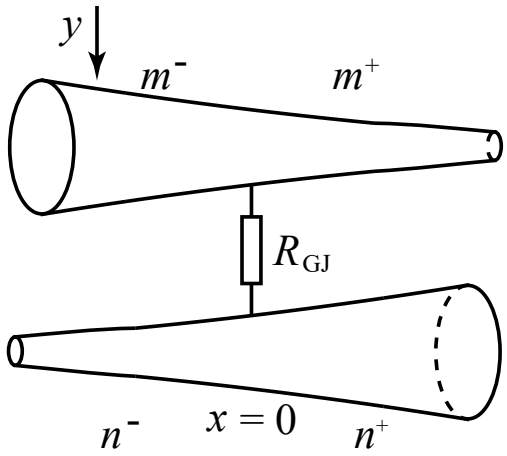

Figure 3.5: A schematic of the gap-junctional node with a coupling conductance $g_{GJ} = R_{GJ}^{-1}$ connecting dendritic branch m to n. The two branches are not necessary to be of the same shape.

(3.117) and (3.118) are equal, that is,

$$z_S(1+\alpha_1)2z_1(0) = (\alpha_1+1)\sum_{k=1}^{N} z_k^*(0), \tag{3.119}$$

which therefore gives

$$\alpha_1 = \frac{2z_1(0)}{z_S + \sum_{k=1}^{N} z_k^*(0)} - 1, \tag{3.120}$$

$$\alpha_k = \frac{2z_1(0)}{z_S + \sum_{k=1}^{N} z_k^*(0)} \Phi_{k1}^{(\chi)}, \qquad \text{for } k \neq 1. \tag{3.121}$$

Gap-junctional node factors

At a gap junction that connects dendritic branch m to n, assume that the input location y is on segment m^-, i.e. the segment on branch m before the gap junction (see Fig. 3.5). For $k \in \{m^-, m^+, n^-, n^+\}$, the Green's function (3.88) reduces to

$$G_k(x_k, y) = \eta_m(y)\phi_k(x_k)\left[\delta_{km^-} H_\infty(\gamma_m Y - \gamma_m X) + \alpha_k H_\infty(\gamma_m Y + \gamma_k X)\right], \tag{3.122}$$

The continuity of membrane potentials (1.41) requires

$$G_{m^-}(0, y) = G_{m^+}(0, y), \tag{3.123a}$$

$$G_{m^-}(0, y) = G_{m^+}(0, y), \tag{3.123b}$$

which gives,

$$1 + \alpha_{m^-} = \alpha_{m^+}, \tag{3.124a}$$

$$\alpha_{n^-} = \alpha_{n^+}. \tag{3.124b}$$

At the same time, the conservation of currents boundary condition (1.40) requires

$$\frac{1}{r_{a,m}(0)} \left[\frac{\partial G_{m^-}}{\partial x} + \frac{\partial G_{m^+}}{\partial x} \right]_{x=0} = g_{GJ}(G_{m^-}(0,y) - G_{n^-}(0,y)), \tag{3.125a}$$

$$\frac{1}{r_{a,n}(0)} \left[\frac{\partial G_{n^-}}{\partial x} + \frac{\partial G_{n^+}}{\partial x} \right]_{x=0} = g_{GJ}(G_{n^-}(0,y) - G_{m^-}(0,y)), \tag{3.125b}$$

where

$$\left.\frac{\partial G_k}{\partial x}\right|_{x=0} = \frac{\eta_m(y)\phi_k(0)}{\lambda_k(0)} \left(\delta_{km^-} \left[\gamma_m - \frac{1}{2}\xi_m(0) \right] - \alpha_k \left[\gamma_k + \frac{1}{2}\xi_k(0) \right] \right) H_\infty(\gamma_m Y) \tag{3.126}$$

is obtained from Eqs. (3.95) and (3.105). All together, $\alpha_{m^+}, \alpha_{m^-}, \alpha_{n^+}, \alpha_{n^-}$ can be found by combining Eqs. (3.124) and (3.125). It is cumbersome but trivial and thus omitted here. The results are explicitly

$$1 + \alpha_{m^-} = \alpha_{m^+} = \frac{z_m(0)(1 + 2R_{GJ} z_n^*(0))}{z_m^*(0) + z_n^*(0) + 2R_{GJ} z_m^*(0) z_n^*(0)}, \tag{3.127a}$$

$$\alpha_{n^-} = \alpha_{n^+} = \frac{z_m(0)\Phi_{km}^{(\chi)}}{z_m^*(0) + z_n^*(0) + 2R_{GJ} z_m^*(0) z_n^*(0)}. \tag{3.127b}$$

3.3.3 Summary of the generalised framework

To summarise, if all cable equations (3.75) on all the branches i of a dendritic tree are reducible to the normalised Helmholtz equation (2.36), the dendritic tree is reducible to a quantum graph. Therefore, $G_{ij}(x, y; \omega)$ on the dendrites can be found by the generalised sum-over-trips framework as Eq. (3.84), where $\mathcal{L}_r(x, y)$ is the normalised trip length and the trip coefficient $A_r(\omega)$ is the product of all node factors α_{nm} along the trip.

If the transition probabilities at branching, somatic and gap-junctional nodes are written in the following forms, as they should be for random walks in the path

integral formulation,

$$p_k = \frac{z_k}{\sum_k z_k^*}, \tag{3.128a}$$

$$p_{S,k} = \frac{z_k}{z_S + \sum_k z_k^*}, \tag{3.128b}$$

$$p_{GJ,k} = \frac{z_k}{z_m^* + z_n^* + 2R_{GJ} z_m^* z_n^*}, \tag{3.128c}$$

the node factors found in §3.3.2 can be presented in more compact expressions:

- At a terminal χ of branch m,

$$\alpha_{mm} = -1, \qquad \text{if } \chi \text{ is open,} \tag{3.129a}$$

$$\alpha_{mm} = 2p_m - 1, \qquad \text{if } \chi \text{ is closed.} \tag{3.129b}$$

- At a branching or somatic node χ that connects branch m and n,

$$\alpha_{nm} = 2p_m \Phi_{nm}^{(\chi)} - \delta_{nm}, \qquad \text{for a branching node,} \tag{3.130a}$$

$$\alpha_{nm} = 2p_{S,m} \Phi_{nm}^{(\chi)} - \delta_{nm}, \qquad \text{for a somatic node.} \tag{3.130b}$$

- At a gap-junctional node χ that connects branch m and n,

$$\alpha_{nm} = p_{GJ,m} \Phi_{nm}^{(\chi)}, \qquad \text{if a trip passes through } \chi, \text{ so } m \neq n, \tag{3.131a}$$

$$\alpha_{mm} = p_{GJ,m} q_n - 1, \qquad \text{if a trip reflects at } \chi, \tag{3.131b}$$

$$\alpha_{mm} = p_{GJ,m} q_n, \qquad \text{if a trip passes by } \chi, \tag{3.131c}$$

  where

$$q_n = 1 + 2R_{GJ} z_n^*(\chi_n). \tag{3.132}$$

Note that all the variables are evaluated at the node χ where branch m and n are connected. There are similarities in the forms of Eqs. (3.129) and (3.130), as a closed terminal can be considered as a special case of a branching node with only one attached branch, and a branching node is indifferent to a somatic node in the limit $z_S \to 0$.

Similar to the sum-over-trips framework on cylindrical dendrites introduced in **Chapter 2**, the method of local point matching can be employed here to avoid the infinite sum in the Green's function (3.84). Instead of the definition (2.70), define

$$J_y = J_{ij}(x, y; \omega) = \frac{2z_j(y; \omega)}{\Phi_{ji}(y, x)} G_{ij}(x, y; \omega). \tag{3.133}$$

It is then straightforward to see the derivation of the method in §2.4.1 can be conducted in exactly the same steps. In practice, the method is employed by the algorithm summarised in §2.4.2 and J_y is obtained first. $G_{ij}(x, y; \omega)$ can then be found by Eq. (3.133).

3.3.4 Properties of the generalised framework

The generalised sum-over-trips framework is a natural extension of the original framework from cylindrical dendrites to reducible dendrites. It shares with the original framework all properties discussed in §2.3.3 and is applicable to all examples investigated in §2.4.3. Below I will show that, firstly, the generalised framework is equivalent to the original one when applied to cylindrical dendrites, and secondly the reciprocity principle (2.67) is still valid on reducible tapers. For other results, e.g. the presence of neuronal loops and the conditions for equivalent branches (not necessarily equivalent cylinders), the arguments are almost the same as in §2.3.3, and are thus omitted here.

Equivalence to the original framekwork on cylindrical dendrites

Apparently a cable equation on a cylindrical dendritic branch is always reducible to Eq. (2.36), and the generalised sum-over-trips framework on reducible dendrites can be applied to dendritic trees with cylindrical branches. However, it is worth noting that, if the branches of a dendritic tree are all cylindrical as assumed in **Chapter 2**, both the original framework on cylindrical dendrites and the generalised framework on tapered dendrites can be employed, but their Green's functions (2.50) and (3.84) have different expressions. Here I prove the two expressions are indeed identical.

Firstly, the normalised trip length $\mathcal{L}_r(x, y)$ are indifferent in the two Green's functions, because the characteristic length parameter $\lambda(x)$ is a constant on each cylindrical branch; its definition (3.1) reduces to (1.31). Thus, $H_\infty(\mathcal{L}_r(x, y))$ are identical in the two expressions. Secondly, all node factors α_{mm} are the same in the two frameworks. On a cylindrical dendritic branch k, $\xi_k(\mu_k(x)) = 0 \Rightarrow z_k^*(x; \omega) = z_k(\omega)$ for all x, because the dendritic radius $r_k(x) = r_k$ is a constant. $\phi_k(\mu_k(x)) = \phi_k$ also becomes a constant dependent on k only, and thus I can write $\Phi_{nm} = \phi_m/\phi_n$ for $\Phi_{nm}^{(\chi)}$, particularly $\Phi_{kk} = 1$. It is immediate to see all reflective node factors defined in (3.129) and (3.130) simply reduced to those defined in §2.3.2 for the original framework. In addition, at a gap junction, $p_{GJ,m}q_n = 1 - p_{GJ,n}$ reduces α_{mm} defined in (3.131b) and (3.131c) to the expressions (2.59) and (2.60) respectively.

However, for the transitive node factors, $m \neq n$, $\alpha_{nm}^t = \alpha_{nm}^c \Phi_{nm} \neq \alpha_{nm}^c$, because

$\xi_k = 0$ but in general $\Phi_{nm} \neq 1$. Note here the superscript t is added for the generalised node factors defined by Eqs. (3.130) and (3.131), and c for the original node factors. Recall the trip coefficient $A_r^c(\omega)$ for an arbitrary trip (2.62) is

$$A_r^c(\omega) = \alpha_{k_0k_1}^c \alpha_{k_1k_2}^c \alpha_{k_2k_3}^c \dots \alpha_{k_{n-1}k_n}^c \alpha_{k_nk_{n+1}}^c, \tag{3.134}$$

where $k_0 = i, k_{n+1} = j$. Similarly, by the generalised framework,

$$\begin{aligned} A_r^t(\omega) &= \alpha_{k_0k_1}^t \alpha_{k_1k_2}^t \alpha_{k_2k_3}^t \dots \alpha_{k_{n-1}k_n}^t \alpha_{k_nk_{n+1}}^t \\ &= \alpha_{k_0k_1}^c \Phi_{k_0k_1} \alpha_{k_1k_2}^c \Phi_{k_1k_2} \alpha_{k_2k_3}^c \Phi_{k_2k_3} \dots \alpha_{k_{n-1}k_n}^c \Phi_{k_{n-1}k_n} \alpha_{k_nk_{n+1}}^c \Phi_{k_nk_{n+1}}. \end{aligned} \tag{3.135}$$

Thus, their ratio can be found as

$$\frac{A_r^t(\omega)}{A_r^c(\omega)} = \Phi_{k_0k_1} \Phi_{k_1k_2} \Phi_{k_2k_3} \dots \Phi_{k_{n-1}k_n} \Phi_{k_nk_{n+1}} = \frac{\phi_j}{\phi_i} = \Phi_{ij}, \tag{3.136}$$

which leads to

$$\frac{\sum A_r^t(\omega) H_\infty(\mathcal{L}_r(x,y))}{\sum A_r^c(\omega) H_\infty(\mathcal{L}_r(x,y))} = \Phi_{ij}, \tag{3.137}$$

where both infinite sums are over all the trips $r \in \mathbb{T}$, because the set $\mathbb{T}$ are identical in the original and generalised frameworks. It is then straightforward to see this ratio (3.137) cancelling out the preceding coefficient Φ_{ji} in the Green's function (3.84), which recovers the Green's function (2.50) found directly by the original sum-over-trips framework on cylindrical dendrites.

The reciprocity principle on dendrites with reducible tapers

For any trip r and its reversal configuration $-r$ on a dendritic tree with reducible tapers, the ratio between their trip coefficients is

$$\frac{A_r(\omega)}{A_{-r}(\omega)} = \frac{\alpha_{ik_1} \alpha_{k_1k_2} \alpha_{k_2k_3} \dots \alpha_{k_{n-1}k_n} \alpha_{k_nj}}{\alpha_{jk_n} \alpha_{k_nk_{n-1}} \alpha_{k_{n-1}k_{n-2}} \dots \alpha_{k_2k_1} \alpha_{k_1i}}, \tag{3.138}$$

assuming, without loss of generality, all node factors α_{nm} where $m = n$ have cancelled each other out.

For any $\alpha_{k_mk_{m+1}}, \alpha_{k_{m+1}k_m}$, which are defined by either Eq. (3.130a), or (3.130b), or (3.131a), in accordance with the type of node χ_m,

$$\frac{\alpha_{k_mk_{m+1}}}{\alpha_{k_{m+1}k_m}} = \frac{z_{k_{m+1}}(\chi_m;\omega)}{z_{k_m}(\chi_m;\omega)} \left[\Phi_{k_mk_{m+1}}^{(\chi_m)}\right]^2, \tag{3.139}$$

for all $m \in \{0, 1, 2, \dots, n\}$, where $k_0 = i, k_{n+1} = j$, and branch k_m and k_{m+1} are

connected at node χ_m. By definition,

$$\left[\Phi_{ji}(y,x)\right]^2 = \frac{\lambda_i(x)}{r_i^2(x)}\frac{r_j^2(y)}{\lambda_j(y)}, \tag{3.140}$$

$$\frac{z_i(x)}{z_j(y)} = \frac{\gamma_i(\omega)r_i^2(x)}{\lambda_i(x)}\frac{\lambda_j(y)}{\gamma_j(\omega)r_j^2(y)}, \tag{3.141}$$

which leads to

$$\frac{z_i(x;\omega)}{z_j(y;\omega)}\left[\Phi_{ji}(y,x)\right]^2 = \frac{\gamma_i(\omega)}{\gamma_j(\omega)}. \tag{3.142}$$

Thus, the ratio (3.139) can be found as

$$\frac{\alpha_{k_m k_{m+1}}}{\alpha_{k_{m+1}k_m}} = \frac{\gamma_{k_{m+1}}(\omega)}{\gamma_{k_m}(\omega)}, \tag{3.143}$$

which further reduces the ratio (3.138) to

$$\frac{A_r(\omega)}{A_{-r}(\omega)} = \frac{\gamma_j(\omega)}{\gamma_i(\omega)}. \tag{3.144}$$

Since any trip has one and only one reversal trip, and they are identical in their normalised length,

$$\frac{\sum A_r(\omega)H_\infty(\mathcal{L}_r(x,y))}{\sum A_{-r}(\omega)H_\infty(\mathcal{L}_{-r}(y,x))} = \frac{\gamma_j(\omega)}{\gamma_i(\omega)}, \tag{3.145}$$

where the sum is over all $r \in \mathbb{T}$. Therefore,

$$\frac{G_{ij}(x,y;\omega)}{G_{ji}(y,x;\omega)} = \frac{z_i(x;\omega)}{z_j(y;\omega)}\left[\Phi_{ji}(y,x)\right]^2\frac{\gamma_j(\omega)}{\gamma_i(\omega)} = 1, \tag{3.146}$$

where the first equality comes from Eq. (3.84) and the second one is given by Eq. (3.142).

3.4 Sum-over-trips on general tapers

The sum-over-trips framework is generalised for dendrites whose tapered geometries are constrained to be one of the six types listed in Table 3.1 in the last section §3.2. However, the realistic dendritic models discussed in §3.2.2 are in general beyond the capacity of the generalised framework, because the realistic tapers are not reducible. Moreover, real dendrites (e.g. Fig. 3.1) could be totally different from any idealised models. Below I will firstly deal with these realistic tapers in a theoretical manner, and then move onto the discussion over general dendritic geometries by applying the finite element method.

3.4.1 Green's functions on dendrites with realistic tapers

Following the steps in §3.2.2, for all dendritic branches i, we assume $[r_i'(x)]^2 \ll 1$, and consider the following system, simply extended from Eqs. (3.26) by adding the branch indices:

$$C_{m,i}\frac{\partial V_i}{\partial t} = -g_{l,i}V_i - I_{h,i} + \frac{1}{2R_{a,i}r_i(x)}\frac{\partial}{\partial x}\left[r_i^2(x)\frac{\partial V_i}{\partial x}\right] + I_0(x;t), \tag{3.147a}$$

$$L_{h,i}\frac{\partial I_{h,i}}{\partial t} = -r_{h,i}I_{h,i} + V_i, \tag{3.147b}$$

where the dendritic radius $r_i(x)$ is modelled by either an exponential decay (3.28) or some power law (3.45). Notably these two classes in fact covers all the six types of taper listed in Table 3.1 (with reasonable and accurate approximations) according to the discussions in §3.2.2, and trivially the cylindrical cases. By spatial scaling and translation, (3.147) is recast into

$$\left[R_{m,i}\mathcal{E}_i(\omega) + \frac{C_{0,i}}{X^2} - \frac{\partial^2}{\partial X^2}\right]V_i^* = \frac{I_0(X;\omega)}{g_{l,i}\phi_i}, \tag{3.148}$$

where

$$C_{0,i} = \begin{cases} \frac{15}{4}, & \text{if } r_i(x) \text{ follows an exponential decay (3.28),} \\ \frac{3\nu(5\nu-4)}{4(2-\nu)^2}, & \text{if } r_i(x) \text{ follows a } \nu\text{-power law (3.45),} \end{cases} \tag{3.149}$$

which is almost identical to Eq. (3.33) except for the branch indices. Thus, as in §3.2.2, we can eventually transform Eq. (3.148) into the Bessel differential equation (3.42).

Assume the Green's function of Eq. (3.33) is $B_\infty(\mathcal{L}(x,y))$ where $\mathcal{L}(x,y)$ is the normalised distance between x, y, if no boundary conditions are applied. The normalised distance here is defined in the same way as the normalised trip length to be defined in (3.151) for the general sum-over-trips framework on realistic tapers. If the entire dendritic tree can be reduced to an equivalent single branch, or if $C_{0,i}$ are identical for all i, we can find the Green's function of Eq. (3.148) as

$$G_{ij}(x,y;\omega) = \gamma_y\phi_j(y)\sum_{r\in\mathbb{T}} A_r(\omega)B_\infty(\mathcal{L}_r(x,y)), \tag{3.150}$$

by the general sum-over-trips framework. The normalised trip length is now

$$\mathcal{L}_r(x,y) = \gamma_y[\mu_i^*(x) + \cdots + \mu_k^*(l_k) + \cdots + \mu_j^*(y)], \tag{3.151}$$

where μ_i^* is the compound mapping by applying μ_i first and then the constant translation that leads to Eq. (3.148). In addition, the trip coefficient $A_r(\omega)$ can be found by the same steps as in §3.3.2.

However, if $C_{0,i}$ are not identical for all i, we cannot apply the general sum-over-trips framework, because Bessel functions of different parameters are used and B_∞ is essentially dependent on $C_{0,i}$. Since we are trying to model the dendritic geometry in a more realistic way while preserving some analytical tractability, the exponential decay (3.28) could be an interesting model as different rates of dendritic radius variation can be parameterised by different a (from a cylindrical branch with $a = 0$ to a steep one for $a < 0$). In addition, since

$$B_\infty(\mathcal{L}_r(x,y)) \neq B_\infty(\gamma_y\mu_i^*(x)) + \cdots + B_\infty(\gamma_y\mu_k^*(l_k)) + \cdots + B_\infty(\gamma_y\mu_j^*(y)), \quad (3.152)$$

the method of local point matching cannot be employed, because the deduction of the method is fundamentally based on Eq. (2.74), which is invalid if replacing H_∞ by B_∞. Therefore, the sum-over-trips framework is not in practice useful to compute the Green's function on a dendritic tree with realistic tapers. It involves two computationally difficult tasks: Bessel functions cannot be written in elementary functions, and the infinite sum by directly applying the sum-over-trips framework is badly convergent (see §2.3.3), whereas the approach is compatible with any linear systems in theory.

3.4.2 Green's functions on dendrites with general properties

In this section, we re-consider the system (3.75), which describes the membrane potential dynamics on a resonant dendritic tree, but here the dendritic radius $r_i(x)$ cannot be classified into the special casses of the reducible or realistic tapers discussed in previous sections. Nonetheless, since the system (given any boundary conditions) is linear in voltage, its Green's function always exists.

Sum-over-trips by the finite element method

In order to solve for the membrane potential dynamics on a reconstructed neuron, it is a common computational practice to employ the finite element method. For example, the simulation environment NEURON discretises the reconstruction into small segments, and simulates the dynamics on all of the segments simultaneously. In addition, recall our derivation of the Green's function for a passive infinite cable by the path integral formulation in §2.2.1, where the random walks constructed are initially a process discrete in space. Thus, Caudron et al. [70] naturally em-

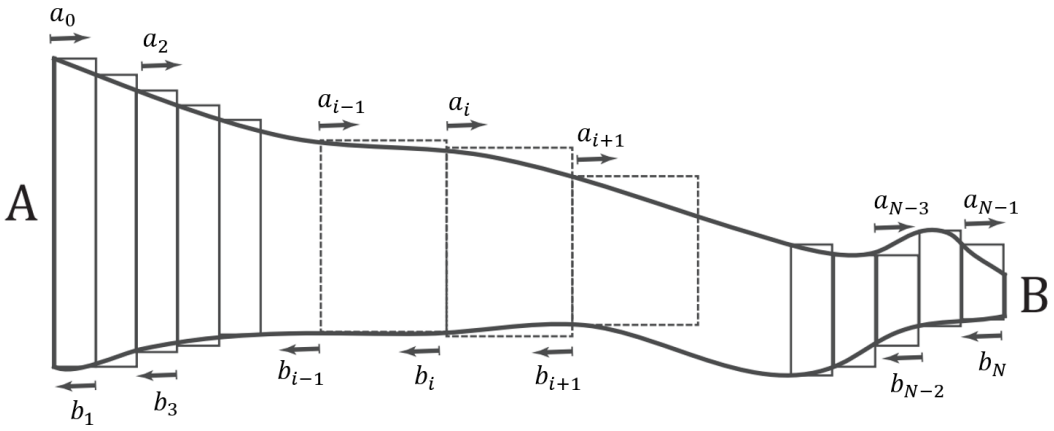

Figure 3.6: A schematic of a general tapered dendrite with finite partition. Since each segment is cylindrical, the sum-over-trips framework on cylindrical dendrites can be employed. Note a_{i-1}, b_i are placed at the left and right ends respectively on segment i.

ployed a Monte-Carlo method to evaluate the Green's function on finite partitions of morphological neurons. Likewise, we can discretise any tapered dendritic branch, or more generally any branch with continuously varying radius into little segments (see Fig. 3.6). By assuming that the dendritic radii of these little segments are locally constant, all the segments are cylindrical in geometry, and the sum-over-trips framework on cylindrical dendrites introduced in **Chapter 2** can be applied, whereas the framework cannot be employed directly.

To see whether and how it works to apply the sum-over-trips framework by the finite element method, we consider a "ball-and-stick" model whose dendritic topology is identical to that in §2.4.3 but the dendritic branch is tapered here. For the continuously tapered model, we assume the parabolic taper with a continuously varying radius $r(x)$ defined by Eq. (3.45), explicitly,

$$r(x) = r_0 \left[\frac{l-x}{l}\right]^2, \tag{3.153}$$

for $x \in [0, l_0]$, where $r_0 = r(0)$ is the initial dendritic radius. It has been discussed in §3.2.2 that the parabolic taper is almost equivalent to the Exponential type of taper (see Fig. 3.4) with

$$\kappa = \frac{3}{2l}\left[\frac{r_0 R_m}{2R_a}\right]^{1/2}, \tag{3.154}$$

in the geometric ratio (3.49). Notably $l \geq l_0$ controls the slope of the taper, and the equality can only be taken when the terminal radius $r_1 = r(l_0)$ is zero. If $r_1 = 0$,

the domain of $F(X)$ is $X \in [0, +\infty)$. Otherwise, $r_1 > 0$ and the upper bound for X is $L_0 = \mu(l_0) = -\ln(1 - l_0/l)/(\lambda_0 l)$, where the mapping μ is defined in (3.48).

We can use the local point matching method to construct the following system of J_v and J_w by following the arrows in Fig. 2.6 and noting the similarity to Eqs. (2.92),

$$J_v = \frac{1}{2}[\exp(\gamma_p(\omega)\mu(l_0))J_w + \exp(\gamma_p(\omega)\mu(x))](2p_{\mathrm{S},p} - 1), \tag{3.155a}$$

$$J_w = \frac{1}{2}[\exp(\gamma_p(\omega)\mu(l_0))J_v + \exp(\gamma_p(\omega)\mu(l_0 - x))](2p_{\mathrm{T},p} - 1), \tag{3.155b}$$

where $\gamma_p(\omega), p_{\mathrm{T},p}$ and $p_{\mathrm{S},p}$ can be found from their definitions (3.78), (3.128a) and (3.128b). Solving the system (3.155) results in

$$J_v = \frac{(2p_{S,p} - 1)\left[\left(\frac{l-l_0+x}{l}\frac{l-l_0}{l}\right)^{3\gamma_p(\omega)/2\kappa}(2p_{T,p} - 1) + \left(\frac{l-x}{l}\right)^{3\gamma_p(\omega)/2\kappa}\right]}{1 - (2p_{S,p} - 1)(2p_{T,p} - 1)\left(\frac{l-l_0}{l}\right)^{3\gamma_p(\omega)/\kappa}}, \tag{3.156a}$$

$$J_w = \frac{(2p_{T,p} - 1)\left[\left(\frac{l-x}{l}\frac{l-l_0}{l}\right)^{3\gamma_p(\omega)/2\kappa}(2p_{S,p} - 1) + \left(\frac{l-l_0+x}{l}\right)^{3\gamma_p(\omega)/2\kappa}\right]}{1 - (2p_{S,p} - 1)(2p_{T,p} - 1)\left(\frac{l-l_0}{l}\right)^{3\gamma_p(\omega)/\kappa}}, \tag{3.156b}$$

which leads to

$$G(x, y; \omega) = \frac{1}{2z(y; \omega)}[\exp(\gamma_p(\omega)\mu(y))J_v + \exp(\gamma_p(\omega)\mu(l_0 - y))J_w + \exp(\gamma_p(\omega)\mu(|x - y|))]. \tag{3.157}$$

For the discretised model, the tapered branch is assumed to be partitioned into an array of N cylinders. Each cylinder is of length l_0/N and radius

$$r_c(i) = \frac{r_m(i) + r_M(i) + \sqrt{r_m(i)r_M(i)}}{3}, \tag{3.158}$$

where

$$r_m(i) = r\left(\min_{x \in \Delta_i}(x)\right), \tag{3.159a}$$

$$r_M(i) = r\left(\max_{x \in \Delta_i}(x)\right), \tag{3.159b}$$

and Δ_i is the segment of compartment $i \in \{1, 2, 3, \ldots, N\}$. $r_c(i)$ thus approximately tracks the parabolic taper (see Fig. 3.7A), and guarantees the membrane surface areas are the same for the models. This multi-compartment model reduces to the

cylindrical "ball-and-stick" model when $N = 1$, and can also be considered as a variation of the model in Fig. 2.10. To solve the model, we employ the method of local point matching and construct

$$J_{a_i} = \frac{1}{2}\exp(\gamma_i^c l_i)\frac{2z_{i+1}}{z_i + z_{i+1}} J_{a_{i-1}} + \frac{1}{2}\exp(\gamma_{i+1}^c l_{i+1})\left(\frac{2z_{i+1}}{z_i + z_{i+1}} - 1\right) J_{b_{i+1}}, \quad (3.160a)$$

$$J_{b_i} = \frac{1}{2}\exp(\gamma_i^c l_i)\left(\frac{2z_i}{z_i + z_{i+1}} - 1\right) J_{a_{i-1}} + \frac{1}{2}\exp(\gamma_{i+1}^c l_{i+1})\frac{2z_i}{z_i + z_{i+1}} J_{b_{i+1}}, \quad (3.160b)$$

where J_{a_i} and J_{b_i} are unknown functions defined recursively at the point $i \in \{1, 2, 3, \ldots, N-1\}$, and i is also the index of segment $(i-1, i)$ (see Fig. 3.6). γ_i^c and z_i defined in (2.32) and (2.40) are also dependent on the segment index i. Note the argument ω is omitted. At the two ends of the branch,

$$J_{a_0} = \frac{1}{2}\exp(\gamma_1^c l_1)(2p_{S,c} - 1) J_{b_1}, \quad (3.161a)$$

$$J_{b_N} = \frac{1}{2}\exp(\gamma_{N-1}^c l_{N-1}) J_{a_{N-1}}. \quad (3.161b)$$

The system (3.160) and then the Green's functions can be solved subject to the boundary conditions (3.161). The numerical details can be found in **Appendix B**.

To investigate the difference in the signal amplitudes more closely, it is more convenient to study purely passive neurons injected by the step current input (1.64). The voltage responses at steady state ($t \to +\infty$) can be obtained directly by Eq. (1.66). Fig. 3.7 compares the discretised and the continuous models, by plotting the differences of their somatic responses at steady state as a function of the input location of the step current. It is clear that the differences are smaller when the number of the compartments N becomes larger. However, considering computational expenses, a tapered dendritic branch is partitioned into only a few segments (usually $N < 10$ [39, 88, 89]). Thus, with a small number of compartments, the discretised model approximates the continuous model worse than expected. In particular, the approximation on the last compartment (close to the terminal) is considerably bad; the difference is large even when N is large (see $N = 100$ in Fig. 3.7B). We should thus be careful with approximations on discretised models especially when the dendritic radius at the input location is small, because a marginal but inaccurate geometric approximation may cause a large difference in the value of input impedance.

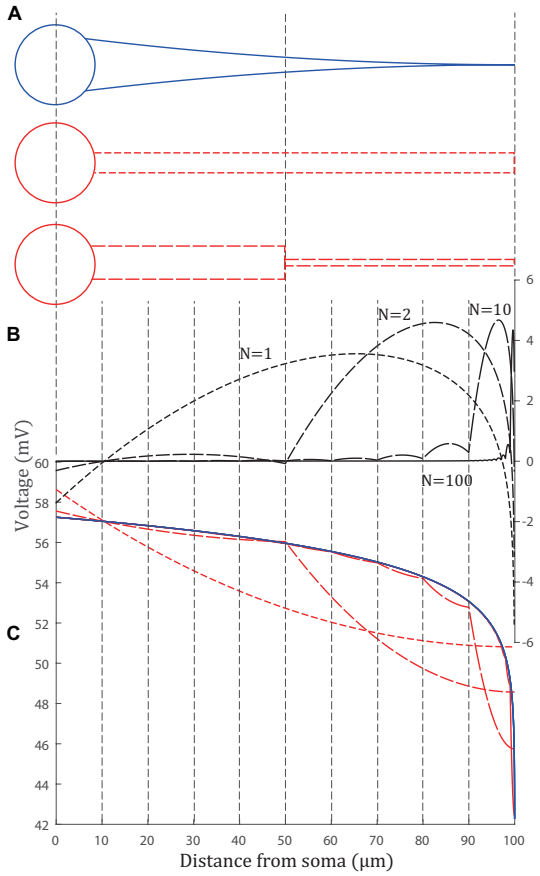

Figure 3.7: (**A**): Schematic shapes of the parabolic model (blue) and the multi-compartment models with $N = 1, 2$ (red). (**B**): Voltage differences between the somatic responses at steady state of the parabolic model and the multi-compartment models with $N = 1, 2, 10, 100$. (**C**): Somatic responses at steady state of the parabolic model (blue) and the multi-compartment models (red) with $N = 1, 2, 10, 100$ as a function of input location. (**B**) is the direct result of (**C**). All the models are purely passive, i.e. $r_h = r_{\text{soma}} \to +\infty$. All the other parameters are the same as in Fig. 4.1 except $R_a = 1000\ \Omega\cdot\text{cm}$.

Sum-over-trips on an infinite partition

It has been shown that the numerically solution to the difference equations (3.160) can be an accurate approximation for large N. Here the limit $N \to +\infty$ is considered. Under this limit, $l_i \to 0$, and the branch with continuously varying radius should be recovered. By defining $f_i = \exp(\gamma_i^c l_i)/2$, Eq. (3.160) can be rewritten as

$$J_{a_i}(2z_i + \Delta z_{i+1}) = (J_{a_i} - \Delta J_{a_i})(2z_i + 2\Delta z_{i+1})f_i + (J_{b_i} + \Delta J_{b_{i+1}})\Delta z_{i+1} f_{i+1}, \tag{3.162a}$$

$$J_{b_i}(2z_i + \Delta z_{i+1}) = (J_{a_i} - \Delta J_{a_i})(-\Delta z_{i+1})f_i + (J_{b_i} + \Delta J_{b_{i+1}})2z_i f_{i+1}, \tag{3.162b}$$

where Δ defines the increment for any variable from i to $i+1$. For example, if $x = 0$ is placed at the end A and $x = l$ at the end B, $l_i = \Delta x_i = x_i - x_{i-1}$. In addition,

$$f_{i+1} = 1 - \gamma_{i+1}^c \Delta x_{i+1} + \ldots, \tag{3.163}$$

by the Taylor expansion. Therefore, in the limit $N \to +\infty$, that is, all $\Delta x_i \to 0$, Eqs. (3.162) becomes a pair of differential equations,

$$2J_a z\gamma_c = (J_a + J_b)z' - 2zJ_a', \tag{3.164a}$$

$$-2J_b z\gamma_c = (J_a + J_b)z' - 2zJ_b', \tag{3.164b}$$

where J_a, J_b, γ_c, z are now assumed to be smooth in x. In addition, J_{a_0}, J_{b_N} are not defined by Eq. (3.162) as they are located at the ends. They should be written as boundary conditions

$$J_a(0) = J_A, \tag{3.165a}$$

$$J_b(l) = J_B, \tag{3.165b}$$

where J_A and J_B are additionally dependent on other branches attached to the two ends. Similarly,

$$J_b(0) = J_{\to A}, \tag{3.166a}$$

$$J_a(l) = J_{\to B}, \tag{3.166b}$$

where the subscripts $\to A, \to B$ represent the local trips that terminate at A, B respectively. If the branch is cylindrical, $J_{\to B} = J_A \exp(\gamma l)/2$ contributes to unknown J's on the branch attached to the end B. $J_{\to B}$ here is a generalisation as the branch is not cylindrical, but plays the same role in the method of local point matching.

Addition and subtraction of Eqs. (3.164) result in

$$w' + \gamma_c u = \frac{z'}{z} w, \tag{3.167a}$$

$$u' + \gamma_c w = 0, \tag{3.167b}$$

where

$$u = J_a - J_b, \tag{3.168}$$

$$w = J_a + J_b. \tag{3.169}$$

The system (3.167) leads to

$$u'' - \left[\frac{\gamma_c'}{\gamma_c} + \frac{z'}{z}\right] u' - \gamma_c^2 u = 0, \tag{3.170}$$

which is to be solved with the boundary conditions

$$u(0) = J_A - J_{\to A}, \tag{3.171a}$$

$$u(l) = J_{\to B} - J_B, \tag{3.171b}$$

given by Eqs. (3.165) and (3.166). It is worth noting after finding w by Eq. (3.167b), the Green's function can be directly obtained as

$$G(x, y; \omega) = \frac{1}{2z(y)} [J_a(y) + J_b(y)] = \frac{w(y)}{2z(y)}, \tag{3.172}$$

if the input location y is on the dendritic branch.

Recall the definitions of γ_c and $\mathcal{E}(\omega)$ in (2.32) and (1.58) respectively,

$$\gamma_c^2(x; \omega) = \frac{2R_a \mathcal{E}(\omega)}{r(x)}, \tag{3.173}$$

where the electrical parameters $R_a, \mathcal{E}(\omega)$ are assumed to be constants. Thus, Eq. (3.170) reduces to

$$u'' - 2[\ln r]' u' - \frac{2R_a \mathcal{E}}{r} u = 0. \tag{3.174}$$

Since the radius $r(x)$ is not a contant in x here, in general Eq. (3.174) has no analytical solution. When $r \propto (x + C_0)^2$ for some constant C_0, Eq. (3.174) reduces to a Cauchy-Euler equation, which can be solved analytically. However, such radius defines a parabolic taper, which is discussed in the previous sections.

Dendrites with heterogeneous electrical properties

Throughout this thesis, all the electrical parameters are assumed to be constants everywhere on the dendritic tree. However, in this section the electrical properties are considered to be continuously varying along a branch, that is, in general,

$$\gamma_c^2(x;\omega) = \frac{2R_a(x)}{r_c}\mathcal{E}(x;\omega), \tag{3.175a}$$

$$\gamma_t^2(X;\omega) = R_m(X)\mathcal{E}(X;\omega) + \beta(X) - 1, \tag{3.175b}$$

where

$$\mathcal{E}(x;\omega) = C_m(x)\omega + g_l(x) + \frac{1}{r_h(x) + L_h(x)\omega} \tag{3.176}$$

is modified from its original definition (1.58) so that it is now dependent on x. Similarly, $\mathcal{E}(X;\omega)$ in Eq. (3.175b) is defined by replacing all x by X in Eq. (3.176).

Analytical solutions to Eqs. (2.24) and (3.10) can be obtained when both equations are reducible to the normalised Helmholtz equation (2.36). In such cases, both γ_c and γ_t should be independent of location again, i.e. constant in x and X respectively. If γ_c is a constant in x, $R_a(x)C_m(x)\omega, R_a(x)g_l(x), R_a(x)/(r_h(x) + L_h(x)\omega)$ are constants in x because they are linearly independent due to ω. Thus,

$$C_m(x) \propto g_l(x) \propto \frac{1}{R_a(x)}, \tag{3.177a}$$

$$r_h(x) \propto L_h(x) \propto R_a(x). \tag{3.177b}$$

Similarly, if γ_t is a constant in X,

$$C_m(X) \propto g_l(X) = \frac{1}{R_m(X)}, \tag{3.178a}$$

$$r_h(X) \propto L_h(X) \propto R_m(X). \tag{3.178b}$$

In addition, if

$$C_m(x) \propto g_l(x) \propto \frac{1}{(x - x_0)^2 R_a(x)}, \tag{3.179a}$$

$$r_h(x) \propto L_h(x) \propto (x - x_0)^2 R_a(x), \tag{3.179b}$$

where x_0 is an arbitrary constant, Eq. (2.24) is a Cauchy-Euler equation that can be solved analytically. The similar condition for Eq. (3.10) to be a Cauchy-Euler equation leads to a contradiction, because $g_l(X)R_m(X) \propto (X - X_0)^{-2}$ is necessary while by definition $g_l(X)R_m(X) = 1$.

By the finite element method and $N \to +\infty$, Eq. (3.170) does not reduce to Eq. (3.174) given $\mathcal{E}$ being a variable in x. Instead, it reduces to

$$u'' - [\ln \mathcal{E} r]' u' - \frac{2R_a \mathcal{E}}{r} u = 0. \tag{3.180}$$

Analytical solutions can be obtained, if the coefficients in Eq. (3.180) are constants, that is,

$$r(x) \propto [R_a(x)]^{1/2} e^{C_1 x}, \tag{3.181a}$$
$$C_m(x) \propto g_l(x) \propto [R_a(x)]^{-1/2} e^{C_1 x}, \tag{3.181b}$$
$$r_h(x) \propto L_h(x) \propto [R_a(x)]^{1/2} e^{-C_1 x}, \tag{3.181c}$$

where $C_1 \neq 0$ is an arbitary constant. If $C_1 = 0$, electrical parameters are reduced to constants in x. Eq. (3.180) can also be solved analytically if it is a Cauchy-Euler equation, in which cases,

$$r(x) \propto [R_a(x)]^{1/2} (x - x_0)^{C_2+1}, \tag{3.182a}$$
$$C_m(x) \propto g_l(x) \propto [R_a(x)]^{-1/2} (x - x_0)^{C_2-1}, \tag{3.182b}$$
$$r_h(x) \propto L_h(x) \propto [R_a(x)]^{1/2} (x - x_0)^{1-C_2}, \tag{3.182c}$$

where $C_2 \neq 0, x_0$ are arbitrary constants. It is worth noting when $C_2 = 1$, the parabolic taper with homogeneous electrical properties is recovered.

In summary, under the constraints (3.177), (3.178), (3.179), (3.181) and (3.182), the cable equations are reducible to normalised Helmholtz equations and thus the sum-over-trips framework and the method of local point matching can be applied. However, the axial resistivity R_a, the leaky resistivity $R_m = g_l^{-1}$ and the capacitance per area C_m are often assumed to be constants in x (and thus in X), which immediately reduces all the cases under the constraints to those special ones discussed in previous sections.

3.5 Summary

In this chapter, I have investigated membrane potential dynamics on dendritic trees with tapered branches. In §3.2, a single tapered cable is studied. For the six types of taper listed in Table 3.1, the Green's functions can be solved analytically [93], because the cable equations on such tapered dendrites are reducible to the normalised Helmholtz equation (2.36). The cases of non-reducible but realistic tapers are then

discussed, and the Green's functions can be found in terms of Bessel functions.

From §3.3, I have moved onto the study of dendritic trees with tapered branches. If all the branches are of the six types of taper, that is, they are all reducible, the entire dendritic model is shown to be a quantum graph, on which the sum-over-trips framework and the local point matching method introduced in **Chapter 2** can be employed. New rules are derived for such reducible tapers, and the sum-over-trips framework is thus generalised. In §3.4, dendrites with general tapers are investigated. If all the branches are of realistic tapers, the sum-over-trips framework is applicable, whereas the local point matching method is not. Thus, likewise on dendritic branches with general geometric or electrical properties, the finite element method is relatively useful in practice.

Chapter 4

Response Functions on Neuronal Models

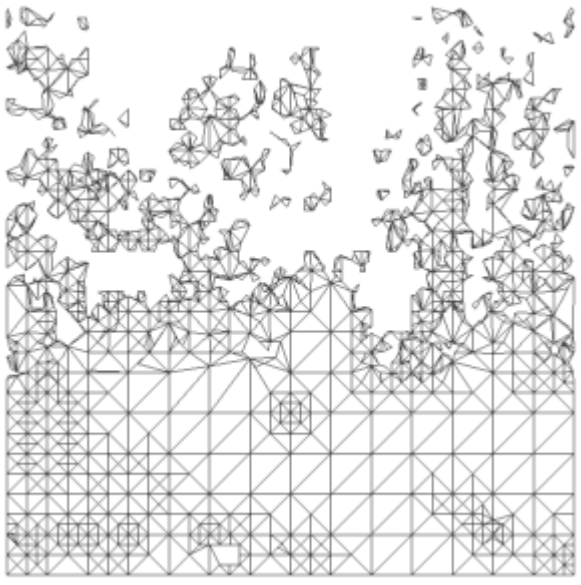

4.1 Introduction

In this chapter, explicit responses on neuronal models with dendritic geometries are studied based on the theoretical discussions in the previous chapters. To start with, the "ball-and-stick" model is studied for the comparison between cylindrical and tapered models in §4.2, and a single neuron with branching dendrites is considered in §4.3 for further investigation into the dendritic geometric effects. Finally, a simplified neuronal network of two neurons coupled by gap junctions is investigated in §4.4.

4.2 Single neuron with single dendritic branch

Here we re-consider the "ball-and-stick" model discussed in §2.4.3 and §3.4.2. This model consists of a lumped soma and one dendritic branch attached to it. The soma is assumed to be located at $x = 0$ and its membrane potential dynamics is described by the boundary conditions (1.39). The branch has a fixed length l_0, and its terminal at $x = l_0$ is closed, which imposes the boundary condition (1.36). A schematic of the model is shown in Fig. 2.6. The dendritic branch is considered to be cylindrical in §2.4.3 and tapered in §3.4.2. The dendritic membrane potential dynamics of the two models are essentially described by resonant cable equations (2.41) and (3.75) respectively. By the method of local point matching, Eqs. (2.92) and (3.155) are constructed for the cylindrical and parabolic models, and their solutions are found in Eqs. (2.93) and (3.156).

4.2.1 Geometric modulation on phase

For comparison between the cylindrical and parabolic models, assume that they share the same electrical parameters, their somata are the same and $r_0 = r_c$. The somatic Green's functions can be found as

$$G_c(0, y; \omega) = \frac{1}{z_c(\omega) \tanh \gamma_c(\omega) l + z_S(\omega)} \frac{\cosh \gamma_c(\omega)(l - y)}{\cosh \gamma_c(\omega) l}, \tag{4.1a}$$

$$G_p(0, y; \omega) = \frac{z_p(0; \omega)}{z_p(y; \omega)} \frac{1}{z_p(0; \omega) - \kappa + z_S(\omega)} \left[\frac{l - y}{l}\right]^{3/2 + 3\gamma_p(\omega)/2\kappa}, \tag{4.1b}$$

where $l_0 = l$ (equivalently $r_1 = 0$) is assumed to simplify the parabolic model. $\gamma_c(\omega), \gamma_p(\omega)$ are defined in (2.32) and (3.11), the characteristic admittance $z_c(\omega), z_p(x; \omega)$ in (2.40) and (3.86) respectively, the somatic admittance $z_S(\omega)$ in (2.57) and κ in (3.154).

In the following two asymptotic cases:

- If the dendritic cable is semi-infinite,

$$\lim_{l\to+\infty} G_p(0,y;\omega) = \lim_{l\to+\infty} G_c(0,y;\omega) = \frac{2\exp(-\gamma_c(\omega)y)}{z_c(\omega)+z_S(\omega)}; \tag{4.2}$$

- If the dendritic cable is infinitesimal,

$$\lim_{l\to 0} G_p(0,0;\omega) = \lim_{l\to 0} G_c(0,0;\omega) = \frac{1}{z_S(\omega)}. \tag{4.3}$$

Both limits can be derived rigorously from Eqs. (4.1). Alternatively, they can be checked in a more heuristic way by geometry. If $l \to +\infty$, the parabola asymptotically becomes a cylinder as $\kappa \to 0$. If $l \to 0$, both models reduce to a point neuron (without any dendrites). It is not surprising that the Green's functions of the two models are reduced to the same one, since the dendritic geometries become identical in these asymptotic cases. In addition, we can see from Eq. (4.2) that the (electrotonic) distance between the input location y and the soma has an exponential effect on the transfer impedance $G(0,y;\omega)$, and that the transfer function (4.2) has a more complicated form than (4.3) in terms of ω. Thus, even an idealised model with a semi-infinite dendritic cable could behave in a way that cannot perfectly mimicked by a point neuron model.

To study the effect of the dendritic geometry for a dendritic length varying in a realistic range, the Green's functions (4.1) are computed numerically. Consider the two models with $l = 100$ and the input is place at $y = 0$. Their somatic input impedances $G(0,0;\omega)$ are compared in Fig. 4.1 (notably the plots of the cylindrical model are shown in Fig. 2.7). It is clear from Fig. 4.1b that both models behave as a band-pass filter with similar spectra. To quantify the resonance more precisely, the resonant frequency $\bar{\Omega}$ is employed. It is defined as the frequency where a Bode magnitude plot is maximised. Mathematically, $\bar{\Omega}$ is found by solving

$$\frac{\partial |G(x,y;i\omega)|}{\partial \omega} = 0, \tag{4.4}$$

for $\omega \geq 0$, or equivalently, the impedance is purely resistive, which gives

$$\Im(G(x,y;i\omega)) = 0, \tag{4.5}$$

where $\Im(x)$ denotes the imaginary part of $x \in \mathbb{C}$. The condition (4.5) is relatively easier to calculate. For example, to find the resonant frequency of a point neuron, we need to solve

$$\Im(z_S^{-1}(\omega)) = 0, \tag{4.6}$$

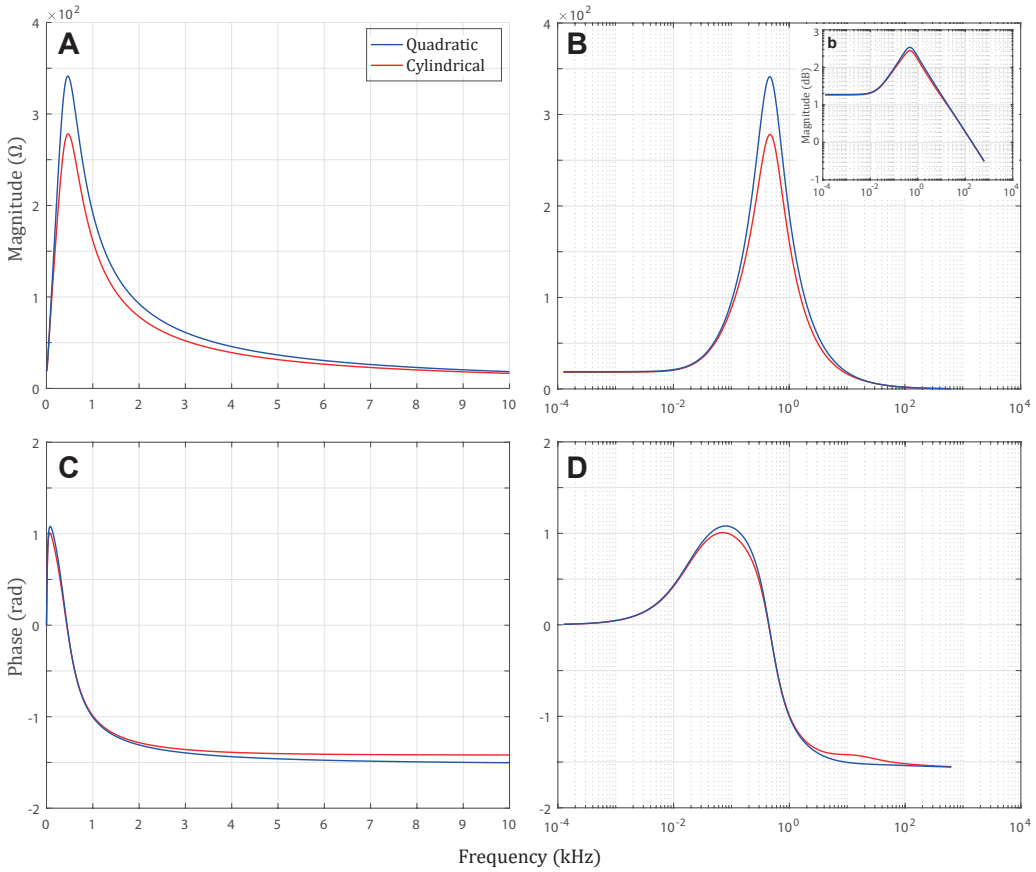

Figure 4.1: The somatic input impedances in the parabolic (blue) and the cylindrical (red) "ball-and-stick" models with resonant membranes. (**A,B,b**): The magnitudes of the the impedances. (**C,D**): The phases of the impedances. The impedance functions (4.1) are complex, because the imaginary frequencies in the Laplace domain (i.e. the real frequencies in the Fourier domain) are employed. Note the horizontal axes (of frequency) of (**B**) and (**D**) are in the logarithmic scale. In addition, (**b**) also plots the same functions as in (**A**) and (**B**), whereas the unit of its vertical axis is decibel (dB), which is by definition logarithmic in the magnitudes. (**b**) and (**D**) are commonly known as the Bode plots in control theory. Geometric parameters: $r_c = 1$ µm for the cylindrical model, $r_0 = 1$ µm and $r_1 = 0$ µm for the parabolic model, and $r_S = 12.5$ µm and $l = 100$ µm for both models. Electrical parameters are the same for both models: $C_m = C_{Soma} = 1$ µF·cm^{-2}, $R_m = R_{Soma} = 2000$ Ω·cm^2, $R_a = 100$ Ω·cm, $r_h = r_{Soma} = 1000$ Ω·cm^2 and $L_h = L_{Soma} = 5$ H·cm^2. Although the neuronal models are simplified in geometry, all the parameters are tuned to be within their realistic ranges.

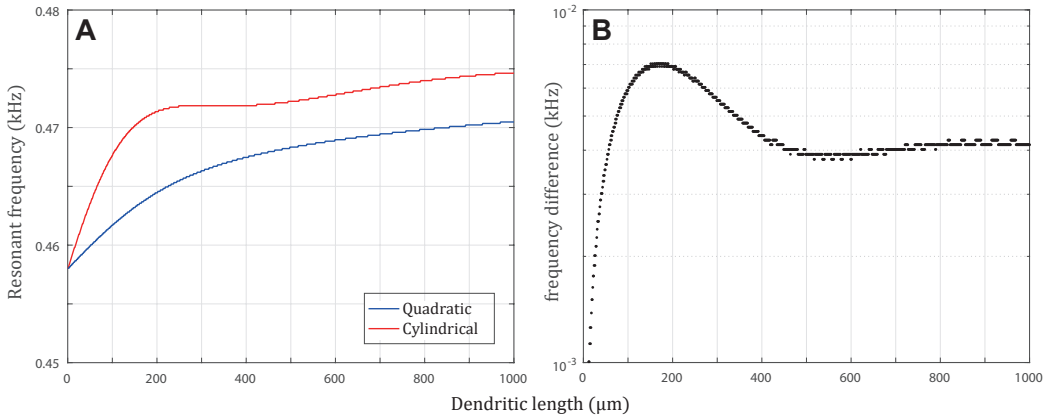

Figure 4.2: Resonant frequency $\bar{\Omega}$ as a function of the dendritic length l. (**A**): Resonant frequencies of the cylindrical (red) and the parabolic (blue) "ball-and-stick" models with resonant membranes. (**B**): The differences of $\bar{\Omega}$ between the two models. All the parameters are the same as in Fig. 4.1, except l which is varying. The value of the resonant frequencies of the two models in the case of $l \to 0$ become identical to that of a point neuron given the same somatic parameters.

which by definition easily reduces to

$$\Im\left(C_S\omega i + \frac{1}{r_S + L_S\omega i}\right) = 0, \tag{4.7}$$

and results in

$$\bar{\Omega} = \sqrt{\frac{1}{C_S L_S} - \frac{r_S^2}{L_S^2}}. \tag{4.8}$$

It is worth noting that, if a neuron is purely passive, it behaves as a low-pass filter and $\bar{\Omega} = 0$. Moreover, if it is resonant, its Bode magnitude plot is always unimodal and $\bar{\Omega} > 0$. More generally, it is proven in [44] that the transfer function on the dendritic cable is a band-pass if a small patch of membrane is a band-pass. In Fig. 4.2, the resonant frequency $\bar{\Omega}$ is plotted as a function of the dendritic length l. It can be seen that the two curves are considerably close when the dendritic length l is small, which implies the two models behave similarly in such cases, as inferred from the limit (4.3). Although the difference between the two curves appear to be finite for large l, the limit (4.2) suggests that their difference vanishes as l increases. Within the realistic range of l, the difference is maximised around $l = 150$ μm.

To see how this difference in the frequency domain determines different behaviours in the time domain, the time profiles of the two somatic responses to the same chirp stimulus is shown in Fig. 4.3A. It can be clearly seen that the two

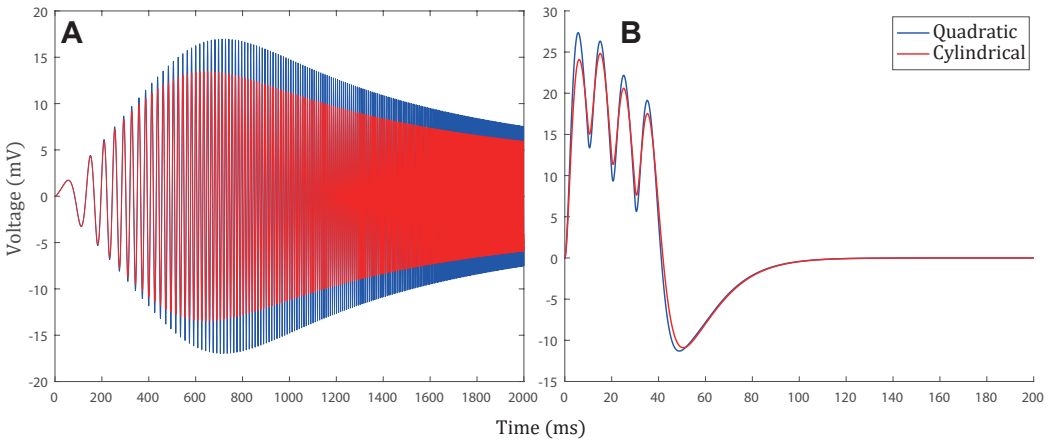

Figure 4.3: The voltage profiles of the somatic responses to somatic inputs of the cylindrical (red) and the parabolic (blue) "ball-and-stick" models with resonant membranes. (**A**): The responses to a chirp input. (**B**): The responses to a train of four idealised EPSCs with successive time gap of 10 ms. Input current parameters: the chirp current is defined by Eq. (1.34) with $A_0 = 0.2$ nA and $\omega_{\text{chirp}} = 0.0003$ kHz, and the EPSC is defined by Eq. (1.32) with $A_0 = 0.2$ nA and $B_0 = 0.1$ kHz. All the other parameters are the same as in Fig. 4.1, except $l = 150$ µm.

oscillating signals clearly reach their peaks at different times. The responses to a more realistic input consisting of succesive EPSCs are shown in Fig. 4.3B. The parabolic model reaches its global maximum at the first peak, while the cylindrical model does so at the second peak. As a result, if an IF model is additionally employed which happens to impose a firing threshold larger than the first peak in the cylindrical model, but smaller than the second one, the firing times of the two models could be different by the time gap between the EPSCs.

Considering the random nature of neuronal systems in reality, the differences in the phases (Fig. 4.1D), the resonant frequencies (Fig. 4.2B) and the times of the signals reaching maxima (Fig. 4.3B) are not be noticeable in many cases. Nonetheless, Fig. 4.1B and 4.3A show clearly that the responses of the two models are different in their amplitudes. In Fig. 4.4A, the somatic responses to single EPSCs applied at the soma are compared for different l. Although the times of the signals reaching the peaks in the two models are indistinguishable, there is a noticeable gap in the peak amplitudes for $l = 150$ µm. It is worth noting that, by moving the input y away from the soma, the difference in the amplitudes of the two models grows rapidly (see Fig. 4.4B). This can also be seen from the Green's functions (4.1), as the impedances decay differently in y, exponentially for the cylindrical model versus polynomially for the parabolic model. The somatic responses of the two models are

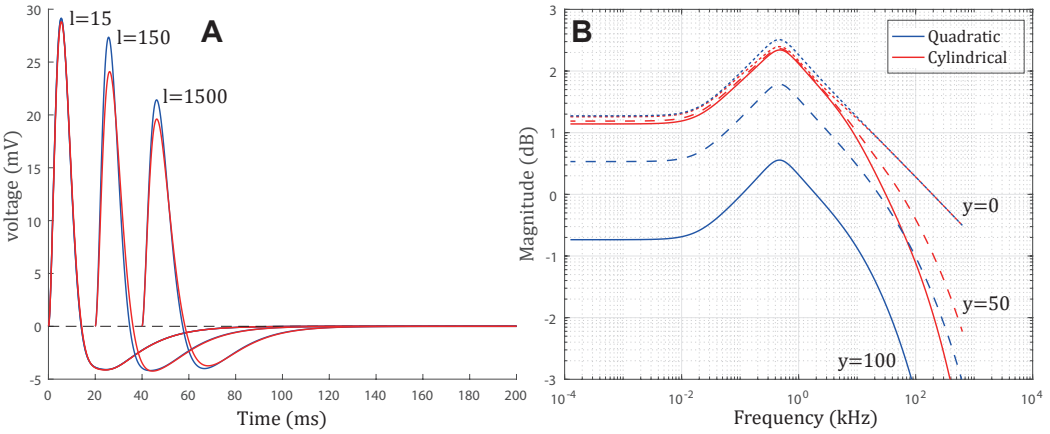

Figure 4.4: The differences in the somatic responses of the cylindrical (red) and the parabolic (blue) "ball-and-stick" models with resonant membranes. (**A**): The voltage profiles due to an EPSC in the models with $l = 15, 150, 1500$ µm, respectively. (**B**): The Bode magnitude plots for the different input locations, $y = 0$ (dotted), 50 (dashed) and 100 (solid) in the model with $l = 150$ µm. All the other parameters are the same as in Fig. 4.3.

extremely distinct for large y. The changes in the resonant frequencies are relatively small, though.

In summary, we have observed minor difference between the resonant behaviors of the cylindrical and parabolic models. This can perhaps be explained by the assumption that they share same electrical parameters. Nonetheless, their difference in voltage amplitude is noticeable. The parabolic model seems to result in larger responses than the cylindrical model, if the same current is injected.

4.2.2 Geometric modulation on amplitude

To conclude the dendritic geometry has a real impact on voltage amplitudes, the above comparison is not convincing enough, because the parabolic model always has a larger area of membrane surface by assuming $r_c = r_0$, which causes more current leakage across the membranes. To eliminate the effect of the membrane surface area, from now on, the areas are assumed to be equal in the two models. In addition, the multi-compartment model discussed in 3.4.2 is considered, because it is both cylindrical (locally) and tapered (globally). The total membrane surface area is also assumed to be the same as the cylindrical and parabolic model by setting dendritic radius (3.158) for each cylindrical compartment. In fact, the multi-compartment model reduces to the cylindrical model with $N = 1$, and $r_c = r_0/3$ in the special

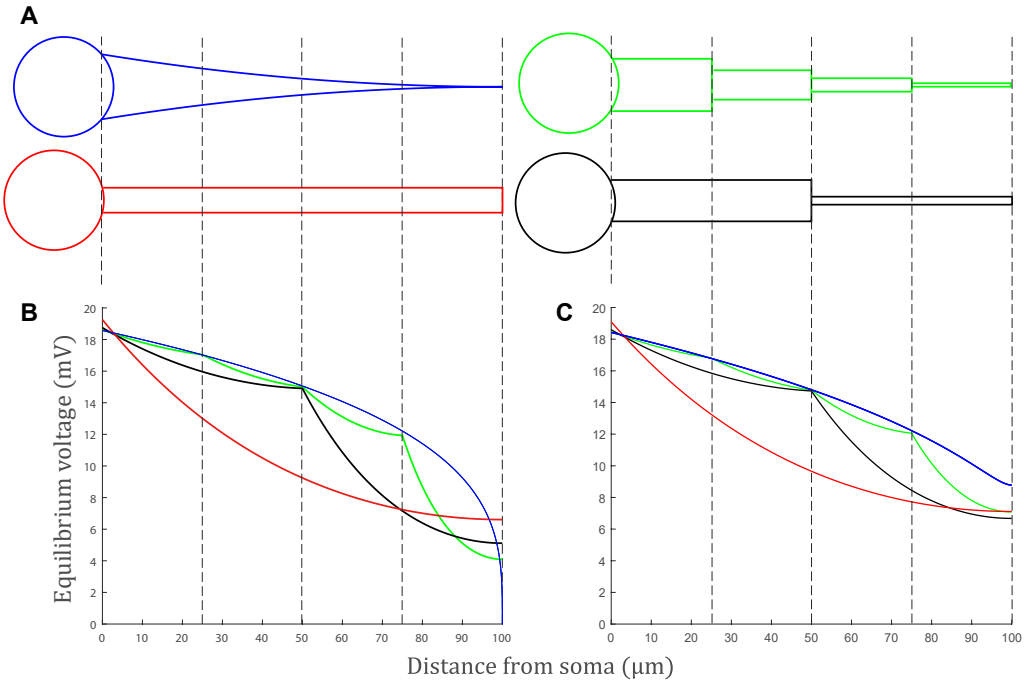

Figure 4.5: (**A**): Schematic shapes of the multi-compartment models with $N = 1$ (red), $N = 2$ (black) and $N = 4$ (green), and the parabolic model (blue) "ball-and-stick" models with passive membranes. (**B,C**): Somatic response at steady state as a function of input location. All the models are purely passive, i.e. $r_h = r_{Soma} \to +\infty$. All the other parameters are the same as in Fig. 4.1 except $R_a = 1000$ Ω·cm. In addition, $r_1 = 0.01$ μm in (**C**).

case of $r_1 = 0$.

Since the difference in resonant behaviours is relatively small, to focus on voltage amplitudes, it is more convenient to study purely passive models injected by the step current input (1.64). The voltage responses at steady state ($t \to +\infty$) can be obtained directly by Eq. (1.66). Fig. 4.5B (similar to Fig. 3.7C) shows the somatic responses at steady state as a function of the input location of the step current. When $N = 1$, there is clearly a large range that the parabolic model yields a higher voltage steady state than the cylindrical model. When $N > 1$, the same phenomena can be observed on each local segment, as the curves of the multi-compartment models are convex piece-wisely on individual compartments. It is also verified that when N is large (e.g. $N = 100$), the multi-compartment model becomes indistinguishable from the parabolic one, whereas the difference is still large on the last compartment (closed to the terminal) as shown in Fig. 3.7C.

In Fig. 4.5B, the voltage of the parabolic model drops to 0 when $y = l$, while that

of the cylindrical model never does (unless $N \to +\infty$). Since $r_1 = 0$ is assumed, the input resistence at the terminal is infinitely large. It is worth noting that, in such models with realistic parameters, the point where the voltage of the parabolic model becomes smaller than that of the cylindrical model always occurs when the dendritic radius is considerably small (at the scale of nanometers in Fig. 4.5B, which is thinner than cell membranes. This is apparently unrealistic and is considered merely a mathematical result. Thus, a more realistic parabolic model with $r_1 = 0.01$ µm (which leads to $l_0 \neq l$) and its corresponding multi-compartment models are considered in Fig. 4.5C. The voltage of the parabolic model exhibits no more drastic slump near the terminal and remains larger than that of the multi-compartment models. However, the noticeable differences between the two models still present with small N, particularly in the region near the terminal.

The result of the relatively large voltage responses on the tapered dendritic branch (or compartments) is consistent with the results in [39, 96]. Cuntz et al. [39] demonstrated by numerical simulations that parabolic dendritic segments would optimise current transfers from distal inputs, and later Bird and Cuntz [96] mathematically proved that this conjecture is valid on a single passive cable that follows parabolic taper. Even though the model cannot match morphologies of all types of neurons, it fits nicely with a stereotypic morphology [96], of which the neurons are known to obey the 3/2 branching rule [76] and to undergo replacement constantly throughout life [98].

voltage attenuation

Another measurement considered for comparison is the voltage attenuation ratio $A_V(y)$. It is defined in [44] as

$$A_V(y;\omega) = \left| \frac{G(0,y;\omega)}{G(y,y;\omega)} \right|. \tag{4.9}$$

Substituting the Green's functions (4.1) and the input impedances

$$G_c(y,y;\omega) = \frac{[1 + (2p_{S,c} - 1)\exp(-2\gamma_c(\omega)y)][1 + \exp(-2\gamma_c(\omega)(l-y))]}{2z_c[1 - (2p_{S,c} - 1)\exp(-2\gamma_c(\omega)l)]}, \tag{4.10a}$$

$$G_p(y,y;\omega) = \frac{(2p_{S,p} - 1)\left(\frac{l-y}{l}\right)^{-3\gamma_p(\omega)/\kappa} + (2p_{\mathrm{C},p} - 1)\left(\frac{y}{l}\right)^{-3\gamma_p(\omega)/\kappa} + 1}{2z_p(y;\omega)}. \tag{4.10b}$$

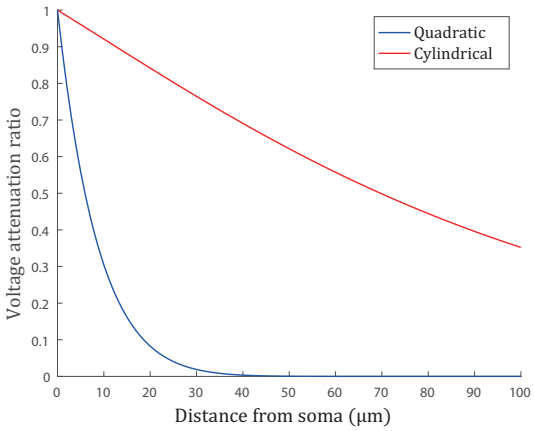

Figure 4.6: Voltage attenuation ratio as a function of input location of the cylindrical (red) and the parabolic (blue) "ball-and-stick" models with passive membranes. All the parameters are the same as in Fig. 4.5B.

into Eq. (4.9), we obtain

$$A_{V,c}(y) = \frac{2p_{S,c}}{\exp(\gamma_c(\omega)y) + (2p_{S,c}-1)\exp(-\gamma_c(\omega)y)}, \tag{4.11}$$

$$A_{V,p}(y) = \frac{2p_{S,p}\left(\frac{l-y}{l}\right)^{3/2+3\gamma_p(\omega)/2\kappa}}{(2p_{S,p}-1)\left(\frac{l-y}{l}\right)^{-3\gamma_p(\omega)/\kappa} + (2p_{\mathrm{C},p}-1)\left(\frac{y}{l}\right)^{-3\gamma_p(\omega)/\kappa} + 1}, \tag{4.12}$$

for the cylindrical and the parabolic models respectively (plotted in Fig. 4.6). For a wide range of input locations ($y > 50$ µm), $A_{V,p}$ stays at almost zero, while $A_{V,c}$ is much larger. Although the result is seemingly opposite to what is observed in Fig. 4.5B, they are consistent with each other. The two results are different, because identical current strength at the input locations is assumed when the somatic response steady states are computed, while identical voltage amplitude is implicitly employed here for the voltage attenuation ratios.

To summarise roughly, for EPSPs of the same size occuring at the same input location in the two models, the somatic response of the cylindrical model is relatively larger, while that of the parabolic model is larger for identical EPSCs. The result is qualitatively consistent with the simulations on neurons with realistic geometries [55]. In addition, recall the input-output reciprocity (2.67) and (3.146), and the responses at different locations to somatic inputs can be easily obtained. If an action potential is fired at a soma of a neuron, the signal is more easily to spread along a cylindrical cable than a tapered one. This could be an explanation for more

tapered branches in dendrites than in axons.

4.3 Single neuron with "Y"-shaped dendritic tree

In this section, I still consider a single neuron, but its dendritic geometry is assumed to form a "Y"-shape (see Fig. 4.7). The dendritic tree consists of one primary dendritic branch and two identical secondary branches. All the branches are generally parabolic in geometry, and thus I call such a neuronal model the parabolic model. For comparison, a cylindrical model is considered, which consists of three cylinders and also forms the "Y"-shape. The sizes of the cylindrers are tuned to guarantee the two models share the same membrane surface area.

In the case when responses are measured at the soma (i.e. $x = 0$), the method of local point matching results in

$$J_a = J_b f(L_0)\alpha_{00}^S + f(0)\alpha_{00}^S, \tag{4.13a}$$

$$J_b = J_a f(L_0)\alpha_{00}^B + f(L_0)\alpha_{00}^B + J_d f(L_1)\alpha_{10}^B + J_e f(L_2)\alpha_{20}^B, \tag{4.13b}$$

$$J_c = J_e = J_a f(L_0)\alpha_{01}^B + f(L_0)\alpha_{01}^B + J_d f(L_1)\alpha_{11}^B + J_f f(L_2)\alpha_{21}^B, \tag{4.13c}$$

$$J_d = J_f = J_c f(L_1)\alpha_{11}^T, \tag{4.13d}$$

where $L_0 = \gamma_0\mu_0(l_0), L_1 = L_2 = \gamma_1\mu_1(l_1)$ are the scaled dendritic lengths. In addition,

$$\alpha_{00}^S = 2p_0^S - 1, \tag{4.14}$$

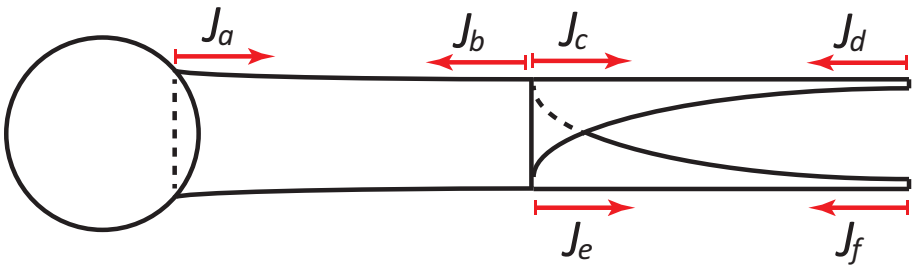

Figure 4.7: A schematic of a neuron with "Y"-shaped dendrites. The primary dendritic branch connects a soma and two identical secondary branches. Both primary and secondary branches are parabolic with geometric parameters: the initial radius r_0, the ending radius r_B and the length l_0 for the primary branch, and similarly r_B, r_1, l_1 for the secondary branch. The terms in Eq. (4.13) are indicated by red arrows.

is the somatic node factor,

$$\alpha_{00}^B = 2p_0^B - 1, \tag{4.15a}$$
$$\alpha_{11}^B = \alpha_{22}^B = 2p_1^B - 1, \tag{4.15b}$$
$$\alpha_{01}^B = \alpha_{02}^B = 2p_1^B \Phi_{01}, \tag{4.15c}$$
$$\alpha_{10}^B = \alpha_{20}^B = 2p_0^B \Phi_{10}, \tag{4.15d}$$
$$\alpha_{21}^B = \alpha_{12}^B = 2p_1^B, \tag{4.15e}$$

are the branching node factors, and

$$\alpha_{11}^T = 2p_1^T - 1, \tag{4.16}$$

is the terminal node factor, where

$$p_0^S = \frac{z_0^S}{z_0^S - \kappa_0 + z_S}, \tag{4.17a}$$
$$p_0^B = \frac{z_0^B}{(z_0^B + \kappa_0) + 2(z_1^B - \kappa_1)}, \tag{4.17b}$$
$$p_1^B = \frac{z_1^B}{(z_0^B + \kappa_0) + 2(z_1^B - \kappa_1)}, \tag{4.17c}$$
$$p_1^T = \frac{z_1^T}{z_1^T + \kappa_1} \tag{4.17d}$$

are the transition probabilities at the soma, the branching node and the closed terminal, and in the end we obtain

$$\Phi_{10} = \Phi_{01}^{-1} = \frac{\phi_0^B}{\phi_1^B}. \tag{4.18}$$

Equivalently, the system (4.13) can be rewritten in the following matrix form,

$$\begin{bmatrix} -1 & f(L_0)\alpha_{00}^S & 0 & 0 \\ f(L_0)\alpha_{00}^B & -1 & 0 & 2f(L_1)\alpha_{10}^B \\ f(L_0)\alpha_{01}^B & 0 & -1 & f(L_1)(\alpha_{11}^B + \alpha_{21}^B) \\ 0 & 0 & f(L_1)\alpha_{11}^T & -1 \end{bmatrix} \begin{bmatrix} J_a + 1 \\ J_b \\ J_c \\ J_d \end{bmatrix} = \begin{bmatrix} -(\alpha_{00}^S + 1) \\ 0 \\ 0 \\ 0 \end{bmatrix}, \tag{4.19}$$

which can be solved by matrix inversion and multiplication, and

$$J_y = \begin{cases} (J_a + 1)f(L_y) + J_b f(L_0 - L_y), & \text{for } 0 \le y \le l_0, \\ J_c f(L_{y-l_0}) + J_d f(L_1 - L_{y-l_0}), & \text{for } l_0 < y \le l_0 + l_1, \end{cases} \tag{4.20}$$

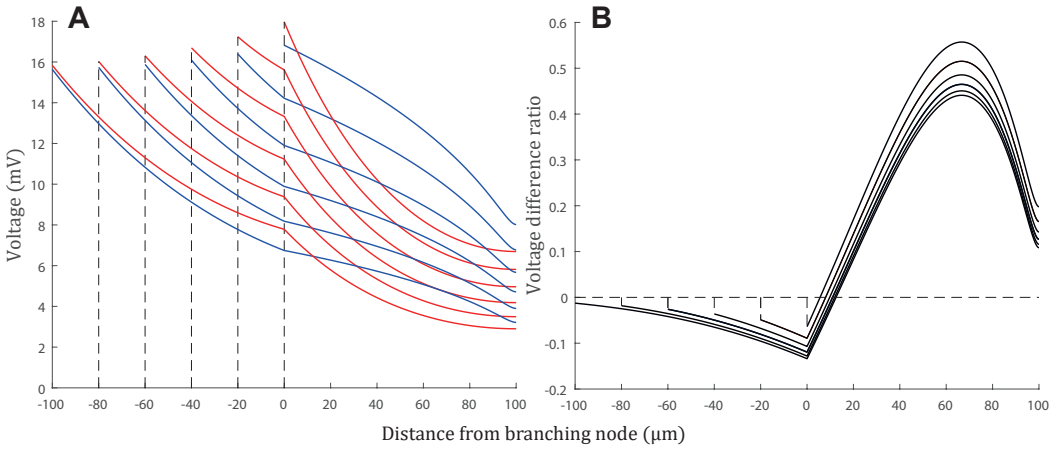

Figure 4.8: Somatic response at steady state as a function of input location on a "Y"-shaped dendritic tree withe passive membranes. (**A**): The somatic responses at steady state of the parabolic (blue) and the cylindrical (red) models with the length of the primary branch $l_0 = 0, 20, 40, 60, 80, 100$ μm. (**B**): The voltage difference ratio ρ_V between the two models. $\rho_V = (V_p - V_c)/V_c$ where V_p and V_c are the somatic responses at steady state of the parabolic model and the cylindrical model respectively. $x = 0$ is placed at the branching node. Other geometric parameters: $r_0 = r_B = 1$ μm and $r_1 = 0.01$ μm, which reduce the primary branch to a cylinder, while both secondary branch are identical to the parabola considered in Fig. 4.5C. The cylindrical model is defined by the relation (3.158). All the electrical parameters are the same as in Fig. 4.5.

where $L_y = \gamma_0\mu_0(y), L_{y-l_0} = \gamma_1\mu_1(y - l_0)$. The Green's functions can thus be obtained in algebraic forms. Notably the above steps to find Green's functions by the generalised sum-over-trips framework also works for the cylindrical model, as I have shown in §3.3.4.

Consider first a case when the primary dendritic branch is cylindrical and the secondary branches are parabolic as in §4.2. (Notably this is still referred to as a parabolic model.) Despite of the dendritic lengths of the primary branch, the voltages are locally larger on the secondary branches in the parabolic model than in the cylindrical one (see Fig. 4.8 for the explicit parameters and results, computed based on the above calculations). Although the somatic responses are changed by varying the global dendritic geometries, the unchanged (secondary) branches are persistent in transmitting signals (the curves are almost the same in their shapes for $y > 0$ in Fig. 4.8B). Next, if the primary branch is parabolic and the secondary branches are cylindrical in the parabolic model, the somatic responses are larger when the inputs are placed on the primary branch, comparing to the cylindrical

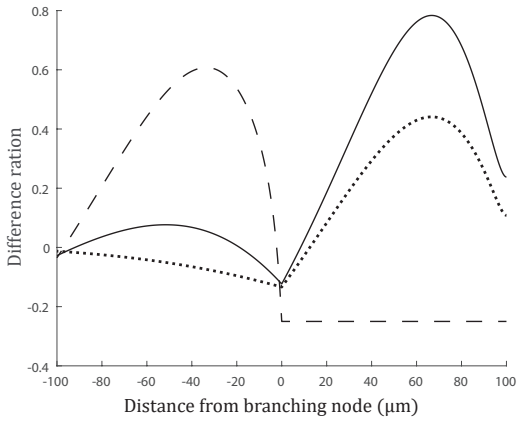

Figure 4.9: The difference ratios ρ_V for $r_B = 0.01$ (dashed), 0.5 (solid),1 (dotted) μm. All the other parameters are the same as in Fig. 4.8.

model (see the dashed curve in Fig. 4.9). Moreover, by fixing the initial and the terminal dendritic radii r_0 and r_1, and varying only r_B in the range between r_0, r_1, the parabolic model transforms continuously from a dendritic geometry of cylinder plus parabolas to parabola plus cylinders. At the same time, the curves of the somatic responses in Fig. 4.9 also transforms accordingly. It is thus reasonable to conclude from all the observations above that, it is a local property for current signals to spread better from distal to proximal location on a parabolic dendritic branch than on a cylindrical one, whereas boundary conditions have some minor effects.

It is worth noting that, with some intermediate value of r_B (e.g. the solid curve in Fig. 4.9), both primary and secondary branches are quite tapered, which leads to larger signals in both branches, comparing to the cylindrical model. Therefore, dendritic tapers can relatively amplify signals from distal regions with the same amount of membranes as cylinders. This suggests that a neuron should always grow tapered dendrites, if its only function is to transmit distal signals to the soma, and its only constraints are the membrane areas. However, not all neurons grow into this stereotypic geometry [96], which implies more complexity in both functions and constraints of dendrites. For those types of neurons whose dendritic morphology fits this geometry (partially if not entirely), they could be more responsible for signal transmission at relatively long distances.

4.4 Two neurons coupled by gap junctions

In this section, a neuronal network of two simplified two neurons coupled by a dendro-dendritic gap junction is considered. Both neurons consist of a soma and N dendritic cylindrical branches. They are connected by a gap junction located at $x_1 = x_2 = l_{GJ}$ away from each soma. This network can receive stimuli in four different locations mimicking distal (y_1 and y_2) and proximal (y_3 and y_4) inputs (see Fig. 4.10).

4.4.1 Two simplified neurons

To start with, consider two identical neurons. If the output is measured at soma 2 where $x_2 = 0$, the method of local point matching constructs the following linear system of algebraic equations for J_a, J_b, J_c and J_d (according to the red arrows in

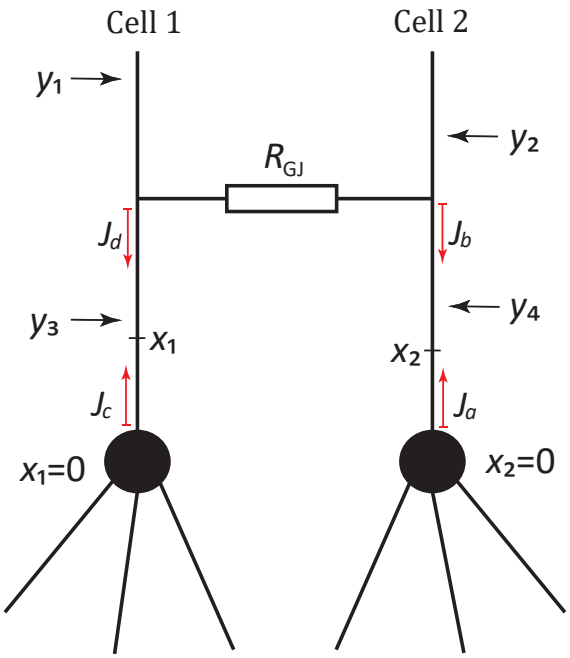

Figure 4.10: A schematic of a simplified network of two neurons coupled by a gap junction. Both neurons consist of a soma and four semi-infinite dendritic cylindrical branches. A gap junction (i.e. an electrical synapse) of conductance $g_{GJ} = R_{GJ}^{-1}$ forms a dendro-dendritic coupling between the two neurons. The terms in Eq. (4.21) are indicated by red arrows.

Fig. 4.10),

$$J_a = J_b f(L_{GJ})(2p_S - 1) + f(X_2)(2p_S - 1), \tag{4.21a}$$
$$J_b = J_c f(L_{GJ})p_{GJ} + J_a f(L_{GJ})(-p_{GJ}) + f(L_{GJ} - X_2)(-p_{GJ}), \tag{4.21b}$$
$$J_c = J_d f(L_{GJ})(2p_S - 1), \tag{4.21c}$$
$$J_d = J_c f(L_{GJ})(-p_{GJ}) + J_a f(L_{GJ})p_{GJ} + f(L_{GJ} - X_2)p_{GJ}, \tag{4.21d}$$

where $X_2 = \gamma_c x_2, L_{GJ} = \gamma_c l_{GJ}$ and γ_c, p_S, p_{GJ} can be found from their definitions (2.32), (2.56) and (2.61). Note that the original sum-over-trips framework on cylindrical dendrites is employed here, since all the dendrites are cylindrical in this section.

Solving the system (4.21) (for details see **Appendix A.1**) leads to the following Green's functions for outputs $x_2 \leq y_4$ on neuron 2,

$$G_2(x_2, y_1) = \frac{1}{2z}\frac{p_{GJ} + p_R}{2p_R + 1} f_*(X_2, Y_1), \tag{4.22a}$$
$$G_2(x_2, y_2) = \frac{1}{2z}\frac{1 - p_{GJ} + p_R}{2p_R + 1} f_*(X_2, Y_2), \tag{4.22b}$$
$$G_2(x_2, y_3) = \frac{1}{2z}\frac{p_{GJ}}{2p_R + 1} f_*(X_2, L_{GJ}) f_*(Y_3, L_{GJ}), \tag{4.22c}$$
$$G_2(x_2, y_4) = \frac{1}{2z}\left[f_*(X_2, Y_4) - \frac{p_{GJ}}{2p_R + 1} f_*(X_2, L_{GJ}) f_*(Y_4, L_{GJ}) \right], \tag{4.22d}$$

where z is defined by Eq. (2.40), $Y_i = \gamma_c y_i$ for $i \in \{1, 2, 3, 4\}$,

$$p_R = (2p_S - 1)p_{GJ} f(2L_{GJ}), \tag{4.23}$$

and a new function

$$f_*(x, y) = f(y)[(2p_S - 1)f(x) + f(-x)] \tag{4.24}$$

is defined to save notations. If $x_2 > y_4$, the first term in the squared bracket in Eq. (4.22d) is $f_*(Y_4, X_2)$ instead of $f_*(X_2, Y_4)$. Since the neurons are identical, the corresponding Green's functions for neuron 1 can be easily obtained from Eq. (4.22) in accordance with the symmetry of the input locations. Note that the Green's functions (4.22a) and (4.22b) are equivalent to the solutions for the Green's functions in the form of an infinite series found by the method of "words" in [20].

If two identical distal inputs are applied at equal distances from each soma (i.e.

$y_1 = y_2 > l_{GJ}$), the somatic Green's functions for both neurons are the same,

$$G_1(0, y_1) + G_1(0, y_2) = G_2(0, y_1) + G_2(0, y_2) = \frac{f_*(0, y_1)}{2z} = \frac{p_S f(y_1)}{z}. \tag{4.25}$$

Similarly, for the case of two identical proximal inputs placed at $y_3 = y_4$,

$$G_1(0, y_3) + G_1(0, y_4) = G_2(0, y_3) + G_2(0, y_4) = \frac{f_*(0, y_3)}{2z} = \frac{p_S f(y_3)}{z}. \tag{4.26}$$

Both solutions are independent of g_{GJ} and l_{GJ} and share the same form as Eq. (4.2) for the model of a single neuron with a single cylindrical dendrite. This result can also be inferred directly from the equivalent cylinders (discussed in §2.4.3).

Consider the case when an input is placed at soma 1 (i.e. $y_3 = 0$). The Bode plots of the somatic Green's functions for both neurons are plotted in Fig. 4.11. Clearly the gap-junctional strength determines the differences between the signal amplitudes at the two somata, while the gap-junctional location has a large impact on the phases. Thus, by stimulating and recording signals at the two somata, the parameters of the gap junction can be inferred.

Now consider a network with the same topology but the biophysical parameters of the two neurons are different. By the same steps as for the previous case, the somatic Green's functions can be calculated: for soma 1,

$$G_1(0, y_1) = \frac{p_{S,1}}{z_1} f(Y_1) \frac{1 - p_{GJ,2} + p_{R,2}}{1 + p_{R_1} + p_{R_2}}, \tag{4.27a}$$

$$G_1(0, y_2) = \frac{p_{S,1}}{z_2} f(L_{GJ,1} + Y_2 - L_{GJ,2}) \frac{p_{GJ,2} + p_{R,2} z_2/z_1}{1 + p_{R_1} + p_{R_2}}, \tag{4.27b}$$

$$G_1(0, y_3) = \frac{p_{S,1}}{z_1} \left[f(Y_3) - \frac{p_{GJ,2}}{1 + p_{R_1} + p_{R_2}} f_{*,1}(Y_3, 2L_{GJ,1}) \right], \tag{4.27c}$$

$$G_1(0, y_4) = \frac{p_{S,1}}{z_2} \frac{p_{GJ,2}}{1 + p_{R_1} + p_{R_2}} f_{*,2}(Y_4, L_{GJ,1} + L_{GJ,2}), \tag{4.27d}$$

and symmetrically for soma 2,

$$G_2(0, y_1) = \frac{p_{S,2}}{z_1} f(L_{GJ,2} + Y_1 - L_{GJ,1}) \frac{p_{GJ,1} + p_{R,1} z_1/z_2}{1 + p_{R_1} + p_{R_2}}, \tag{4.28a}$$

$$G_2(0, y_2) = \frac{p_{S,2}}{z_2} f(Y_2) \frac{1 - p_{GJ,1} + p_{R,1}}{1 + p_{R_1} + p_{R_2}}, \tag{4.28b}$$

$$G_2(0, y_3) = \frac{p_{S,2}}{z_1} \frac{p_{GJ,1}}{1 + p_{R_1} + p_{R_2}} f_{*,1}(Y_3, L_{GJ,1} + L_{GJ,2}), \tag{4.28c}$$

$$G_2(0, y_4) = \frac{p_{S,2}}{z_2} \left[f(Y_4) - \frac{p_{GJ,1}}{1 + p_{R_1} + p_{R_2}} f_{*,2}(Y_4, 2L_{GJ,1}) \right], \tag{4.28d}$$

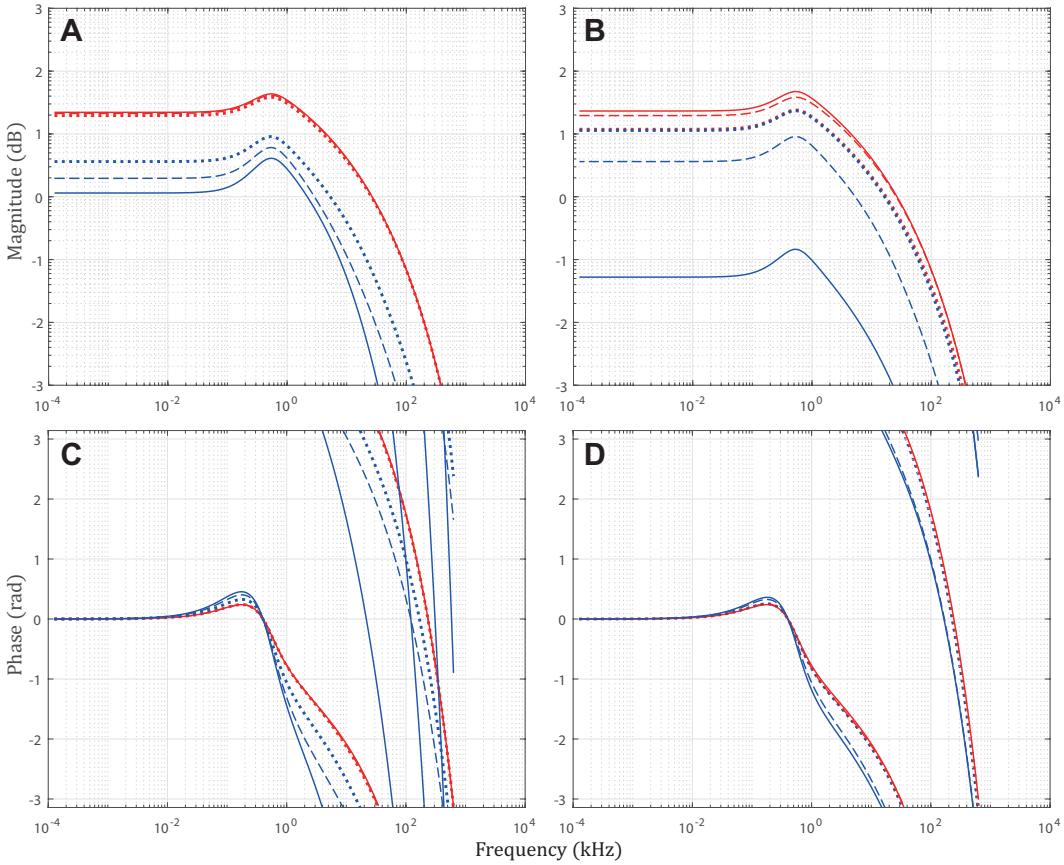

Figure 4.11: Bode plots of transfer impedances at soma 1 (blue) and soma 2 (red) of the simplified neuronal network with resonant membranes. (**A,B**): The Bode magnitude plots. (**C,D**): The Bode phase plots. (**A,C**): The cases of $l_{GJ} = 0$ (dotted), 100 (dashed) and 200 (solid) µm while fixing $R_{GJ} = 100$ MΩ. (**B,D**): The cases of $R_{GJ} = 1$ (dotted), 100 (dashed) and 10000 (solid) MΩ while fixing $l_{GJ} = 100$ µm. The somatic and the dendritic radii and all the electrical parameters are the same as in Fig. 4.1. Note that in many cases the red curves are clashed with each other because the input is always placed at soma 2 (the same location as the output).

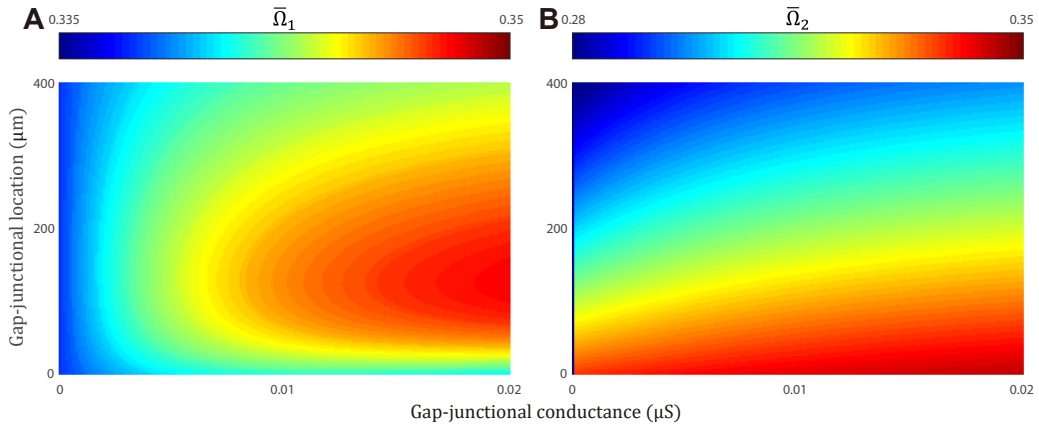

Figure 4.12: Resonant frequency as a function of gap-junctional location l_{GJ} and conductance $g_{GJ} = R_{GJ}^{-1}$. (**A**): The resonant frequency $\bar{\Omega}_1$ at soma 1. (**B**): The resonant frequency $\bar{\Omega}_2$ at soma 2. The input is placed at soma 1. All the parameters of the two somata are the same as in Fig. 4.11. All the dendritic branches are semi-infinite with $r_c = 1$ μm. Their electrical parameters are unchanged from Fig. 4.11, except $r_{h,1} = 100\ \Omega{\cdot}\text{cm}^2$, $r_{h,2} = 10\ \Omega{\cdot}\text{cm}^2$ and $L_{h,1} = L_{h,2} = 50\ \text{H}{\cdot}\text{cm}^2$.

where, for $k \in \{1, 2\}$ indexing the two neurons,

$$Y_i = \gamma_{c,k} y_i, \tag{4.29}$$

$$p_{R,k} = (2p_{S,k} - 1)p_{GJ,3-k} f(2L_{GJ,k}), \tag{4.30}$$

$$f_{*,k}(x, y) = f(y)[(2p_{S,k} - 1)f(x) + f(-x)], \tag{4.31}$$

and $\gamma_{c,k}, z_k, p_{S,k}, p_{GJ,k}, L_{GJ,k}$ are generalised from the previous model (of identical cells) to distinguish the different parameters of the two neurons.

The resonant frequencies $\bar{\Omega}_1$ and $\bar{\Omega}_2$ can then be found by substituting $G_1(0, y_3; \omega)$ and $G_2(0, y_3; \omega)$ where $y_3 = 0$ into Eq. (4.4) for different values of l_{GJ} and $g_{GJ} = R_{GJ}^{-1}$. Thus, a mapping,

$$\mathcal{R} : (l_{GJ}, g_{GJ}) \to (\bar{\Omega}_1, \bar{\Omega}_2), \tag{4.32}$$

can be constructed (see Fig. 4.12). It is straightforward to see that the results are consistent with the observations in Fig. 4.11: the changes in the gap junctional properties have little effect on $\bar{\Omega}_1$ (Fig. 4.12A), and only the location of the gap junction plays a more influential role than its strength in modulating $\bar{\Omega}_2$ (Fig. 4.12B). The persistency in $\bar{\Omega}_1$ is probably due to the experimental design that both the input and the output are located at soma 1.

Often it is difficult to measure experimentally locations and strengths of gap

junctions in real neuronal networks. Knowledge of the inverse mapping

$$\mathcal{R}^{-1} : (\bar{\Omega}_1, \bar{\Omega}_2) \to (l_{GJ}, g_{GJ}) \tag{4.33}$$

from a pair of resonant frequencies (obtained from somatic sub-threshold stimulations) might provide estimates for gap-junctional parameters. The mapping $\mathcal{R}$ is neither surjective nor injective (see Fig. 4.12A), and thus $\mathcal{R}^{-1}$ is not mathematically well defined. Nonetheless, Fig. 4.12B suggests the gap junctional strength may have little effects on the system, so it might be more important to measure the location. Once the location is estimated, this may lead to a one-to-one correspondence between (l_{GJ}, g_{GJ}) and $(\bar{\Omega}_1, \bar{\Omega}_2)$, if the experimental technique could measure the resonant frequencies accurately enough.

4.4.2 Two tufted neurons

Now consider a more realistic neuronal network consisting of two identical tufted or mitral cells. Each neuron has one primary dendritic branch, which branches at its end and forms a tuft. The two cells are coupled in their tufts by dendro-dendritic gap junctions (see Fig. 4.13A). Although it is possible to apply the method of local point matching to find the Green's functions for this tufted network, it is more convenient to perform first the model reduction with equivalent cylinders (discussed in §2.4.3), and the reduced network topology is shown in Fig. 4.13B. Notably, after model reduction, a tufted neuron becomes a "Y"-shaped neuron studied in §4.3.

To be specific, if the input and output are not located in the tufts, the tufted branches for each neuron can be merged into two equivalent cylinders, with an equivalent gap junction located on one of them, or explicitly,

$$z^*_{T,GJ} = N_{GJ} z_T, \tag{4.34a}$$

$$R^*_{GJ} = R_{GJ}/N_{GJ}, \tag{4.34b}$$

where $z_T, z^*_{T,GJ}$ are the characteristic admittances of the individual tufted branches, and R_{GJ}, R^*_{GJ} are the gap-junctional resistances. The superscript $*$ in this section denotes the equivalent reduced model. The Green's functions obtained under the conditions (4.34) are identical for the two models, that is,

$$G(x_0, y_k) = G^*(x_0, y_2). \tag{4.35}$$

If the input is in the tuft but the output is not, it is easy to check that the constraints (4.34) would give the same J_y. However, Green's functions are dependent on the

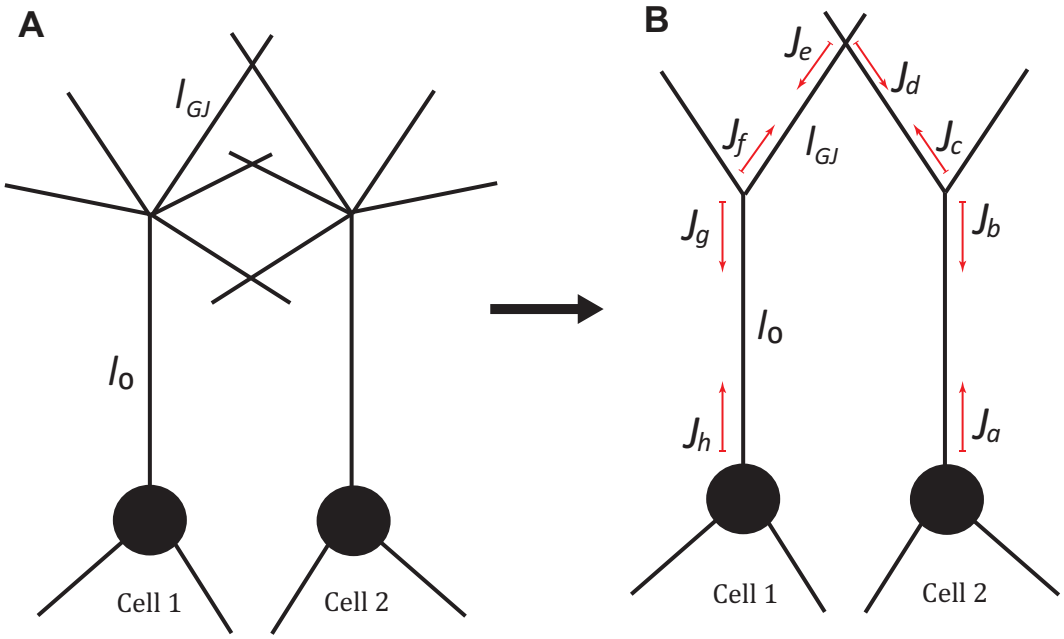

Figure 4.13: (**A**): A schematic of a simplified network of two neurons coupled by gap junctions in their tufts. Each neuron has N dendritic branches attached to its soma ($x = 0$). One of the N branches is the primary dendrite, which branches at the end ($x = l_0$) and forms a tuft. The other branches attached to the somata and the secondary branches in the tufts are semi-infinite. Each tuft has N_T branches, and N_{GJ} of them form dendro-dendritic gap junctions (one on each). All the gap junctions are identical in strength g_{GJ} and located at $x = l_{GJ} + l_0$. (**B**): An equivalent reduced model to (**A**). Everything outside the tufts are unchanged from (**A**). Either tuft consists of only two branches, one of which forms a gap junction to the other tuft. The gap junction still locates at l_{GJ}, whereas its strength $g^*_{GJ} = N_{GJ} g_{GJ}$. The arrows denote the terms in Eqs. (A.8) according to the local point matching method.

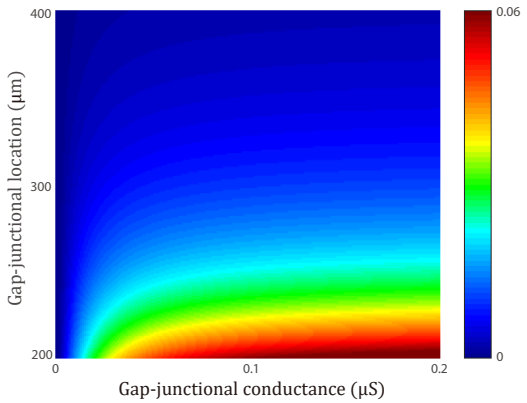

Figure 4.14: Coupling ratio as a function of gap-junctional location $l_{GJ} \geq l_0$ and conductance $g_{GJ} = R_{GJ}^{-1}$. The two neurons are passive and identical. Their geometries are shown in Fig. 4.13, with the primary dendritic branch of length $l_0 = 200$ µm, and their passive electrical parameters are the same as in Fig. 4.11.

$z_j(y)$ at the input location due to Eq. (2.83), which leads to

$$G(x_0, y_k) = \frac{1}{N_T - N_{GJ}} G^*(x_0, y_1), \tag{4.36}$$

if the input at y_k is applied to the branch without a gap junction, and

$$G(x_0, y_k) = \frac{1}{N_{GJ}} G^*(x_0, y_2), \tag{4.37}$$

if the input at y_k is applied to the branch with a gap junction. Here the reduced model is constructed so that the stimuli in the full and reduced models are placed at the same location, i.e. $y_1 = y_k$ and $y_2 = y_k$. The point $x_0 < l_0$ is located on the primary dendritic branch of either of the neurons. If the output is in the tufts but the input is not, the input-output reciprocity (2.67) can be employed. If both input and output are in the tufts, the symmetry among the branches in the tufts is broken, and thus the model reduction fails.

After obtaining the Green's functions by the method of local point matching on the reduced model, those on the full model can be easily found by Eqs. (4.35) - (4.37) (explicit expressions and deductions omitted here, details to be found in **Appendix A.2**). To investigate the effect of gap junctions in the tufts, the coupling ratio (CR) between the two neurons are shown in Fig. 4.14, where CR is defined in [99] as

$$\text{CR} = \frac{\max_t \mathcal{L}^{-1}\{G_2(0,0;\omega)\}(t)}{\max_t \mathcal{L}^{-1}\{G_1(0,0;\omega)\}(t)}. \tag{4.38}$$

Although increasing g_{GJ} strengthens the coupling (as expected), l_{GJ} actually plays an even more important role. Comparing to the results in Fig. 4.12, the domination of l_{GJ} over the system occurs for relatively large g_{GJ}. Nonetheless, all the observations in this section suggest that gap-junctional location has stronger impact than gap-junctional strength on voltage spreading between the coupled neurons.

4.5 Summary

In this chapter, I have computed the numerical results on neuronal models with different dendritic geometries. Firstly, a single neuron with a single dendritic branch is investigated in §4.2. By defining the resonant frequency to quantify the resonant behaviours of the neuronal systems, it is found that different geometry of a single branch (tapered or cylindrical) has little impact on signal modulation. However, a tapered dendrite is better at current transfer from its distal (thinner) end to the proximal (thicker) end. This effect is found to be a local property of tapered dendrites in §4.3, by investigating a single neuron with a "Y"-shaped dendritic tree and varying the geometries of the primary and the secondary dendritic branches.

Secondly, a simplified neuronal network of two gap junctional coupled neurons is considerd in §4.4. Mimicking a realistic experimental protocal, injecting currents and recording responses at the two somata, the relationship between the gap junctional properties and the output measurements can be computed. This procedure can be used to assist the estimation of gap junctional parameters. The numerical results suggest that the location of the gap junction has a noticeable effect on the signal transmission between the coupled neurons, whereas little impact is seen on the resonant behaviours. The strong modulation on voltage attenuation by gap junctional location, i.e. the distance between the gap junction and the soma, is also observed in a more realistic model consisting of tufted neurons.

Chapter 5

Conclusion

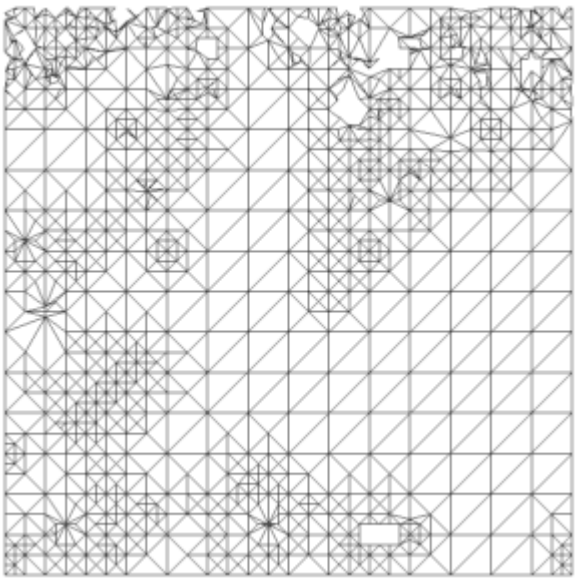

5.1 Results and discussion

In this thesis, I have thoroughly studied linear dendritic cable theory, which provides a methodological framework and empirical insights into neuronal signal modulation by dendritic geometry. Due to the complex morphologies of neuronal dendrites, it is non-trivial to find the input-output relationship analytically, even though the model of dendritic membrane potential dynamics is simplified and all cable equations are assumed to be linear. As all the cable equations on cylindrical dendrites can be reduced to the normalised Helmholtz equation, the dendritic membrane potential dynamics on an arbitrary dendritic geometry can be formally modelled as a quantum graph. To solve for analytical solutions to the dynamics, the sum-over-trips framework and the local point matching method are studied in detail.

5.1.1 Implications and limitations of methods

The sum-over-trips framework is essentially a reformulation of the path integral, and is applicable to any quantum graphs. In fact, the term "quantum graph" is borrowed from other physical disciplines, e.g. photonic crystals. It can be employed as a simplified model to describe signal propagation through a quasi-one-dimensional system [62, 63]. The framework constructs analytical Green's functions essentially by encoding transition probablities along random paths according to graph topologies. Solutions can thus be found in more structured expressions than by the path integral formulation direction. Theoretical analysis, e.g. spectral analysis, can be conducted more easily. General properties, e.g. the reciprocity identity, can be shown by the framework without any specific geometry.

However, the computational convergence by the sum-over-trips framework is highly dependent on graph topology. Perhaps the convergence is well-behaved in crystals, of which the structure is highly ordered as the binary tree in Fig. 2.4, and even analytical solutions can be found as for the the nerve ring and the array of neurons (see §2.4.3). Dendritic morphologies of real neurons are much less ordered, and the convergence can be relatively ill-behaved or at least computationally expensive as shown on realistic digital reconstructions in Fig. 2.4. This problem can be overcome by the novel method of local point matching, if the dynamics can be described by a Helmholtz equation. The method results in analytical Green's functions in closed algebraic forms, instead of infinite sums by directly employing the sum-over-trips framework. The problem in practice is again due to the heterogeneous geometrical and electrical properties of real neurons, whereas some theoretical analysis is still possible given appropriate assumptions (see 5.1.3).

The main limitation of the framework roots in the mathematical modelling of the dendritic membrane potential dynamics. The model is by assumption linear, but real neurons can behave non-linearly, e.g. firing action potentials. I will discuss spiking models in §5.1.4, and additionally non-linear interactions between synaptic inputs in §5.1.5. The linear assumption is valid when sub-threshold membrane potential dynamics by single (or non-interactive) inputs is considered. If the assumption can be justified, the framework is powerful as Green's functions in closed algebraic forms permit not only more straightforward mathematical analysis, but also accurate and cheap numerical computations. The input can even be modelled as a random process, in particular, a Poisson process or a white noise. Stochastic cable theory [49] proves the (deterministic) Green's function $G(x, y; t)$ on a neuronal cable will be the mean behaviour of the stochastic Green's function, and its variance can be found in terms of $G^2(x, y; t)$. It is straightforward to note that the sum-over-trips framework is perfectly and straightforwardly compatible with the theory.

5.1.2 Cylindrical versus tapered dendritic branches

To investigate the differences in signal transmission between cylindrical and tapered dendrites, morphologically simplified but representative neuronal models are studied in **Chapter 4**. All neurons behave as band-pass filters if their membranes are resonant. Dendritic geometries affect the signal amplitudes and phases. Although the geometric modulation on signal phases is small, the modulation on amplitudes is noticeable. Locally on a dendritic branch, distal current signals are amplified in a tapered structure, comparing to a cylindrical structure with the same membrane area. This is probably due to the large input impedance at tapered ends of dendrites. Distal signals propagated along tapered dendrites are more reliable, and thus perhaps it it metabolically cheaper for a neuron to grow tapered dendrites, if it is more responsible for such uni-directional signal transmissions.

Computational models with compartmental cylinders can provide relatively good approximations at relatively thick ends of dendrites (comparing to primary dendrites). However, the differences at such tapered ends cannot be ignored, even if the individual compartments are quite small. One would expect smaller errors if the input impedances are close in corresponding continuous and discretised models. Thus, it might be reasonable to discretise continous models more finely near input locations.

5.1.3 Non-uniform distribution of h-channels

The I_h currents are produced by h-channels. The channels are assumed to be uniformly distributed on cell membranes throughout this thesis. However, the densities of h-channels are known to increase noticeably along the branches from the soma in some pyramidal cells [9–11]. Williams and Stuart [12] found such increases to be linear and Poolos et al. [14] also employed linear models in simulations to elaborate the experimental results, whereas Kole et al. [15] showed such increases to be exponential. Since I_h currents prevent membranes from too large hyperpolarisation, it seems reasonable for them to be distributed more densely near locations where synapses aggregate, rather than uniformly everywhere. In terms of modelling, the h-channels are the most important in determining signal phases, as electric energy is transformed into magnetic energy stored in inductors and later released from time to time.

Assume all the individual h-channels are identical, and that they are linearly distributed along a cylindrical cable for $x \geq 0$ where a soma (or a closed terminal) is at $x = 0$. We can follow the discussion in the last section of §3.4.2, and rewrite Eq. (3.175a) as

$$\mathcal{E}(x;\omega) = C_m\omega + g_l + \frac{x - x_0}{1/\rho_g + \omega/\rho_p}, \tag{5.1}$$

where $x_0 \leq 0$ and $\rho_g, \rho_p > 0$ are constants defined by $g_h = r_h^{-1} = \rho_g(x - x_0), p_h = L_h^{-1} = \rho_p(x - x_0)$. The resonant cable equation (2.24) is thus reduced to

$$-\frac{\partial^2 V}{\partial x^2} + \frac{2R_a}{r_c}\left[\mathcal{E}(0;\omega) + \frac{x}{1/\rho_g + \omega/\rho_p}\right] V = \frac{I_0(x;\omega)}{C_m D}, \tag{5.2}$$

which can be further recast into the canonical form of the Airy equation by scaling x. The Green's functions can thus be obtained in terms of elementary and Airy functions [100]. Notably solutions to Eq. (3.148) for non-reducible dendritic tapers can be expressed in the forms of Bessel functions, and Bessel functions and Airy functions are deeply related to each other [101]. It seems possible to investigate and analyse these realistic but not reducible general cable equations (3.148) and (5.2) together as a class. However, both cases are not likely to be compatible with the sum-over-trips framework as the differential operators are not likely to be identical on different dendritic branches (since heterogenous geometric and electrical properties are considered).

Furthermore, it will be interesting to study non-uniformly distributed h-channels on a tapered dendritic branch. For example, h-channels are more densely distributed at the distal region of a tapered branch of a pyramidal cell. It is plausible to see

from the model that the tapered geometry would amplify distal synaptic signals while h-channels modulate them, making the dynamics flattened and slower. This might eventually encourage interactions between synapses, which is in general non-linear (see §5.1.5).

5.1.4 Spiking neurons

Under resting conditions, a typical neuron is polarised at a membrane potential of around -70 mV. If its membrane potential rises above a threshold level (about -55 to -50 mV), it fires an action potential [43]. The dynamics of an action potential can be elaborated by non-linear conductance-based models, e.g. the Hodgkin-Huxley model [42]. Alternatively, it is also reasonable to model the sub-threshold dynamics and the firing behaviours separately, as the change in voltage is so rapid during a short time. Since this thesis mainly finds Green's functions by assuming linear(ised) neuronal membrane dynamics, the second approach (to model the firing behaviours separately) can be easily incorporated into the framework. To be specific, Integrate-and-Fire (IF) models can be employed. Such models describe the two states of a neuron, firing and resting, independently by specifying the threshold voltage V_{th}. When the membrane potential eventually "integrates" to V_{th}, it "fires" a spike and resets its value to V_{re}. Although IF models are mathematical idealisations and thus lack biological details, they are useful because they are analytically solvable, even in cases of stochastic inputs, and therefore they have been widely used in analysis of emergent properties of neuronal circuits [43, 102].

To start with, consider a point neuron. The sub-threshold behavior of a leaky IF model is determined simply by the passive membrane (1.1) and the leakage current (1.3), that is,

$$\tau_m \frac{dV}{dt} = E_l - V + \frac{I_0}{g_l}, \tag{5.3}$$

where

$$\tau_m = \frac{C_m}{g_l}. \tag{5.4}$$

In addition, once $V \geq V_{\text{th}}$, a spike is assumed to be generated and V is immediately reset to V_{re}. It is worth noting the changes in V during a spike is not modelled, as the duration of a spike is considered extremely short. For any constant input current I_0, Eq. (5.3) permits a fixed point $V = E_0$ where $E_0 = E_l + I_0/g_l$. If $E_0 < V_{\text{th}}$, the neuron is depolarised to a new equilibrium E_0. If $E_0 \geq V_{\text{th}}$, its membrane potential keeps increasing towards E_0 but always reaches the threshold and then resets first, that is, the neuron fires periodically. Without loss of generality, choose $V(0) = V_{\text{re}}$

and the solution to Eq. (5.3) can be found as

$$V(t) = E_0 + (V_{\text{re}} - E_0)e^{-t/\tau_m}. \tag{5.5}$$

$V(T) = V_{\text{th}}$ then gives the duration T for the potential to reach the threshold, explicitly,

$$T = \tau_m \ln\left(\frac{E_0 - V_{\text{re}}}{E_0 - V_{\text{th}}}\right). \tag{5.6}$$

Since T is the period of firing, the firing rate can be easily found as T^{-1}.

To make the model more realistic, an additional function for the spiking regime can be considered instead of the instant reset, while the sub-threshold regime described by Eq. (5.3) is unchanged. Explicitly, the function can be defined as

$$V(t) = h_s(t - t_s^i), \tag{5.7}$$

for $t \in (t_s^i + T_s]$ and any $i \in \{1, 2, 3, \dots\}$, where t_s^i is the time when the i-th spike is initiated and T_s is the duration of a spike. In addition, $h_s(0) = V_{\text{th}}$ and $h_s(T_s) = V_{\text{re}}$. Thus, when $V < V_{\text{th}}$ the membrane potential in this extended model is described by Eq. (5.3), but once it reaches the threshold it follows Eq. (5.7) until the spiking regime ends (after T_s). It is straightforward to see that the original leaky IF model with the instant reset can be recovered by the new model with the limit $T_s \to 0$. The new model has a period of $T + T_s$, which gives a firing rate of $(T + T_s)^{-1}$. The definition of h_s becomes really important and useful when neurons with morphologies are considered. For example, Schwemmer and Lewis [103] considered a "ball-and-stick" model, and only the soma is excitable, that is, if the somatic membrane potential reaches the threshold, it starts to vary as Eq. (5.7) specifies. If the voltage is reset instantly, i.e. $T_s \to 0$, the somatic membrane potential is discontinuous in t at the spiking times t_s^i. However, there is always a boundary condition at the location where the soma and the dendrites are attached together that requires the somatic and the dendritic membrane potentials to be equal (i.e. the continuity of membrane potentials, see §1.2.4). A contradiction arises because the dendritic potential is continuous in t (even at t_s^i). Since Green's functions are found by the sum-over-trips framework, it is simple to compute responses given any inputs. It is then trivial to check for the soma whether or not their membrane potentials are above the threshold. If so, it fires a spike, which can be treated as injecting a somatic input current. The entire voltage response profiles after the occurrance of spiking events are thus recursively updated. Such a simulation procedure saves computational cost, because given the fixed time window of voltage profile it only

needs to be updated as many as the number of spiking events, comparing to any numerical simulation that updates every time steps.

Another example is to model dendritic spines as IF active points. Dendritic spines are extensions on dendrites that connect post-synaptic neurons to axons of pre-synaptic neurons. Many chemical synapses can be found on the head of them, and thus they are closely related to spikes. Spine heads are excitable and can thus be modelled by IF active points [79] (as the soma in the last example), whereas Hodgkin-Huxley models are also applicable [104]. Spine necks can be simply modelled as passive resistors. Assuming spines distributed in a discrete and uniform density along a dendritic branch, we obtain the Spike-Diffuse-Spike (SDS) models [79–82]. Comparing to brutal-force simulations, solving for Green's functions between two such spines first allows one to repetitively add the responses directly into the entire system whenever the voltage of any spine reaches the IF threshold.

In addition, since the Fire-Diffuse-Fire (FDF) models for intra-cellular calcium releases and waves [83, 84] are similar to the SDS models in their mathematical expressions, the approaches taken in this thesis can be also employed for the FDF models [85]. IF active points can also be added onto the model of the nerve ring discussed in §2.4.3. Such a theoretical model can assist experimentalists understanding nerve rings in jellyfishes *Polyorchis* and *Aglantha*, their central nervous systems, because these creatures are small in size and it is difficult to obtain intra-cellular recordings from their neurons [77, 78].

5.1.5 Synaptic activities

Synapses are essential because they are the means by which neurons transmit signals from one to another. They mainly connect axons to dendrites, whereas there are many exceptions, e.g. dendro-dendritic synapses [105–108] and axo-axonic synapses [106, 109]. Depending on whether or not biochemical processes are involved, they can be classified into two fundamentally different types, chemical and electrical. Electrical synapses (gap junctions) are included in the sum-over-trips framework as boundary conditions, because they permit direct ion flows between coupled cells, and are thus simply modelled as purely passive resistors. No biochemical processes are involved, and thus signal transmission by gap junctions is metabolically inexpensive.

It is observed in §4.4 that the gap junctional strength modulates signal amplitudes but has little effect on signal phases. The result is trivial because the gap junction plays the role of a resistor in the electrical circuit. The gap junctional location significantly modulates both amplitudes and phases of signals. However, the location of gap junction is in fact a geometric measurement of the dendritic

branches on which the gap junction is located, and the dendritic branches are resonant. Hence, computational results of the theoretical model could assist parameter estimation of gap junctions, given the knowledge of the dendritic geometric and electrial measurements; it is difficult to accurately measure the parameters of gap junctions in experiments due to their small sizes, but relatively easy to stimulate and record at somata.

Synaptic interactions

At a chemical synapse, the pre-synaptic neuron releases neurotransmitters (typically due to a spike) from synaptic vesicles into the synaptic cleft. The neurotransimitters can diffuse to the opposite side of the cleft, and if they bound to the corresponding ligand-gated channels of the post-synaptic cell, generation of post-synaptic currents could be triggered as these channels would change their conductances. At the same time, it is clear from Eq. (1.8) that the total membrane conductance is voltage dependent. Therefore, any post-synaptic current is also dependent on the temporal membrane potential at its location, which implies the interactions between synaptic inputs are inevitable. Such non-linear synaptic interactions on dendrites were discovered for a long time [64]. However, due to the model choice, Green's functions found by our method always admit the additivity of multiple inputs (1.53), which can hardly be justified when multiple inputs are presented. Hence, Eq. (1.32) is only an idealised model of EPSC in the case of no shunting currents that would have varied the membrane conductance are presented. This model can be useful for experiments investigating single neurons *in vitro*, though.

Considering shunting currents on an infinite cable, a more realistic model [110] for the post-synaptic current is

$$I_0(x;t) = w(x;V)(E_0 - V), \tag{5.8}$$

where $w(x;V)$ is membrane conductance at x, and E_0 is the effective membrane reversal potential determined by all the ion channels. Since $w(x;V)$ is voltage dependent, the input current $I_0(x;t)$ becomes non-linear (in V). Although the system is no long a LTI system, the membrane potentials can still be written down in terms of a Green's function:

$$V(x;t) = \int_0^t \int_{-\infty}^{\infty} G(x,y;t,s) I_0(y;s) dyds + \int_{-\infty}^{\infty} G(x,y;t,0) V(y;0) dy. \tag{5.9}$$

Notably the concept of Green's function is here extended from a simple tool for

solving linear differential equations to a general object quatifying the relationship between input and output. It can be shown that the Green's function $G(x, y; t, 0)$ is linear in space but non-linear in time, which leads to

$$G(x, y; t, s) = G(x - z_1; t, t_{N-1}) * G(z_1 - z_2; t_{N-1}, t_{N-2}) * \cdots * G(z_1 - y; t_1, s), \quad (5.10)$$

by the convolutional property (1.49), for $s = t_0 < t_1 < \cdots < t_{N-1} < t_N = t$. If the time steps $|t_n - t_{n-1}|, n \in \{1, 2, 3, \ldots, N\}$ are small enough, the non-linear Green's function $G(z_n - z_{n-1}; t_n, t_{n-1})$ is tiny, and can thus be approximated in terms of the linear $G(z_n - z_{n-1}; t_n - t_{n-1})$. Assuming this linear approximation works for all n and taking the limit $N \to +\infty$, Bressloff and Coombes [110] showed

$$G(x, y; t, s) = e^{-\int_s^t w(t')dt'} G(x - y; t - s), \quad (5.11)$$

where $G(x-y; t-s)$ is the Green's function for the model without shunting currents. Noticing the similarities between the proof in [110] and the deduction of the original sum-over-trips in [18], we should expect this result to be compatible with the sum-over-trips framework. Hence, synaptic interactions by shunting currents can be studied on dendritic trees by the same approach taken in this thesis.

To consider a typical neuron *in vivo*, that could have several thousand synapses, and constantly receive numerous synaptic inputs, background synaptic noise of this neuron has to be taken into account. Bressloff and Coombes [110] shows it is possible to determine the effects of such noise on this neuron *in vivo*, by experimental investigation of the neuron *in vitro*. Green's functions still play a role in the results, but more assumptions and techniques beyond the scope of this thesis are employed. A cost must be paid, if one attempts to understand the behaviours of single neurons in the context of a large network.

Synaptic plasticity

Another significant feature of synapses is synaptic plasticity, that is, the strength of a synapse can vary based on its activities. Synaptic plasticity is believed to be one of the most basic adaptation processes occuring in nervous systems, that ultimately enables learning behaviours of any creature with a nervous system [43]. Hebbian theory [111] offers the most famous explanation for synaptic plasticity, which is often summarised roughly as *"cells that fire together wire together"*. The idea is also widely employed in artifical neural networks, e.g. the Hopfield model [112].

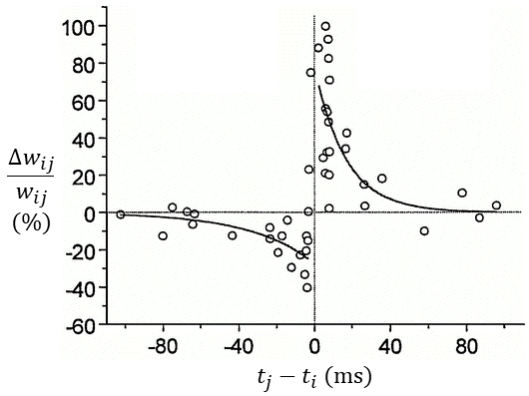

Figure 5.1: Spike-timing dependent plasticity: the normalised change of synaptic strength as a function of the timing difference between the pre- and post-synaptic spikes, where w_{ij} is the synaptic strength between neuron i, j, Δw_{ij} is its change, and t_i and t_j are the spiking times of the two cells, respectively. Copied from [113].

Explicitly, they often employ the generalised Hebb's rule,

$$\Delta w_{ij} = \eta x_i x_j, \tag{5.12}$$

where x_i and x_j are the activities of neuron i and j respectively, Δw_{ij} is the change in the synaptic strength between them, and η is the learning rate. Although the generalised Hebb's rule (5.12) is as simple as a bilinear form in the activities of the pre- and post-synaptic neurons, the Hebb's rule commonly employed in biological neural networks, known as *spike-timing dependent plasticity* (STDP), is asymmetric and non-linear (see Fig. 5.1), which reveals the importance of temporal precedence in spikes. Notably these Hebb's rules are mainly concerned with chemical synapses and the function of STDP could imply the casuality between spikes in pre- and post-synaptic neurons as the signal propagation is uni-directional. However, the plasticity of electrical synapses are often difficult to measure experimentally and had been poorly investigated until recently Turecek et al. [114] found a mechanism of coupling enhancement at the inferior olive electrical synapse.

Synaptic plasticity is not considered in this thesis at all. It mainly contributes to emergent properties of large neural networks, while the study of dendritic membrane potential dynamics focuses on single neurons or small neuronal circuits. They also live in different time scales; synaptic strengths are hardly changed after a few spikes.

5.2 Further works

In addition to the above discussions, below are the natural directions to build upon the results of this thesis.

5.2.1 Realistic neuronal morphologies

The sum-over-trips framework was initially proposed for realistic morphologies [18]. However, it has not become useful in practice, because its solutions are in the form of infinite sums and the computational errors cannot be well controlled due to its disordered convergence. To overcome the problem, the method of local point matching has been developed which enables accurate and efficient computation on complex dendritic morphologies. Based on this method, a software package could be coded up that would read topological data of neuron reconstructions and automatically compute the Green's functions symbolically. The finite element method could be employed for continuously varying dendritic radii as suggested in §3.4.2. All simulations will then be able to skip the procedure of solving for the solutions to the partial differential equations numerically by simply substituting the values of parameters into the Green's function. In addition, it will be much easier to alter some parameters (geometrical or electrophysiological, local or global) to see their impacts on the dynamics of membrane potentials.

5.2.2 Large-scale neural networks

Even running on some of the most powerful computers in the world, the Blue Brain Project [115] could investigate a network of up to 5×10^5 neurons by 2012 [116], only a tiny fraction of an average human brain. With the Human Brain Project [35], Markram et al. [36] simulated a neural network with approximately 31,000 morphologically detailed neurons. To investigate larger netgworks, Izhikevich and Edelman [117] simulated at the cellular level a computational brain of exactly 10^{11} simplified nerve cells with almost 10^{15} synapses. Although the model was able to exhibit brainwaves, it took fifty days to produce the data of one second in the computational brain's real time.

Based on the framework studied in this thesis, responses functions on morphologically realistic resonant neurons can be obtained in advance. By incorporating the results in the above discusssions (e.g. spiking neurons, synaptic plasticity), simulations on a large-scale network consisting of such neurons of realistic geometric and electrical properties can be conducted at a low computational expense.

Appendix A

Detailed calculations

A.1 The simplified two-cell model

Here I show the detailed steps to obtain the Green's functions for the simplified two-cell model (see Fig. 4.10) by solving the system (4.21).

By noting the similarities between Eqs. (4.21b) and (4.21d) and between Eqs. (4.21a) and (4.21c), it is easy to see

$$J_b + J_d = 0, \tag{A.1a}$$

$$J_a + J_c = f(X_2)(2p_S - 1). \tag{A.1b}$$

Combining Eqs. (4.21c), (4.21d) and (A.1b), we arrive at

$$J_d = \frac{p_{GJ} f(L_{GJ})}{2p_R + 1} f_*(x_2, 0), \tag{A.2}$$

and then obtain J_a, J_b, J_c by substituting J_d back into the system (4.21). Notably p_R defined in (4.23) is more than a variable to save notations. $-p_R$ actually describes a trip travelling from one of the somata, changing its direction at the gap junction, arriving and reflecting at the same soma. It plays the same role as R in Eq. (2.68), a local recurrence of trips. Recall the formula for computing a geometric ratio, which explains $1 + 2p_R$ in the denominator of the expression of J_d (and in fact J_a, J_b, J_c too). Similarly, $f_*(x, y)$ defined in (4.24) has its physical meaning. It is actually a sum of two terms between x and y on the same neuron generated by local trips, one from x to y directly, and the other one from x to the closest soma, and reflectively to y. Such terms appear only when the input or the output locates on the dendritic branch in consideration, which essentially comes from Eqs. (2.80) and (2.82). $f_*(x, y)$ thus encodes the information of the different classes of trips as in

Fig. 2.3.

If the input is placed at $y_1 > l_{GJ}$, i.e. the distal part of the dendritic branch of neuron 1 (see Fig. 4.10), the local point matching method gives

$$J_{y_1} = [J_c f(L_{GJ})(1 - p_{GJ}) + J_a f(L_{GJ}) p_{GJ} + f(L_{GJ} - X_2) p_{GJ}] f(y_1 - L_{GJ}), \quad \text{(A.3)}$$

which leads to $G_2(x_2, y_1)$ in (4.22a). Similarly if the input is placed at $y_2 > l_{GJ}$, i.e. the distal part of the dendritic branch of neuron 2, we obtain

$$J_{y_2} = [J_a f(L_{GJ})(1 - p_{GJ}) + J_c f(L_{GJ}) p_{GJ} + f(L_{GJ} - X_2) p_{GJ}] f(y_2 - L_{GJ}), \quad \text{(A.4)}$$

and then $G_2(x_2, y_2)$ in (4.22b). If the input is placed at $y_3 < l_{GJ}$, i.e. the proximal part of the dendritic branch of neuron 1, we obtain

$$J_{y_3} = J_c f(Y_3) + J_d f(L_{GJ} - Y_3), \quad \text{(A.5)}$$

and then $G_2(x_2, y_3)$ in (4.22c). If the input is placed at $y_4 < l_{GJ}$, i.e. the proximal part of the dendritic branch of neuron 2, we obtain

$$J_{y_4} = J_a f(Y_4) + J_b f(L_{GJ} - Y_4) + f(|Y_4 - X_2|). \quad \text{(A.6)}$$

and then the Green's function

$$G_2(x_2, y_4) = \begin{cases} \frac{1}{2z} \left[f_*(X_2, Y_4) - \frac{p_{GJ}}{2p_R + 1} f_*(X_2, L_{GJ}) f_*(Y_4, L_{GJ}) \right], & \text{if } x_2 \le y_4, \\ \frac{1}{2z} \left[f_*(Y_4, X_2) - \frac{p_{GJ}}{2p_R + 1} f_*(X_2, L_{GJ}) f_*(Y_4, L_{GJ}) \right], & \text{if } x_2 \ge y_4. \end{cases} \quad \text{(A.7)}$$

When $x_2 = y_4$, one can check that the two expressions are identical to each other. The Green's functions on neuron 1 can then be easily found using the symmetry of the two neurons.

A.2 The tufted two-cell model

Here I solve for $G^*(x_0, y_2)$ in Eq. (4.35), i.e. the Green's function of the reduced tufted model in Fig. 4.13B. To save notations, the superscript $*$ is omitted in this section; since the original model is not discussed here, it is clear that all variables are for the reduced model.

Assume $x \le l_0$ is located on cell 1, the electrotonic length of the primary dendritic branch is L_0 and the electrotonic distance between the end of the primary branch and the gap junction is L_{GJ}. Employing the method of local point matching, we

can follow the arrows in Fig. 4.13B and write down

$$J_a = J_b f(L_0)(2p_S - 1) + f(X_0)(2p_S - 1), \tag{A.8a}$$
$$J_b = J_d f(L_{GJ})2p_D + J_a f(L_0)(2p_D - 1) + f(L_0 - X_0)(2p_D - 1), \tag{A.8b}$$
$$J_c = J_a f(L_0)2p_T + J_d f(L_{GJ})(2p_T - 1) + f(L_0)2p_T, \tag{A.8c}$$
$$J_d = J_c f(L_{GJ})(-p_{GJ}) + J_f f(L_{GJ})p_{GJ}, \tag{A.8d}$$
$$J_e = J_c f(L_{GJ})p_{GJ} + J_f f(L_{GJ})(-p_{GJ}), \tag{A.8e}$$
$$J_f = J_y f(L_0)2p_T + J_e f(L_{GJ})(2p_T - 1), \tag{A.8f}$$
$$J_g = J_e f(L_{GJ})2p_D + J_y f(L_0)(2p_D - 1), \tag{A.8g}$$
$$J_h = J_g f(L_0)(2p_S - 1), \tag{A.8h}$$

where p_S is the transition probability of either soma defined in (2.56), p_{GJ} the transition probability of the gap junction defined in (2.61), and p_D, p_T are the transition probabilities of the primary and tufted dendrites,

$$p_D = \frac{z_D}{z_D + 2z_T}, \tag{A.9a}$$
$$p_T = \frac{z_T}{z_D + 2z_T}, \tag{A.9b}$$

according to the definition (2.55), in which z_D, z_T are the characteristic admittances of the primary and tufted dendrites respectively. Solving the system (A.8), we obtain

$$J_a = R_2 p_S - 1 - \frac{R_S R_T R_2^2 p_{GJ} p_S p_D f(2L_{GJ})}{1 + 2R_0}, \tag{A.10a}$$
$$J_b = R_D R_2 p_S - \frac{R_T R_2^2 p_{GJ} p_S p_D f(2L_{GJ})}{1 + 2R_0}, \tag{A.10b}$$
$$J_c = R_T R_2 p_S \frac{1 + R_0}{1 + 2R_0}, \tag{A.10c}$$
$$J_d = \frac{-R_T R_2 p_{GJ} p_S f(L_{GJ})}{1 + 2R_0}, \tag{A.10d}$$
$$J_e = \frac{R_T R_2 p_{GJ} p_S f(L_{GJ})}{1 + 2R_0}, \tag{A.10e}$$
$$J_f = R_T R_2 p_S \frac{R_0}{1 + 2R_0}, \tag{A.10f}$$
$$J_g = \frac{R_T R_2^2 p_{GJ} p_S p_D f(2L_{GJ})}{1 + 2R_0}, \tag{A.10g}$$
$$J_h = \frac{R_S R_T R_2^2 p_{GJ} p_S p_D f(2L_{GJ})}{1 + 2R_0}, \tag{A.10h}$$

where

$$R_S = (2p_S - 1)f(L_0), \tag{A.11}$$

$$R_D = (2p_D - 1)f(L_0), \tag{A.12}$$

$$R_T = 2p_T f(L_0), \tag{A.13}$$

$$R_2 = \frac{2}{1 - R_S R_D}, \tag{A.14}$$

$$R_0 = (R_S R_T R_2 p_D + 2p_T - 1)p_{GJ} f(2L_{GJ}). \tag{A.15}$$

Considering only somatic input, i.e. $x = 0$, we have

$$J_y = \begin{cases} J_g f(L_0) + J_h f(0), & \text{if } x, y \text{ on the same cell,} \\ J_b f(L_0) + J_a f(0) + f(0), & \text{if } x, y \text{ on the different cells,} \end{cases} \tag{A.16}$$

which gives the Green's functions for x on cell 1 and y on either cell. By symmetry of the two cells, we in fact obtain the Green's function for x on either cell, given fixed y. Now assume y is located at soma 1

$$G_2(0,0) = \frac{R_T R_2^2 p_D p_S^2 p_{GJ} f(L_0 + 2L_{GJ})}{z_D(1 + 2R_0)}, \tag{A.17}$$

$$G_1(0,0) = \frac{p_S}{2z_D}(1 + R_D f(L_0))R_2 - G_2(0,0). \tag{A.18}$$

Appendix B

MATLAB code

All numerical computations in this thesis are conducted and the plots for their results are produced in MATLAB.

All models of single neurons (mainly discussed in §4.2 and §4.3) can be computed by the following MATLAB code with different parameter choices:

```
%%% all parameters
% space in um (micrometer), time are ms, otherwise marked
% length
l0=1e-1;rad0=1;%cylinder 2
l1=100;rad1=0;%1e-2;%quadratic

N=2;%partition N

%%% discrete shape, finite partition
Dl=l1/N;
radDl=zeros(1,N+1);x2=radDl;
l2=l1/(1-sqrt(rad1/rad0));%um
for i=1:N+1
    x2(i)=(i-1)*Dl;
    radDl(i)=rad0*(1-x2(i)/l2)^2;
end
rad2=zeros(1,N+1);
for i=1:N
    rad2(i)=(radDl(i)+radDl(i+1)+sqrt(radDl(i)*radDl(i+1)
       ))/3;
end
```

```
Dia2=2*rad2(1:end-1);
rad2(N+1)=rad2(N);
% theoretic shape, continuous
x2con=linspace(0,l2,101);radDlcon=x2con;
for i=1:101
    radDlcon(i)=rad0*(1-x2con(i)/l2)^2;
end
x2coni=find(x2con>l1,1);

%%% electronic paramters
% dendrites
Cm=1; %uF/cm2
Rm=2000;%1000; %Ohm-cm2
Ra=100;%;100; %Ohm-cm
Dia0=2*rad0;

r_res=inf;%1000; %Ohm cm^2
L_res=5;%5 %H cm^2
r_resk=r_res*1e-3;

% Somas
Dia_soma=12.5;%25; % um 50
Cm_soma=1; %uF/cm2
Rm_soma=2000;%1000;

rsoma_res=inf; %Ohm cm^2   1
Lsoma_res=5;%5 %H cm^2   0.1
rsoma_resk=rsoma_res*1e-3;

omega=0;

%%% variables with omega
% Dendrite
tau=1e-3*Cm*Rm; %ms
lambda0=sqrt(1e4/4*Dia0/(Ra/Rm)); %um
D0=lambda0^2/tau; %um2/ms
D=(1e4/4*Dia2/(Ra/Rm))/tau;
```

```
58
59 % Soma
60 Cs=Cm_soma*pi*Dia_soma^2;%1e-8uF
61 tau_s=1e-3*Cm_soma*Rm_soma; %ms
62
63 r_a0=4*Ra/(pi*Dia0^2);
64 r_a=4*Ra./(pi*Dia2.^2);
65
66 %%% variables of use
67 gamma0=sqrt((1/tau+omega+1./(Cm.*(r_resk+L_res*omega)))/
      D0); %resonant dendrite
68 gamma=zeros(N,Om);%1/um
69 for i=1:N
70     gamma(i,:)=sqrt((1/tau+omega+1./(Cm.*(r_resk+L_res*
         omega)))/D(i));
71 end
72 f0=exp(-gamma0*l0);
73 f=exp(-gamma*Dl);%no unit
74 z_s=1e-7*Cs*(omega+1/tau_s+1./(Cm_soma*(rsoma_resk+
      Lsoma_res*omega)));%resonant soma
75 z0=gamma0./r_a0;%1e-4S
76 z=zeros(N,Om);
77 for i=1:N
78     z(i,:)=gamma(i,:)./r_a(i);
79 end
80 pr=z;pl=z;
81 pr(1,:)=z(1,:)./(z0+z(1,:));%non-branching
82 pl(1,:)=z0./(z0+z(1,:));%non-branching
83 for i=2:N
84     pr(i,:)=z(i,:)./(z(i-1,:)+z(i,:));
85     pl(i,:)=z(i-1,:)./(z(i-1,:)+z(i,:));
86 end
87 ps=z0./(z0+z_s);
88 %%%
89
90 %%% algebraic equations/matrix representation
91 coeffAB=zeros(2*N+2,2*N+2,Om);invcoefAB=coeffAB;
```

```
92  constAB=zeros(2*N+2,Om);AB=constAB;
93  for i=1:2*N+2
94      coeffAB(i,i,:)=-1;
95  end
96  % AB(1)=A1=J_a1,AB(2)=A2=J_a2,...,AB(N+1)=B1=J_b1,AB(N+N)
       =BN=J_bN,AB(end-1)=A0+1=J_a0+1,AB(end)=J_b0
97  coeffAB(end-1,end,:)=f0.*(2*ps-1);
98  constAB(end-1,:)=-2*ps;
99  coeffAB(1,end-1,:)=2*f0.*pr(1,:);
100 %coeffAB(1,N+1,:)=f(1,:).*(4*pr(1,:)-1);%for branching
101 coeffAB(1,N+1,:)=f(1,:).*(2*pr(1,:)-1);%for non-branching
102 for i=2:N
103     coeffAB(i,i-1,:)=2*f(i-1,:).*pr(i,:);
104     coeffAB(i,N+i,:)=f(i,:).*(2*pr(i,:)-1);
105 end
106 coeffAB(end,end-1,:)=f0.*(2*pl(1)-1);
107 %coeffAB(end,N+1,:)=4*f(1,:).*pl(1);%for branching
108 coeffAB(end,N+1,:)=2*f(1,:).*pl(1);%for non-branching
109 for i=1:N-1
110     coeffAB(N+i,i,:)=f(i,:).*(2*pl(i+1)-1);
111     coeffAB(N+i,N+i+1,:)=2*f(i+1,:).*pl(i+1);
112 end
113 coeffAB(N+N,N,:)=f(N,:);
114 %%% inverse the matrix, times the constant column
115 for i=1:Om
116     AB(:,i)=coeffAB(:,:,i)\constAB(:,i);
117 end
118 %%%
119
120 %%% via Poznanski's transformation
121 Z_K=-3*lambda0/(2*l2);%no unit
122 Z_l0=l0/lambda0;%the primary dendrite is a cylinder;
123 Z_l1=3/(2*Z_K)*log(1-l1/l2);%no unit
124 Z_beta=1+Z_K^2;%no unit
125 Z_gamma0=sqrt(omega*tau+1);%beta=1 if cylindrical
126 Z_gamma1=sqrt(omega*tau+Z_beta);%no unit
127 Z_z0=Z_gamma0/(lambda0*r_a0);%1e-4S, same as z0
```

```
128 Z_ps=Z_z0./(Z_z0+z_s);
129 Z_lambda1_0=lambda0*(1+4*rad0^2/l2^2)^(-1/4);%um
130 Z_z1=Z_gamma1/(Z_lambda1_0*r_a0);
131 %Z_denop=2*(Z_gamma1+Z_K)/(Z_lambda1_0*r_a0)+Z_z0;%for
       branching
132 Z_denop=(Z_gamma1+Z_K)/(Z_lambda1_0*r_a0)+Z_z0;%for non-
       branching
133 Z_p0=Z_z0./Z_denop;
134 Z_Phi10=sqrt(lambda0/Z_lambda1_0);
135 Z_p1=Z_z1./Z_denop;
136 Z_Phi01=1/Z_Phi10;
137 AsR=2*Z_ps-1;%reflection at soma
138 AbR0=2*Z_p0-1;%reflection at branching, from primary back
        to primary
139 AbT10=2*Z_p0*Z_Phi10;%transition at branching, to primary
140 AbR1=2*Z_p1-1;%reflection at branching, from branched
       back to branched
141 AbT01=2*Z_p1*Z_Phi01;%transition at branching, from
       primary to branched
142 AbT11=2*Z_p1;%transition at branching, from branched to
       the other branched
143 AcR=2*Z_gamma1./(Z_gamma1-Z_K)-1;%reflection at closed
       end
144 fZ0=exp(-Z_gamma0*Z_l0);
145 fZ1=exp(-Z_gamma1*Z_l1);
146 %%% algebraic equation -- matrix: A1=J_A+1
147 coeffA1BCD=zeros(4,4,Om);invcoeffA1BCD=coeffA1BCD;
148 constA1BCD=zeros(4,Om);A1BCD=constA1BCD;
149 for i=1:4
150     coeffA1BCD(i,i,:)=-1;
151 end
152 coeffA1BCD(1,2,:)=fZ0.*AsR;
153 constA1BCD(1,:)=-(AsR+1);
154 coeffA1BCD(2,1,:)=fZ0.*AbR0;
155 %coeffA1BCD(2,4,:)=2*fZ1.*AbT10;%for branching
156 coeffA1BCD(2,4,:)=fZ1.*AbT10;%for non-branching
157 coeffA1BCD(3,1,:)=fZ0.*AbT01;
```

```
%coeffA1BCD(3,4,:)=fZ1.*(AbR1+AbT11);%for branching
coeffA1BCD(3,4,:)=fZ1.*AbR1;%for non-branching
coeffA1BCD(4,3,:)=fZ1.*AcR;
for i=1:Om
    invcoeffA1BCD(:,:,i)=inv(coeffA1BCD(:,:,i));
    A1BCD(:,i)=invcoeffA1BCD(:,:,i)*constA1BCD(:,i);
end

%%%
yyy=0:.01:l0+l1-1e-11;
Noy=length(yyy);
Vcyli0=zeros(1,Noy);
Vquad0=Vcyli0;

for j=1:Noy
y_um=yyy(j);
%%% test Green
if y_um>l0
    yi=find(x2(2:end)>y_um-l0,1);
    lax=y_um-x2(yi)-l0;
    lbx=Dl-lax;
    testG=(AB(yi,:).*exp(-gamma(yi,:).*lax)+AB(yi+N,:).*
       exp(-gamma(yi,:).*lbx))./(2*D(yi).*gamma(yi,:));%
       ms/um
else
    testG=(AB(end-1,:).*exp(-gamma0*y_um)+AB(end,:).*exp
       (-gamma0*(l0-y_um)))./(2*D0.*gamma0);
end

%%% current
Amp_nA=.2;

if y_um>l0
    y1=y_um-l0;
    Z_Y=3/(2*Z_K)*log(1-y1/l2);
    Z_Jy=A1BCD(3,:).*exp(-Z_gamma1.*Z_Y)+A1BCD(4,:).*exp
       (-Z_gamma1.*(Z_l1-Z_Y));
```

```
191     lambday=Z_lambda1_0*(1-y1/l2)*(1+4*rad0^2/l2^4*(l2-y1
            )^2)^(-1/4);
192     phiy=exp(-Z_K*Z_Y);
193     testGpoz=tau./(2*Z_gamma1.*lambday.*phiy).*Z_Jy;
194
195     rc_um=rad2(yi);
196     I0c=Amp_nA/2/pi/rc_um/Cm*1e5;
197     ry_um=rad0*(1-y1/l2)^2;
198     I0t=Amp_nA/2/pi/ry_um/sqrt(1+4*rad0*ry_um/l2^2)/Cm*1
            e5;
199 else
200     Z_Y=y_um/lambda0;
201     Z_Jy=A1BCD(1,:).*exp(-Z_gamma0.*Z_Y)+A1BCD(2,:).*exp
            (-Z_gamma0.*(Z_l0-Z_Y));
202     testGpoz=tau./(2*Z_gamma0.*lambda0).*Z_Jy;
203
204     rc_um=rad0;
205     I0c=Amp_nA/2/pi/rc_um/Cm*1e5;
206     ry_um=rad0;
207     I0t=Amp_nA/2/pi/ry_um/Cm*1e5;
208 end
209
210 Vcyli0(j)=I0c*testG;
211 Vquad0(j)=I0t*testGpoz;
212
213 end
214 %%%
215 figure(1), hold on
216 plot(yyy-l0,Vcyli0,'r')
217 plot(yyy-l0,Vquad0,'b')
218 xlim([0 100])
219
220 figure(2), hold on
221 plot(yyy,Vquad0-Vcyli0)
222 xlim([0 100])
```

Appendix C

Miscellaneous notes

- Fig. 1.5 and 1.6 are generated in NEURON.
- All symbolic calculations in this thesis are derived by hand and checked with Wolfram Mathematica.
- The figures on the cover pages of all chapters in this thesis are obtained by the following Mathematica code:

```
Plot3D[Im[(0.5 (E^-Sin[y^RandomReal[20]] + E^(1 - Sin[y^
    RandomReal[20]])))/(Sqrt[1 + w I + 1/(1 + w I)] (1 +
    0.8 E^2))], {w, -50,50}, {y, -10, -1}, Mesh -> All,
    MeshFunctions -> Automatic,Mesh -> Automatic,
    MeshFunctions -> {#3 &},PlotStyle -> Directive[
    Opacity[0]], Axes -> False,ViewPoint -> Above]
```

  Notably this expression is a special modification of Eq. (2.95). For a fixed value of the argument in `RandomReal[ ]`, each configuration is random but they share a similar pattern. One can change the value of the argument, for example changing `20` in the above code to `40`, to obtain different patterns.

Bibliography

[1] Santiago Ramón y Cajal. *Significación fisiológica de las expansiones protoplásmicas y nerviosas de las células de la sustancia gris.* 1891.

[2] Herbert Spencer. *The Principles of Biology, Vol. 2.* Willium And Norgate, London, 1884.

[3] Dale Purves and Jeff W Lichtman. Geometrical differences among homologous neurons in mammals. *Science*, 228(4697):298–302, 1985.

[4] James T Voyvodic. Peripheral target regulation of dendritic geometry in the rat superior cervical ganglion. *Journal of Neuroscience*, 9(6):1997–2010, 1989.

[5] Wilfrid Rall, Robert E Burke, William R Holmes, James J Jack, Stephan J Redman, and Idan Segev. Matching dendritic neuron models to experimental data. *Physiological Reviews*, 72(suppl_4):S159–S186, 1992.

[6] Zachary F Mainen and Terrence J Sejnowski. Influence of dendritic structure on firing pattern in model neocortical neurons. *Nature*, 382(6589):363, 1996.

[7] Philipp Vetter, Arnd Roth, and Michael Häusser. Propagation of action potentials in dendrites depends on dendritic morphology. *Journal of Neurophysiology*, 85(2):926–937, 2001.

[8] Moritz Helmstaedter, Bert Sakmann, and Dirk Feldmeyer. The relation between dendritic geometry, electrical excitability, and axonal projections of L2/3 interneurons in rat barrel cortex. *Cerebral Cortex*, 19(4):938–950, 2008.

[9] Jeffrey C Magee. Dendritic hyperpolarization-activated currents modify the integrative properties of hippocampal CA1 pyramidal neurons. *Journal of Neuroscience*, 18(19):7613–7624, 1998.

[10] Greg Stuart and Nelson Spruston. Determinants of voltage attenuation in neocortical pyramidal neuron dendrites. *Journal of Neuroscience*, 18(10):3501–3510, 1998.

[11] Michael Häusser, Nelson Spruston, and Greg J Stuart. Diversity and dynamics of dendritic signaling. *Science*, 290(5492):739–744, 2000.

[12] Stephen R Williams and Greg J Stuart. Site independence of EPSP time course is mediated by dendritic I(h) in neocortical pyramidal neurons. *Journal of Neurophysiology*, 83(5):3177–3182, 2000.

[13] Nace L Golding, William L Kath, and Nelson Spruston. Dichotomy of action-potential backpropagation in CA1 pyramidal neuron dendrites. *Journal of Neurophysiology*, 86(6):2998–3010, 2001.

[14] Nicholas P Poolos, Michele Migliore, and Daniel Johnston. Pharmacological upregulation of h-channels reduces the excitability of pyramidal neuron dendrites. *Nature Neuroscience*, 5(8):767, 2002.

[15] Maarten H P Kole, Stefan Hallermann, and Greg J Stuart. Single Ih channels in pyramidal neuron dendrites: properties, distribution, and impact on action potential output. *Journal of Neuroscience*, 26(6):1677–1687, 2006.

[16] Helen C Lai and Lily Y Jan. The distribution and targeting of neuronal voltage-gated ion channels. *Nature Reviews Neuroscience*, 7(7), 2006.

[17] Wilfrid Rall. Theory of physiological properties of dendrites. *Annals of the New York Academy of Sciences*, 96(1):1071–1092, 1962.

[18] Laurence F Abbott, Edward Farhi, and Sam Gutmann. The path integral for dendritic trees. *Biological Cybernetics*, 66(1):49–60, 1991.

[19] Stephen Coombes, Yulia Timofeeva, Carl-Magnus Svensson, Gabriel J Lord, Krešimir Josić, Steven J Cox, and Costa M Colbert. Branching dendrites with resonant membrane: a "sum-over-trips" approach. *Biological Cybernetics*, 97 (2):137–149, 2007.

[20] Yulia Timofeeva, Stephen Coombes, and Davide Michieletto. Gap junctions, dendrites and resonances: a recipe for tuning network dynamics. *The Journal of Mathematical Neuroscience*, 3(1):15, 2013.

[21] Stanley Finger. *Origins of Neuroscience: a history of explorations into brain function.* Oxford University Press, USA, 2001.

[22] Terry F Hoad, editor. *The Concise Oxford Dictionary of English Etymology.* Oxford University Press, Oxford, 1993.

[23] Bartlett W Mel. Information processing in dendritic trees. *Neural Computation*, 6(6):1031–1085, 1994.

[24] Giorgio A Ascoli. *Computational Neuroanatomy: principles and methods*. Springer Science & Business Media, 2002.

[25] Giorgio A Ascoli, Duncan E Donohue, and Maryam Halavi. Neuromorpho.org: a central resource for neuronal morphologies. *Journal of Neuroscience*, 27(35): 9247–9251, 2007.

[26] Mitch Glickstein. Golgi and Cajal: The neuron doctrine and the 100th anniversary of the 1906 Nobel Prize. *Current Biology*, 16(5):R147–R151, 2006.

[27] James J Mancuso, Yuanxin Chen, Xuping Li, Zhong Xue, and Stephen TC Wong. Methods of dendritic spine detection: from Golgi to high-resolution optical imaging. *Neuroscience*, 251:129–140, 2013.

[28] Edmund M Glaser and Hendrik F M Van der Loos. A semi-automatic computer-microscope for the analysis of neuronal morphology. *IEEE Transactions on Biomedical Engineering*, BME-12(1):22–31, 1965.

[29] Joseph J Capowski and Mathius J Sedivec. Accurate computer reconstruction and graphics display of complex neurons utilizing state-of-the-art interactive techniques. *Computers and Biomedical Research*, 14(6):518–532, 1981.

[30] Thomas S Ford-Holevinski, Todd A Dahlberg, and Bernard W Agranoff. A microcomputer-based image analyzer for quantitating neurite outgrowth. *Brain Research*, 368(2):339–346, 1986.

[31] Joseph J Capowski. An automatic neuron reconstruction system. *Journal of Neuroscience Methods*, 8(4):353–364, 1983.

[32] Joseph J Capowski. *Computer Techniques in Neuroanatomy*. Springer Science & Business Media, 2012.

[33] Erik Meijering. Neuron tracing in perspective. *Cytometry Part A*, 77(7): 693–704, 2010.

[34] Hanchuan Peng, Fuhui Long, Ting Zhao, and Eugene Myers. Proof-editing is the bottleneck of 3D neuron reconstruction: the problem and solutions. *Neuroinformatics*, 9(2-3):103–105, 2011.

[35] Henry Markram. The human brain project. *Scientific American*, 306(6):50–55, 2012.

[36] Henry Markram, Eilif Muller, Srikanth Ramaswamy, Michael W Reimann, Marwan Abdellah, Carlos Aguado Sanchez, Anastasia Ailamaki, Lidia Alonso-Nanclares, Nicolas Antille, Selim Arsever, et al. Reconstruction and simulation of neocortical microcircuitry. *Cell*, 163(2):456–492, 2015.

[37] Donald A Sholl. Dendritic organization in the neurons of the visual and motor cortices of the cat. *Journal of Anatomy*, 87(Pt 4):387, 1953.

[38] Christopher Cherniak, Mark Changizi, and Du Won Kang. Large-scale optimization of neuron arbors. *Physical Review E*, 59(5):6001, 1999.

[39] Hermann Cuntz, Alexander Borst, and Idan Segev. Optimization principles of dendritic structure. *Theoretical Biology & Medical Modelling*, 4:21–21, 2007.

[40] Tobias Bonhoeffer and Rafael Yuste. Spine motility: phenomenology, mechanisms, and function. *Neuron*, 35(6):1019–1027, 2002.

[41] Warren S McCulloch and Walter Pitts. A logical calculus of the ideas immanent in nervous activity. *The Bulletin of Mathematical Biophysics*, 5(4): 115–133, 1943.

[42] Alan L Hodgkin and Andrew F Huxley. A quantitative description of membrane current and its application to conduction and excitation in nerve. *The Journal of Physiology*, 117(4):500–544, 1952.

[43] Peter Dayan and Laurence F Abbott. *Theoretical Neuroscience*. MIT Press, 2001.

[44] Christof Koch. Cable theory in neurons with active, linearized membranes. *Biological Cybernetics*, 50(1):15–33, 1984.

[45] Magnus J E Richardson. Introduction to Theoretical Neuroscience (lecture notes). URL `https://warwick.ac.uk/fac/sci/systemsbiology/staff/richardson/teaching/ma4g4/ITN_LN1.pdf`. Last visited on 2017/12/16.

[46] Hermann Von Helmholtz. Messungen über den zeitlichen verlauf der zuckung animalischer muskeln und die fortpflanzungsgeschwindigkeit der reizung in den nerven. *Archiv für Anatomie, Physiologie und wissenschaftliche Medicin*, 17: 176–364, 1850.

[47] William Thomson. III. On the theory of the electric telegraph. *Proceedings of the Royal Society of London*, 7:382–399, 1856.

[48] Idan Segev, John Rinzel, and Gordon M Shepherd, editors. *The Theoretical Foundation of Dendritic Function: selected papers of Wilfrid Rall with commentaries*. MIT press, 1995.

[49] Henry C Tuckwell. *Introduction to Theoretical Neurobiology*. Cambridge University Press, 1988.

[50] Wilfrid Rall. Core conductor theory and cable properties of neurons. *Comprehensive physiology*, pages 39–97, 2011.

[51] Kenneth A Lindsay, Jay R Rosenberg, and G Tucker. From Maxwell's equations to the cable equation and beyond. *Progress in Biophysics & Molecular Biology*, 85(1):71–116, 2004.

[52] Wilfrid Rall. Distributions of potential in cylindrical coordinates and time constants for a membrane cylinder. *Biophysical Journal*, 9(12):1509–1541, 1969.

[53] Wilfrid Rall. Distinguishing theoretical synaptic potentials computed for different soma-dendritic distributions of synaptic input. *Journal of Neurophysiology*, 30(5):1138–1168, 1967.

[54] James J B Jack, Denis Noble, and Richard W Tsien. *Electric Current Flow in Excitable Cells*. Clarendon Press Oxford, 1983.

[55] Yoshiyuki Kubota, Fuyuki Karube, Masaki Nomura, Allan T Gulledge, Atsushi Mochizuki, Andreas Schertel, and Yasuo Kawaguchi. Conserved properties of dendritic trees in four cortical interneuron subtypes. *Scientific Reports*, 1:89, 2011.

[56] Stephen Coombes and Áine Byrne. Next generation neural mass models. *arXiv preprint arXiv:1607.06251*, 2016.

[57] Tom Rother. *Green's Functions in Classical Physics*, volume 938. Springer, 2017.

[58] Norbert Ortner and Peter Wagner. *Fundamental Solutions of Linear Partial Differential Operators*. Springer, 2015.

[59] Richard D Mattuck. *A Guide to Feynman Diagrams in the Many-Body Problem*. Courier Corporation, 1976.

[60] David J Griffiths. *Introduction to Quantum Mechanics*. Cambridge University Press, 2016.

[61] Raymond A DeCarlo and Pen-Min Lin. *Linear Circuit Analysis: time domain, phasor, and Laplace transform approaches*. Oxford University Press, 2001.

[62] Peter Kuchment. Quantum graphs: an introduction and a brief survey. *arXiv preprint arXiv:0802.3442*, 2008.

[63] Gregory Berkolaiko and Peter Kuchment. *Introduction to Quantum Graphs*. American Mathematical Society, 2013.

[64] Christof Koch, Tomaso Poggio, and Vincent Torre. Nonlinear interactions in a dendritic tree: localization, timing, and role in information processing. *Proceedings of the National Academy of Sciences*, 80(9):2799–2802, 1983.

[65] Ivar Stakgold and Michael J Holst. *Green's Functions and Boundary Value Problems*. John Wiley & Sons, 2011.

[66] Edward G Butz and Jack D Cowan. Transient potentials in dendritic systems of arbitrary geometry. *Biophysical Journal*, 14(9):661, 1974.

[67] Christof Koch and Tomaso Poggio. A simple algorithm for solving the cable equation in dendritic trees of arbitrary geometry. *Journal of Neuroscience Methods*, 12(4):303–315, 1985.

[68] Nicholas T Carnevale and Michael L Hines. *The NEURON Book*. Cambridge University Press, 2006.

[69] Laurence F Abbott. Simple diagrammatic rules for solving dendritic cable problems. *Physica A: Statistical Mechanics and its Applications*, 185(1-4): 343–356, 1992.

[70] Quentin Caudron, Simon R Donnelly, Samuel P C Brand, and Yulia Timofeeva. Computational convergence of the path integral for real dendritic morphologies. *The Journal of Mathematical Neuroscience*, 2(1):11, 2012.

[71] Bulin J Cao and Laurence F Abbott. A new computational method for cable theory problems. *Biophysical Journal*, 64(2):303–313, 1993.

[72] Quentin Caudron. *Neuronal Computation on Complex Dendritic Morphologies*. PhD thesis, University of Warwick, 2012.

[73] Lu Yihe and Yulia Timofeeva. Response functions for electrically coupled neuronal network: a method of local point matching and its applications. *Biological Cybernetics*, 110(2-3):117–133, 2016.

[74] Yulia Timofeeva and Stephen Coombes. *The Computing Dendrite: from structure to function*, chapter Network response of gap junction coupled dendrites, pages 449–464. Springer, 2014.

[75] Peter Sterling and Simon Laughlin. *Principles of Neural Design*. MIT Press, 2015.

[76] Nancy L Desmond and William B Levy. Dendritic caliber and the 3/2 power relationship of dentate granule cells. *Journal of Comparative Neurology*, 227 (4):589–596, 1984.

[77] Peter A V Anderson and George O Mackie. Electrically coupled, photosensitive neurons control swimming in a jellyfish. *Science*, 197(4299):186–188, 1977.

[78] George O Mackie. Central neural circuitry in the jellyfish Aglantha. *Neurosignals*, 13(1-2):5–19, 2004.

[79] Paul C Bressloff and Stephen Coombes. Solitary waves in a model of dendritic cable with active spines. *SIAM Journal on Applied Mathematics*, 61(2):432–453, 2000.

[80] Stephen Coombes. From periodic travelling waves to travelling fronts in the spike–diffuse–spike model of dendritic waves. *Mathematical Biosciences*, 170 (2):155–172, 2001.

[81] Yulia Timofeeva, Gabriel J Lord, and Stephen Coombes. Dendritic cable with active spines: A modelling study in the spike-diffuse-spike framework. *Neurocomputing*, 69(10-12):1058–1061, 2006.

[82] Yulia Timofeeva, Gabriel J Lord, and Stephen Coombes. Spatio-temporal filtering properties of a dendritic cable with active spines: a modeling study in the spike-diffuse-spike framework. *Journal of Computational Neuroscience*, 21(3):293–306, 2006.

[83] Silvina P Dawson, Joel Keizer, and John E Pearson. Fire-diffuse-fire model of dynamics of intracellular calcium waves. *Proceedings of the National Academy of Sciences*, 96(11):6060–6063, 1999.

[84] Stephen Coombes and Yulia Timofeeva. Sparks and waves in a stochastic fire-diffuse-fire model of Ca 2+ release. *Physical Review E*, 68(2):021915, 2003.

[85] Jamie Harris and Yulia Timofeeva. Intercellular calcium waves in the fire-diffuse-fire framework: Green's function for gap-junctional coupling. *Physical Review E*, 82(5):051910, 2010.

[86] William P Bartlett and Gary A Banker. An electron microscopic study of the development of axons and dendrites by hippocampal neurons in culture. I. Cells which develop without intercellular contacts. *Journal of Neuroscience*, 4(8):1944–1953, 1984.

[87] John D Clements and Stephan J Redman. Cable properties of cat spinal motoneurones measured by combining voltage clamp, current clamp and intracellular staining. *The Journal of Physiology*, 409(1):63–87, 1989.

[88] Charles J Wilson and Joseph C Callaway. Coupled oscillator model of the dopaminergic neuron of the substantia nigra. *Journal of Neurophysiology*, 83 (5):3084–3100, 2000.

[89] Graeme Lowe. Inhibition of backpropagating action potentials in mitral cell secondary dendrites. *Journal of Neurophysiology*, 88(1):64–85, 2002.

[90] Juan M Romero and Carlos Trenado. Analytical solution of a tapering cable equation for dendrites and conformal symmetry. *Biophysical Reviews and Letters*, 10(03):175–185, 2015.

[91] George M Strain and William H Brockman. A modified cable model for neuron processes with non-constant diameters. *Journal of Theoretical Biology*, 51(2): 475–494, 1975.

[92] Alison S Walker, Guilherme Neves, Federico Grillo, Rachel E Jackson, Mark Rigby, Cian O'Donnell, Andrew S Lowe, Gema Vizcay-Barrena, Roland A Fleck, and Juan Burrone. Distance-dependent gradient in NMDAR-driven spine calcium signals along tapering dendrites. *Proceedings of the National Academy of Sciences*, page 201607462, 2017.

[93] Roman R Poznanski. A generalized tapering equivalent cable model for dendritic neurons. *Bulletin of Mathematical Biology*, 53(3):457–467, 1991.

[94] Wilfrid Rall. Electrophysiology of a dendritic neuron model. *Biophysical Journal*, 2(2):145–167, 1962.

[95] G Bard Ermentrout and David H Terman. *Mathematical Foundations of Neuroscience*, volume 35. Springer Science & Business Media, 2010.

[96] Alex D Bird and Hermann Cuntz. Optimal current transfer in dendrites. *PLoS Computational Biology*, 12(5):e1004897, 2016.

[97] Steven S Goldstein and Wilfrid Rall. Changes of action potential shape and velocity for changing core conductor geometry. *Biophysical Journal*, 14(10): 731–757, 1974.

[98] Heather A Cameron and Ronald D G Mckay. Adult neurogenesis produces a large pool of new granule cells in the dentate gyrus. *Journal of Comparative Neurology*, 435(4):406–417, 2001.

[99] Michele Migliore, Michael L Hines, and Gordon M Shepherd. The role of distal dendritic gap junctions in synchronization of mitral cell axonal output. *Journal of Computational Neuroscience*, 18(2):151–161, 2005.

[100] Olivier Vallée and Manuel Soares. *Airy Functions and Applications to Physics*. World Scientific Publishing Company, 2010.

[101] Eric W Weisstein. Airy functions. from *MathWorld*–a Wolfram web resource. URL `http://mathworld.wolfram.com/AiryFunctions.html`. Last visited on 2018/06/29.

[102] Wulfram Gerstner and Werner Kistler. *Spiking Neuron Models: single neurons, populations, plasticity*. Cambridge University Press, 2002.

[103] Michael A Schwemmer and Timothy J Lewis. Bistability in a leaky integrate-and-fire neuron with a passive dendrite. *SIAM Journal on Applied Dynamical Systems*, 11(1):507–539, 2012.

[104] Steven M Baer and John Rinzel. Propagation of dendritic spikes mediated by excitable spines: a continuum theory. *Journal of Neurophysiology*, 65(4): 874–890, 1991.

[105] Wilfrid Rall, Gordon M Shepherd, Thomas S Reese, and Milton W Brightman. Dendrodendritic synaptic pathway for inhibition in the olfactory bulb. *Experimental neurology*, 14(1):44–56, 1966.

[106] Didier Pinault, Yoland Smith, and Martin Deschênes. Dendrodendritic and axoaxonic synapses in the thalamic reticular nucleus of the adult rat. *Journal of Neuroscience*, 17(9):3215–3233, 1997.

[107] Roger D Traub, Nancy Kopell, Andrea Bibbig, Eberhard H Buhl, Fiona E N LeBeau, and Miles A Whittington. Gap junctions between interneuron dendrites can enhance synchrony of gamma oscillations in distributed networks. *Journal of Neuroscience*, 21(23):9478–9486, 2001.

[108] Gordon M Shepherd. Dendrodendritic synapses: past, present and future. *Annals of the New York Academy of Sciences*, 1170, 2009.

[109] Fred Walberg. Axoaxonic contacts in the cuneate nucleus, probable basis for presynaptic depolarization. *Experimental neurology*, 13(2):218–231, 1965.

[110] Paul C Bressloff and Stephen Coombes. Physics of the extended neuron. *International Journal of Modern Physics B*, 11(20):2343–2392, 1997.

[111] Donald O Hebb. *The Organization of Behavior:a neuropsychological theory*. Psychology Press, 2005.

[112] John J Hopfield. Neural networks and physical systems with emergent collective computational abilities. *Proceedings of the National Academy of Sciences*, 79(8):2554–2558, 1982.

[113] Guo-qiang Bi and Mu-ming Poo. Synaptic modification by correlated activity: Hebb's postulate revisited. *Annual Review of Neuroscience*, 24(1):139–166, 2001.

[114] Josef Turecek, Genevieve S Yuen, Victor Z Han, Xiao-Hui Zeng, K Ulrich Bayer, and John P Welsh. NMDA receptor activation strengthens weak electrical coupling in mammalian brain. *Neuron*, 81(6):1375–1388, 2014.

[115] Henry Markram. The blue brain project. *Nature Reviews Neuroscience*, 7(2): 153–160, 2006.

[116] Farhan Tauheed, Laurynas Biveinis, Thomas Heinis, Felix Schürmann, Henry Markram, and Anastasia Ailamaki. Accelerating range queries for brain simulations. In *2012 IEEE 28th International Conference on Data Engineering*, pages 941–952. IEEE, 2012.

[117] Eugene M Izhikevich and Gerald M Edelman. Large-scale model of mammalian thalamocortical systems. *Proceedings of the National Academy of Sciences*, 105 (9):3593–3598, 2008.